Cutting Edge Honing With Non-Newtonian Fluids

CUTTING EDGE HONING WITH NON-NEWTONIAN FLUIDS

BY

JASON SIU FUNG CHAN, B.ENG.

A THESIS

SUBMITTED TO THE DEPARTMENT OF MECHANICAL ENGINEERING

AND THE SCHOOL OF GRADUATE STUDIES

OF MCMASTER UNIVERSITY

IN PARTIAL FULFILMENT OF THE REQUIREMENTS

FOR THE DEGREE OF

MASTER OF APPLIED SCIENCE

Master of Applied Science (2020)   McMaster University

(Mechanical Engineering)   Hamilton, Ontario, Canada

TITLE: Cutting Edge Honing with Non-Newtonian Fluids

AUTHOR: Jason Siu Fung Chan

                    B.ENG (Mechanical Engineering)

                    McMaster University, Hamilton, Canada

SUPERVISOR: Dr. Philip Koshy

NUMBER OF PAGES: 154

To My Loving Parents

Abstract

Cutting tool edges are honed to an edge radius of about 15-30 micrometers for enhancing tool performance. During honing, defects left by prior manufacturing processes such as grinding and pressing are removed to achieve a higher quality edge. Recently, researchers have shown that tailoring the edge microgeometry to comprise an asymmetric shape and/or a gradient edge microgeometry is beneficial. Conventional edge honing processes such as brush honing and abrasive micro-blasting are limited in terms of reliably generating such geometries in a productive manner. To this end, this research explored the application of non-Newtonian aqueous suspensions of cornstarch and abrasives, for the edge honing of cutting tools. This thesis details the science, technology, characteristics and capabilities of this innovative process.

Acknowledgements

I have encountered countless challenges during the time of my thesis, and I would like to acknowledge all the people who helped me physically and spiritually.

I would like to thank my supervisor, Dr. Philip Koshy, for his continuous guidance, patience and motivation through each stage of the process. His encouragement allowed me to think outside of the box.

I would like to acknowledge the staff in the MMRI lab. Terry Wagg has opened up my eyes to the real-world industry and limitations I might encounter. Brady Semple has taught me numerous manufacturing techniques.

I would like to show my gratitude to the Machine Shop Laboratory staff, especially Ron Lodewyks and Mark Mackenzie. They spent hours and hours to sit down and have meeting with me to discuss the design of my apparatus. They provided me with a lot of suggestion and taught me how to make a lean design.

Thank you, Dr. Chan Y. Ching, for the mentorship in teaching and sharing your knowledge in fluid mechanics and providing me with the opportunity to set up an undergraduate lab.

I would like to pay my regards to my colleagues, Andy Guo, Gurpyar Dhadda and Sophia Deng. The presentation skill by Andy Guo was breathtaking and captured the audience attention with his amazing slideshows. Gurpyar Dhadda has offered me insightful knowledge in the fluid mechanics. Sophia Deng and Sameh Mamdouh have shown me awesome techniques to capture amazing pictures on the SEM microscope.

I wish to present my special thanks to my loving parents, Lindy Chan and Jimmy Chan for their support of my passions and interests in the development of innovative technologies. I would like to thank Darlene Tran for your love and constant support. I appreciate my friends Justin Chow and Raymond Lo for your mental support.

Contents

List of Tables

List of Figures

Chapter 1

Introduction

Metal working dates to preliterate times by Neolithic people. Metal mining, smelting and casting were then practiced by ancient Asians and Egyptians to produce weapons and tools [1]. It was not until the Industrial Revolution of the late eighteenth century that metal cutting was developed to incorporate elements of science. The earliest scientific studies were performed by Time [2], Tresca [3] and Mallock [4] to describe chip formation in metal cutting to be due to shearing action ahead of the cutting edge. Up until the late 1800s cutting tools were primarily made of low carbon steels. Taylor invented High Speed Steel (HSS) in the early 1900s that enabled a higher cutting speed and performance in machining. In the twentieth century, the development of cemented carbide and ceramic tools further elevated cutting speed and machining productivity.

Throughout history, it was believed that cutting tools with a sharp edge would yield a higher performance than a rounded one. In 1945, Merchant [5] developed an early analytical model based on the assumption of a sharp cutting edge to predict process force and offer simple explanations of metal cutting. Numerous attempts have been made by CIRP (International Institution for Production Engineering Research) to improve the predictive ability of the model proposed by Merchant but were unsuccessful in their findings as they lacked consideration for the roundness on the cutting edge. During the subsequent 15 years, Albrecht [6], Chien [7] and Masuko [8] independently published the influence of cutting edge roundness on process force, material deformation and surface finish and concluded that an appropriate roundness can greatly increase the tool life. Within the last twenty years, publications regarding cutting edge roundness has increased rapidly and revealed that asymmetric edge shape and gradient edge radius can positively influence the cutting and wear mechanisms [9]. Through the modifications of edge microgeometries, cutting tool producers can tailor microgeometry of the tool edge to control the wear mechanism for different cutting conditions.

The process to produce a round cutting edge geometry is known as cutting edge honing. Due to the need for machining challenging materials [9], cutting edge honing has been commercialized as a final step to produce quality cutting tools. Innovative edge honing techniques have been constantly researched to provide alternative ways to increase the performance of cutting tools. However, drawbacks among the techniques limit their implementation in industry. For this reason, a novel edge honing technique is presented in this work to provide an efficient means to edge hone cutting tools.

1.1   Cutting Tools and Mechanisms

There are various types of cutting tools and their geometry depends on machining applications such as drilling, milling and turning. Cutting tools can be either indexable or solid tools. Indexable tools are made of specially designed tool holder and inserts [Figure 1.1]. The inserts, comprised of extremely hard materials such as tungsten carbide, ceramics, cubic boron nitride or diamond are held in a tool holder and are responsible for the actual cutting process. When enough wear accumulates, new inserts can simply replace the existing ones without replacing the tool holder.
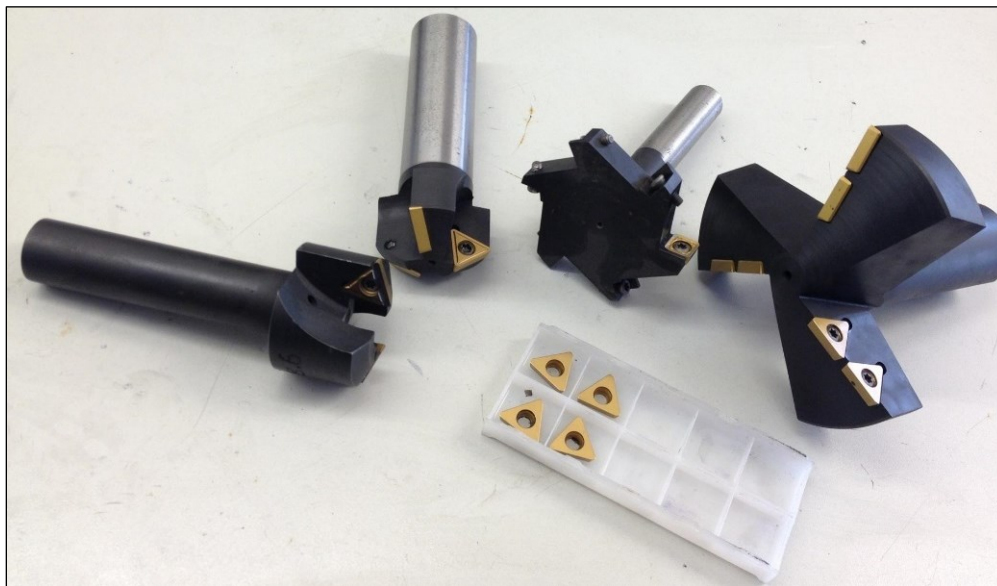
Figure 1.1: Indexable Tooling and Inserts [10].

Modern solid tools are made entirely as one component usually out of high speed steels or cemented carbides [Figure 1.2]. Better machining accuracy relative to the indexable tool is an advantage as clamping of an insert is not necessary. However, it is less cost effective in the long term as tool failure requires a complete replacement.

Figure 1.2: Different Types of Solid Tools [11].

The cutting mechanism remains the same regardless of the cutting tool applications and geometries. Based on the description by Merchant [5], as the tool feeds and moves in the cutting direction, the sharp cutting edge divides the job into chip and workpiece as shown in Figure 1.3. Chip formation is due to shear deformation in the primary shear zone and significant heat is generated due to plastic deformation.
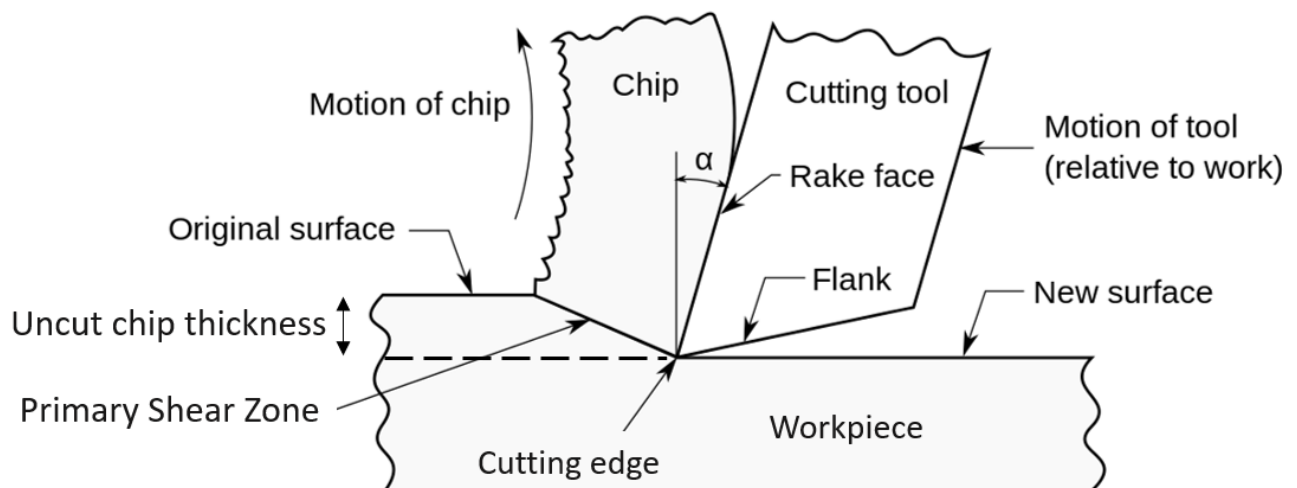
Figure 1.3: Schematic of Orthogonal Cutting [1].

However, it is impossible for the cutting edge to be infinitely sharp as it exerts a high stress concentration at the tool tip. In addition, a sharp edge usually is associated with chipping that causes machining instability. Therefore, a smooth edge profile is usually generated by edge honing technique to remove defects such as chipping, die flash and burrs on the cutting edge, so as to enhance cutting tools performance [Figure 1.4].
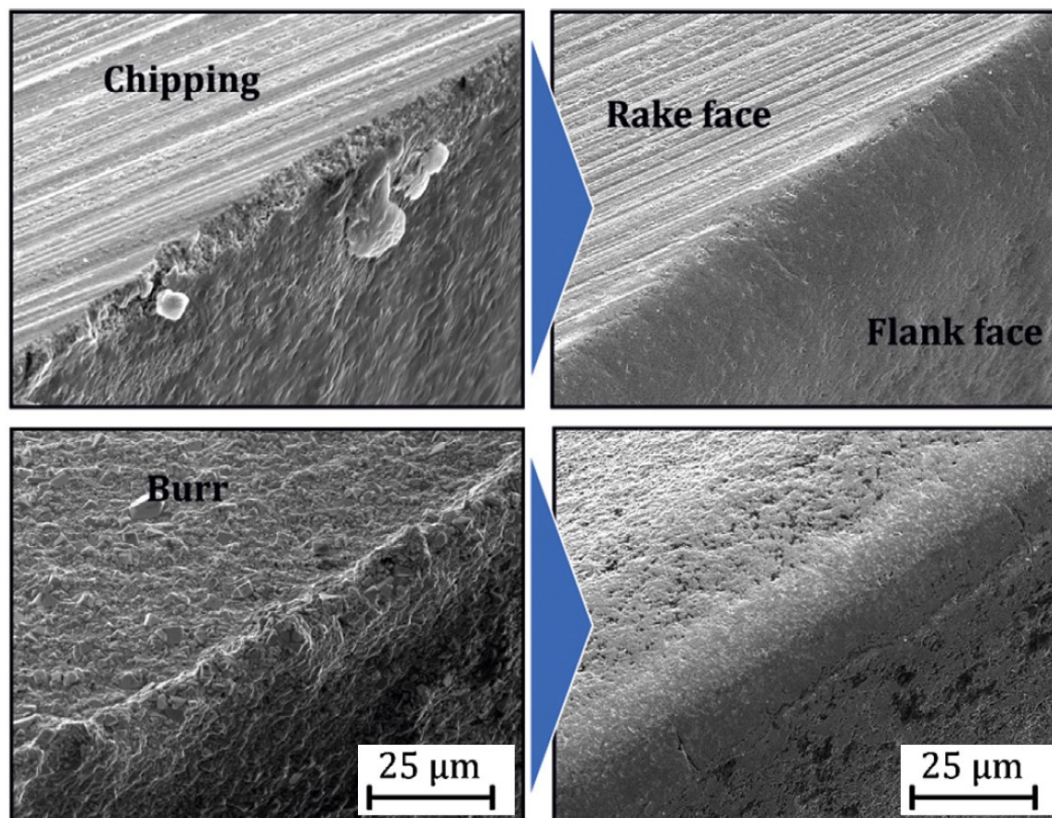
Figure 1.4: Effect of Cutting Edge Preparation [9].

To this end, this thesis presents a new process for edge honing cutting tools using a non-Newtonian abrasive slurry.

1.2   Proposed Edge Honing Process

The primary function of cutting edge honing is to generate a rounded cutting edge and remove imperfections from prior processes such as grinding and pressing. In order to hone the edges of a cutting tool with a complex geometry, a fluid mixed with abrasives could be possibly used as the honing agent, given that such a fluid may easily flow around and conform to the complex geometric contours of such tools. In reference to the tool materials being relatively hard, it is also essential that the fluid used is capable of generating sufficiently high normal stresses in order to force the abrasives against the tool surface and appropriately remove material from the tool edge.

The essential and innovative theme of this thesis is that the fascinating non-Newtonian characteristic of an aqueous cornstarch suspension satisfies the above requirement. Non-Newtonian fluids exhibit to a significant increase in viscosity when they are sheared at certain shear rates or being subject to an impact load. Depending on the mode and rate at which such a suspension is deformed, it is capable of generating normal stress on the order of 1 MPa [12], which is significantly higher than that required (~50 kPa) to support the weight of an adult walking or running atop a bed of such a suspension [Figure 1.5]. If the individual were to stop moving, the cornstarch suspension will revert to the liquid state and the person will sink in. Such a behaviour of the cornstarch suspension may be utilized to remove material and hone the edges of cutting tools, by mixing abrasives in the suspension and using appropriate process kinematics to use abrasion as the material removal mechanism.

Figure 1.5: A Person Walking Across a Pool of Cornstarch Suspension [13].

Non-Newtonian fluids have previously been used in other technology sectors. As shown in Figure 1.6 (a), a hydraulic press extrudes a non-Newtonian abrasive putty through an engine manifold to finish and deburr complex interior passages that traditional deburring tools could possibly not reach. Likewise, Figure 1.6 (b) shows an armor incorporating a non-Newtonian fluid to absorb the momentum of a bullet and prevent it from penetrating through.

(a)   (b)

Figure 1.6: (a) Extrusion Honing of an Engine Manifold with a Non-Newtonian Abrasive Putty [14] (b) Body Armor Absorbing the Momentum of a Bullet [15].

Along similar lines, this thesis will explore the feasibility of using non-Newtonian abrasive slurries comprising an aqueous mixture of cornstarch and abrasives to hone cutting edges.

1.3   Scope of Thesis

The initial focus of the thesis was to understand the thickening behavior of an abrasive-laden cornstarch suspension so as to creatively apply this knowledge to hone cutting edges. An experimental setup was designed and manufactured to realize the novel edge honing process. The setup was then tested in the context of various process kinematics and abrasive slurry compositions to characterize the effectiveness of such a process to hone the cutting edges of inserts as well as solid tools made from both high speed steel and cemented carbides. In particular, the capability of the process to generate symmetric as well as asymmetric cutting edges, and to fabricate edges with a gradient microgeometry along the length of the cutting edge were investigated. On understanding the process mechanisms, the process was applied for the honing of actual industrial tools such as drills, ball-nose end mills and fir-tree root-form end milling tools of a complex geometry to prove the novel process concept.

Chapter 2

Literature Review

Cutting edge honing has become an essential process in the machining sector as it significantly enhances the stability, surface integrity and edge quality of cutting tools. The wear mode of the tool can further be controlled by customizing the microgeometry of the tool edge [1]. Several edge honing processes with specific advantages and limitations have been reported in the literature. In this chapter, the characterization of cutting edges is briefly introduced, which is then followed by a discussion on the mechanisms and limitations of current honing methods. In addition, the properties of non-Newtonian fluids are introduced in the context of the feasibility of their application for edge honing cutting tools.

2.1 Cutting Edge Microgeometry

2.1.1 Cutting Edge Characterization

For a cutting tool with a chamfered edge, the edge geometry may be characterized by the chamfer length l_β and chamfer angle γ_β as shown in Figure 2.1.
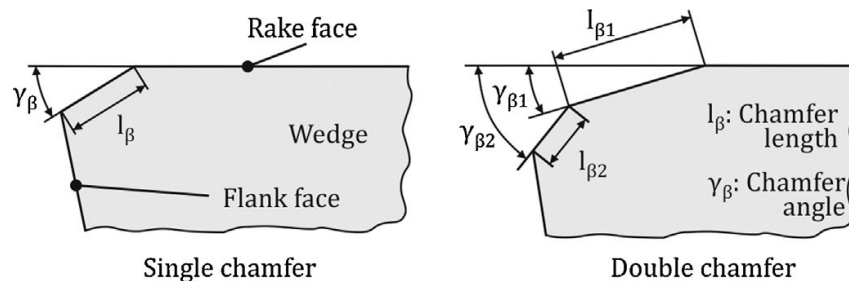
Figure 2.1: Characterization of Single and Double Chamber Edge [9].

A rounded cutting edge is relatively complex to characterize relative to the chamfered edge. In the circle fitting method, a circle is fit in reference to the measured points on the cutting edge [9]. At a minimum, three data points are required to fit a circle. Identification of the start and end points of the rounded edge and the consideration of points to base the circle fit on are however subjective, which can result in significant variability in the deemed edge radius [Figure 2.3].
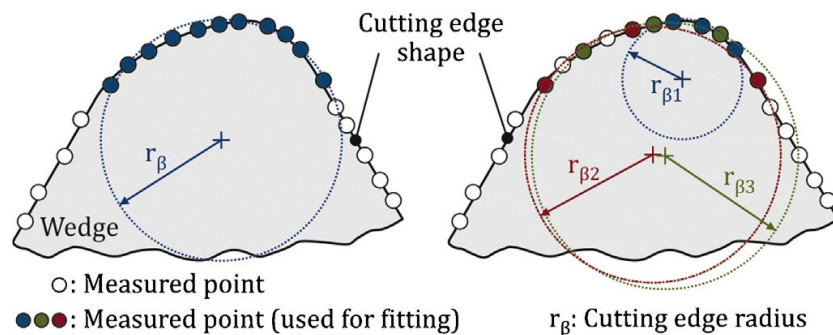
Figure 2.2: Characterization of a Rounded Edge by Circle Fitting Method [9].

24

In order to depict the edge asymmetry, a form factor method has been proposed. The lengths of the rake and flank face segments from the separation points (from where the edge deviates from the rake and flank faces) to the virtual tool tip are measured as S_γ and S_α. The asymmetry of the edge is denoted by the K factor, where K is the ratio of S_γ to S_α. In addition, the profile flattening Δr and apex angle φ are used to characterize the profile [9].

S_α: Cutting edge segment on flank face
S_γ: Cutting edge segment on rake face
$\overline{S}$: Average cutting edge rounding
K (Kappa): Form-factor, K-factor

$$\overline{S} = \frac{S_\alpha + S_\gamma}{2} \qquad K = \frac{S_\gamma}{S_\alpha}$$

Δr: Profile flattening
φ: Apex angle
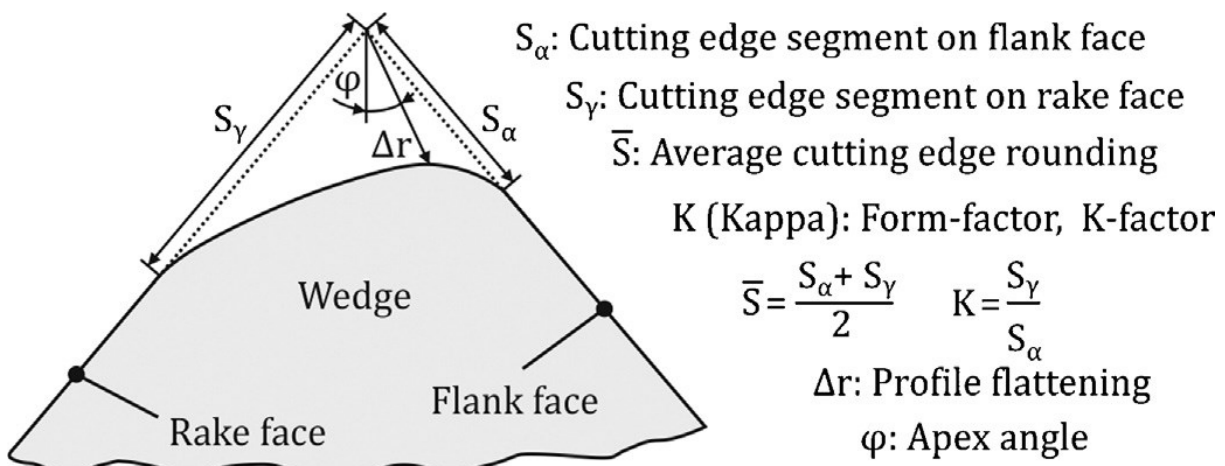
Figure 2.3: Characterization of an Asymmetric Edge Using Form Factor Method [9].

Process parameters may also be taken into consideration to describe the cutting edge geometry as shown in Figure 2.4 [9]. In this method, minimum uncut chip thickness h_{min} and transition uncut chip thickness h_{tr} are used to divide the cutting edge into three sections. They are the contact length on flank L_α, transition length L_{tr} and contact length on rake $L\gamma$. The cutting edge profile is then interpolated in consideration of these lengths.
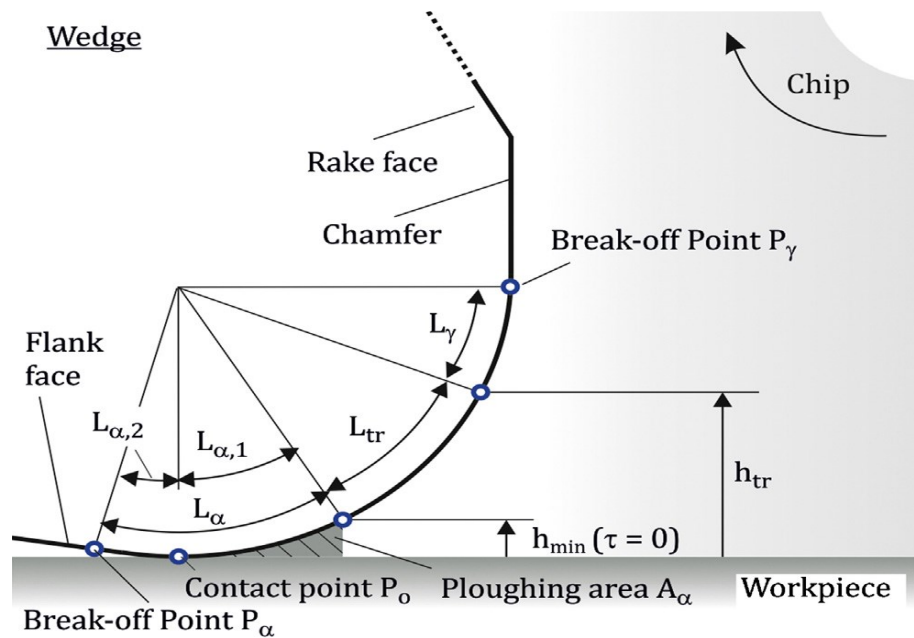
Figure 2.4: Characterization of a Cutting Edge by Considering Process Parameters [9].

2.1.2 Effect of Edge Microgeometry on Cutting

The shearing process in cutting is significantly affected by the edge radius. The optimal cutting edge radius is determined by couple of factors. First, the feed force and cutting force increase linearly with the cutting edge radius, however, the feed force is more significantly influenced. Deflection of the workpiece and excessive stress on cutting tools can be caused by the higher process forces. The increased process force is due to the difficulty associated with material shearing. As seen in Figure 2.5, material removal is diminished at the primary shear zone when the ratio of the uncut-chip thickness to cutting edge radius decreases. Material is ploughed underneath and to the sides of the cutting tool instead of being sheared into chips. Furthermore, the thermal load is increased by the additional plastic deformation at the shear deformation zones. On the other hand, stability and heat dissipation are improved by the increase in the size of the cutting edge

radius, given that the stress concentration at the tool tip is minimized and the surface area available for heat conduction is increased.
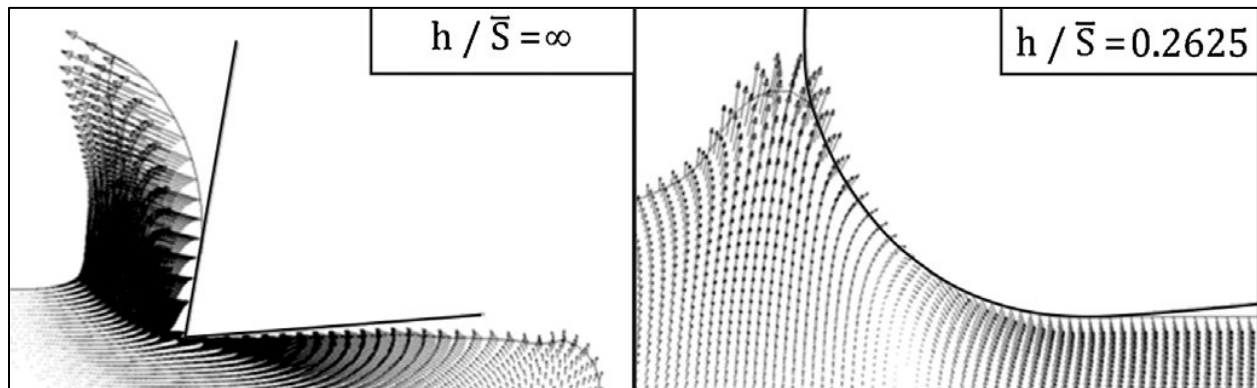
Figure 2.5: Effect of the Ratio of the Uncut-chip Thickness to the Cutting Edge Radius [9].

The mode and extent of tool wear can also be controlled by an appropriate design of edge asymmetry. With increasing S_γ the thermal and mechanical loads are shifted from the flank face to the rake face, which gives rise to increased crater wear, as shown in Figure 2.6 [9]. Likewise, with an increase in S_α more material is deformed against the flank face causing a rise in thermal and mechanical loads therein, which consequently increases flank wear. Figure 2.7 shows the rake and flank temperatures for various combinations of edge geometry asymmetry relative to a symmetric edge.
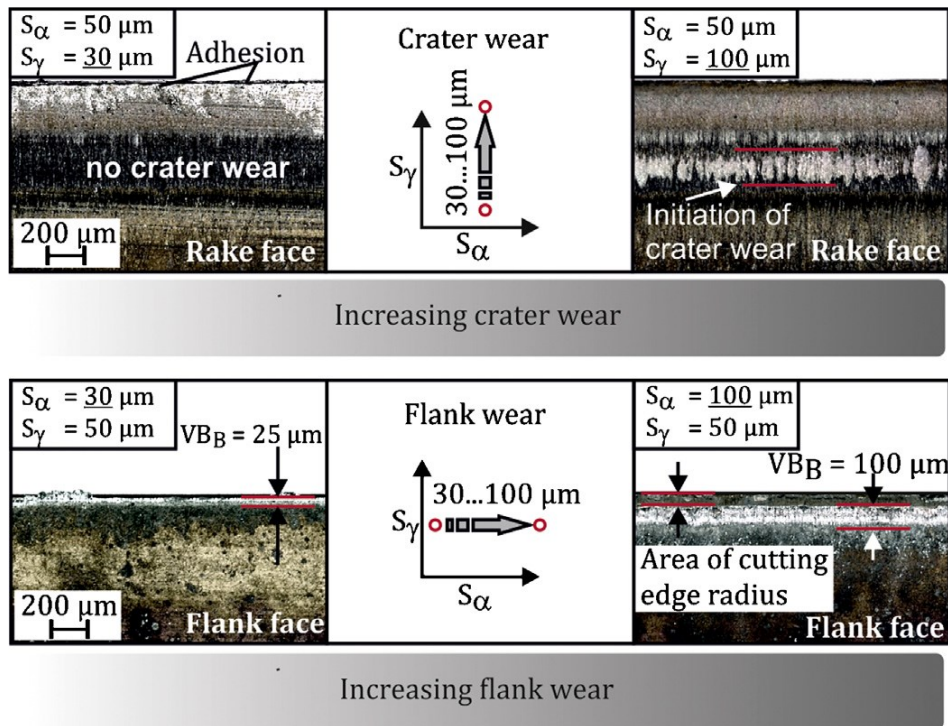
Figure 2.6: Dominant Wear Depends on the Edge Asymmetry [9].
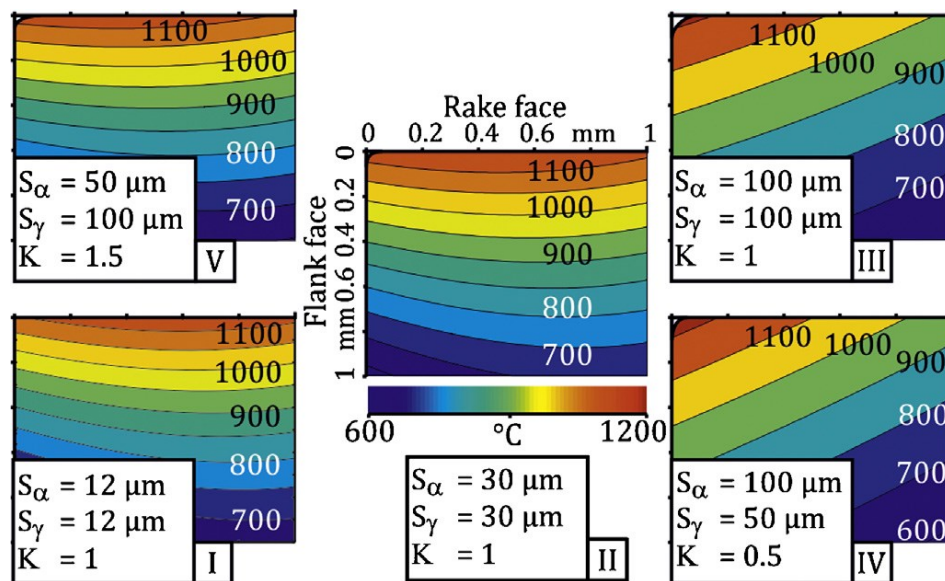
Figure 2.7: Temperature on the Tool's Location Depends on the Edge Asymmetry [9].

2.2   Cutting Edge Honing Processes

The use of low quality tools with imperfect or flawed edges may cause frequent and catastrophic tool failure that leads to low manufacturing productivity. The microgeometry of the edge can be customized to control the dominant wear mechanism. For example, flank wear can be redistributed to the rake face by increasing the rake segment of the edge as mentioned in Section 2.1, and vice versa. Cutting edge honing process aims to manipulate the edge geometry in order to increase the edge integrity and tailor the tool to specific cutting conditions. Common processes for cutting edge honing include brushing, micro abrasive jet blasting and drag finishing. These and other less common but novel methods are discussed in this section. Their advantages and limitations are then identified, to lead into the motivations for the present work.

2.2.1   Brushing

Brushing is one of the most common techniques to edge hone a cutting tool. During this process, a rotating disk or wheel with abrasive filaments is brushed against the cutting edge to remove material. There are two types of brushes: ones with steel wires and others with nylon abrasive filaments (NAF) [16]. Steel wire brushes are slowly losing their acceptance in industry as the wire tip can pose a detrimental effect to the surface integrity of the edge [17]. NAF is used to prepare the cutting edge [Figure 2.8] due to its finer material removal mode and the associated finer finish. The wear of NAF is relatively more stable than steel wire. This is due to new sharp edges of the abrasive grains that are constantly being exposed as they wear [16]. The abrasive material on the filament of NAF

can be silicon carbide (SiC), aluminum oxide (Al_2O_3), cubic boron nitride (CBN) or poly crystalline diamond (PCD). The performance of the brushing process can be controlled by adjusting the brushing parameters such as rotational speed, feed rate and depth of cut [9], [16], [18]. Moreover, asymmetry can be produced by adjusting contact conditions such as brushing angle and direction. Tools with a complex geometry can also be honed but this requires the use of a 5-axis machine tool which adds to the cost [9].
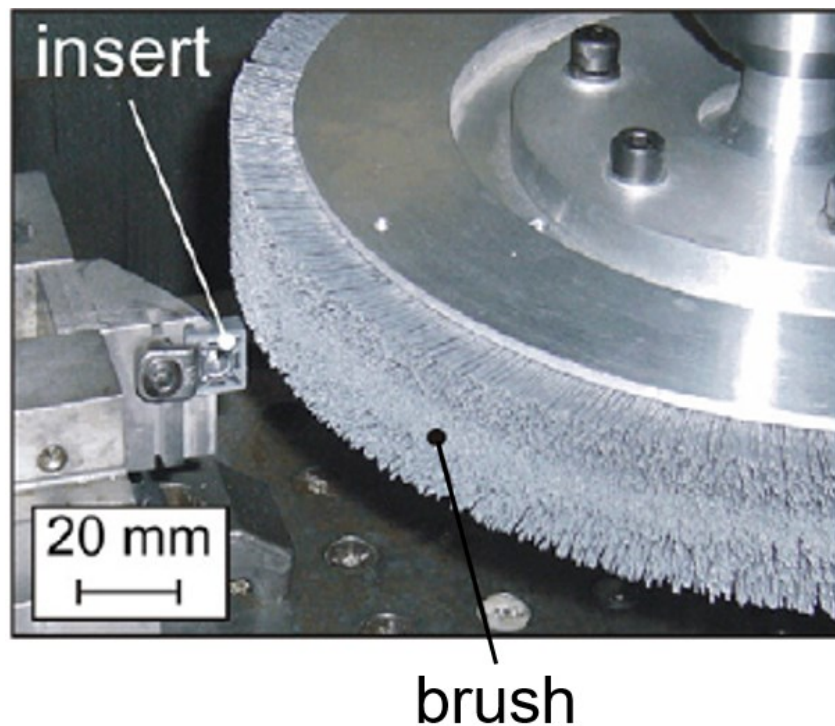
Figure 2.8: Brush Honing an Insert with NAF [18].

High brushing speed often leads to high temperatures and damages the filaments. As a result, the material removal rate can be dramatically decreased [18]. Overuse of a brush can also decrease the honing quality and edge radius as shown in Figure 2.9.
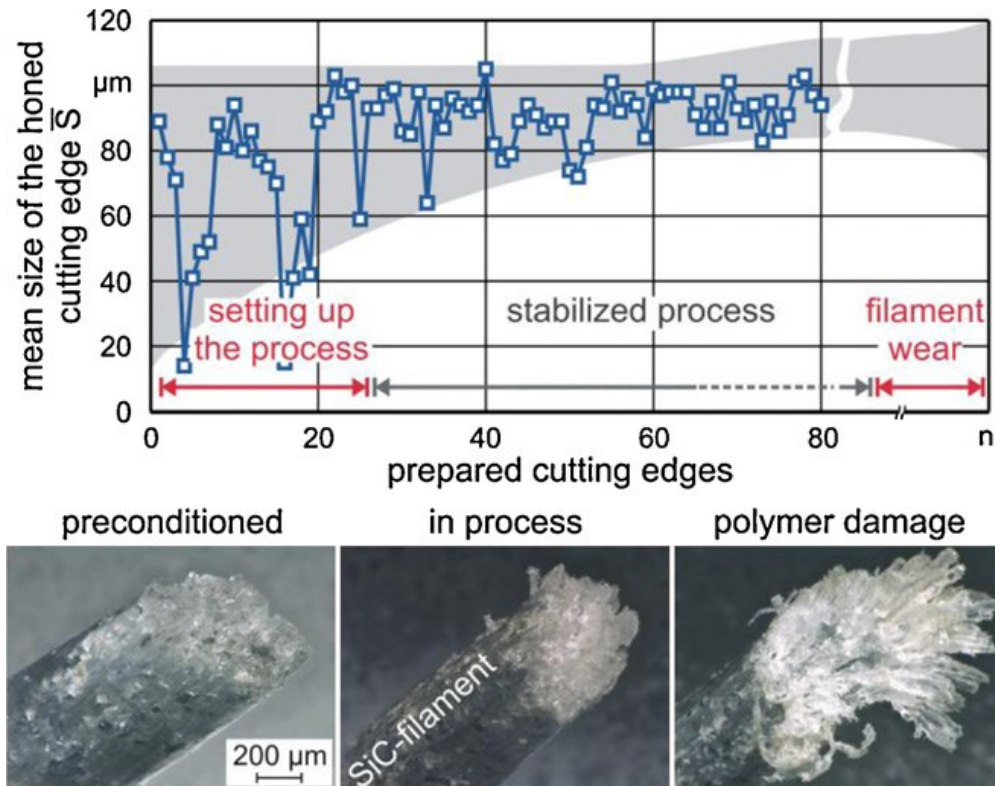
Figure 2.9: Wear Stages of a NAF Filament when Honing Inserts [19].

Currently, there is no effective method to detect the wear on the filament [9] and the process control has yet to be developed due to the complexity of modelling the material removal mechanism [16]. Brush honing is also limited when preparing tools with an intricate geometry with nearly enclosed features, as the filaments cannot reach this space. Due to this, these tools may still contain defects after brush honing [9].

2.2.2 Abrasive Jet Machining (AJM)

Abrasive jet machining (AJM) also known as micro blasting, has a wide range of usage from machining to surface finishing. There are two types of AJM: dry and wet. In dry AJM, pressurized air mixed with abrasives is accelerated through a nozzle to hone the cutting

tool whereas pressurized air is replaced with water in wet AJM [9]. The material removal is due to the erosive action of the abrasives impinging on the workpiece. Figure 2.10 shows a typical AJM set-up. The nozzle is positioned so that it has a blasting angle α_{st} [20]. When α_{st} is set to 45° a symmetric edge with a form factor K = 1 can be achieved. The nozzle may be shifted to control the level of erosion on the major and minor cutting edges. The level of rounding can be controlled by adjusting the jet pressure and preparation time. A low jet pressure can remove defects on the cutting edges, but not the grinding marks. A higher jet pressure can produce a lower surface roughness and remove grinding marks. A high quality edge rounding can be achieved in a relative short machining time in this process. However, focused erosion of the tool edge can cause selective removal of carbide particles, and lead to premature flaking of the coating [21]. The implementation of jet blasting to hone tools with a complex geometry is problematic since there are numerous process parameters to control in this process.
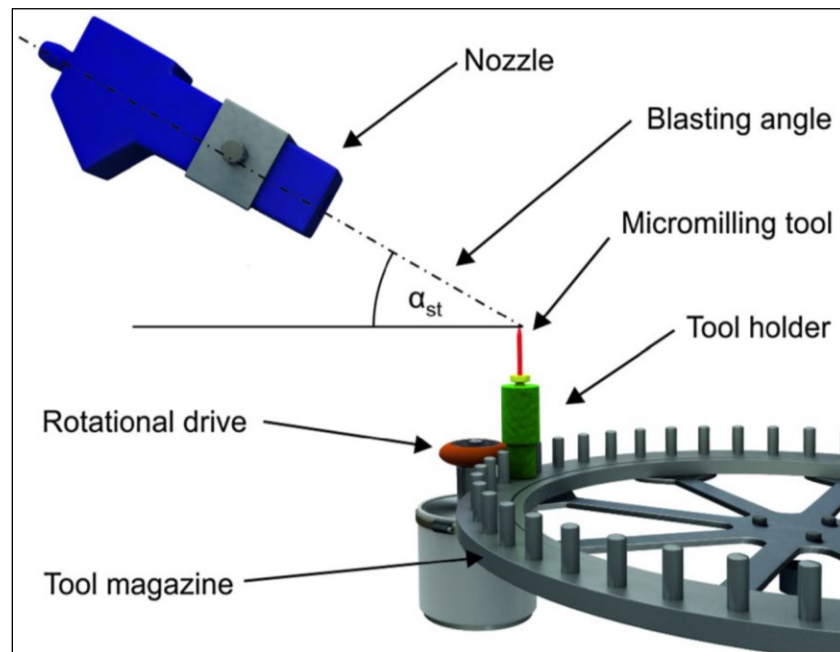
Figure 2.10: Wet Abrasive Jet Honing of a Micro-milling Tool [20].

2.2.3 Drag Finishing

In drag finishing, workpieces are usually moved through a bath of free abrasives while being held by a fixed track device to avoid collision between parts [9] to deburr and enhance surface finish [Figure 2.11] [22]. Material removal is caused by the relative motion between the abrasives and workpieces. Higher material removal rate can be achieved by increasing the workpiece velocities [22]. Cutting edges may be honed using drag finishing; however, the resultant radius along the cutting edge is often not homogenous because there is no control of localized interaction between the abrasives and the cutting edge. Modelling of the process requires expensive measurement devices and is time-intensive [22]. Unless there is a model that can accommodate various cutting tool geometries and material, precise control of microgeometry on the cutting edge is difficult.

Figure 2.11: Drag Finishing [23].

2.2.4 Laser Machining

A pre-defined edge radius can be accurately produced by laser machining on tools made from a difficult-to-machine material [24]. The process has been shown to be capable of generating edges with a radius from 9 μm to 47 μm with an accuracy of 1.5 μm on a straight edge insert in about 10 seconds. A diode-pumped solid state laser marking machine combined with a 5-axis movement has been used in the work above to hone the cutting edge. A beam with a gaussian energy distribution is used to ensure that the lasered and non-lasered regions refer to a smooth transition. In addition, short laser pulses are used as it can produce a higher surface integrity than long laser pulses. As a result, the material can be heated up more rapidly to evaporation point to prevent the conduction of energy into the subsurface that could detrimentally alter its material properties. The thermal loads would however sustain tensile residual stress which could result in catastrophic tool failure [9]. Moreover, honing a tool with a complex geometry would necessitate precise positioning of the laser head relative to the tool edge.

2.2.5 Electro-Erosion Edge Honing (EEEH)

In sink electrical discharge machining (EDM) sharp edges are rapidly rounded off as shown in Figure 2.12 [25]. This phenomenon is exploited in the electro-erosion edge honing (EEEH) technique, in which the cutting insert is used as the tool. As a result, the sharp edges on the cutting tool is rounded off as shown in Figure 2.12.
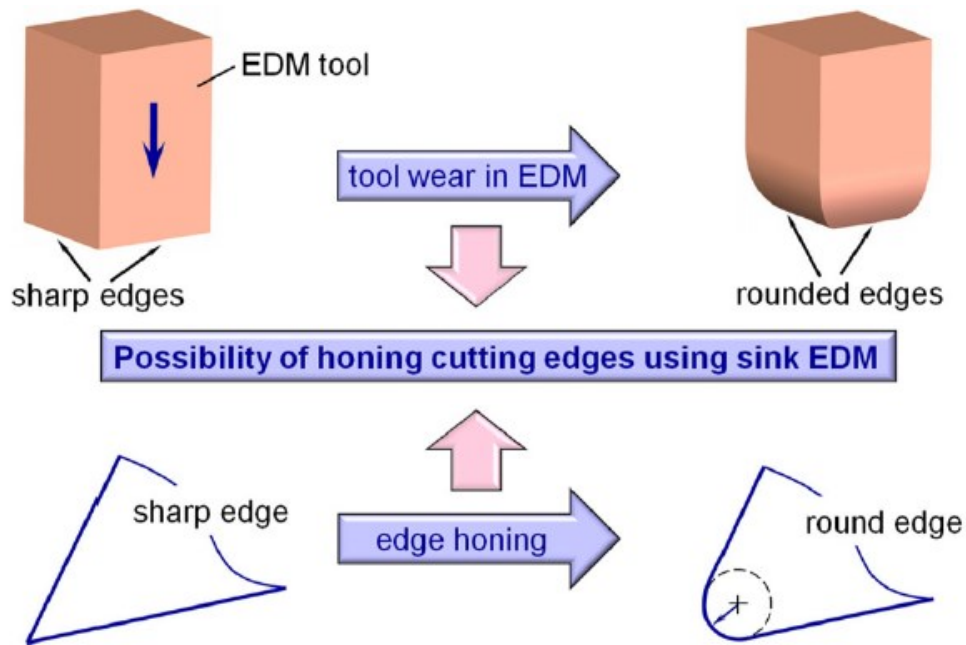
Figure 2.12: Principle of Electro Erosion Edge Honing [25].

The hardness of the cutting tool is not a limiting factor by this method since material is removed by melting and vaporization rather than shearing. Moreover, since only a small volume of material is required to be removed from the edge, the process is very rapid although the material removal rate of EDM is relatively low compared to conventional processes. The process can be controlled by adjusting the machining parameters such as current, on time and the counterface material [25].

An uniform and symmetrical cutting edge can be produced by feeding the cutting insert symmetrically into the counterface [25]. In addition, cutting edge microgeometry can be altered by changing the kinematic of the process: rotation about the X-axis can produce a variable radius along the edge and rotation about the Z-axis can produce asymmetric edge radius as shown in Figure 2.13. Given the thermal means of material

removal, the honed edge may be expected to be subject to undesired tensile residual

stresses [11].
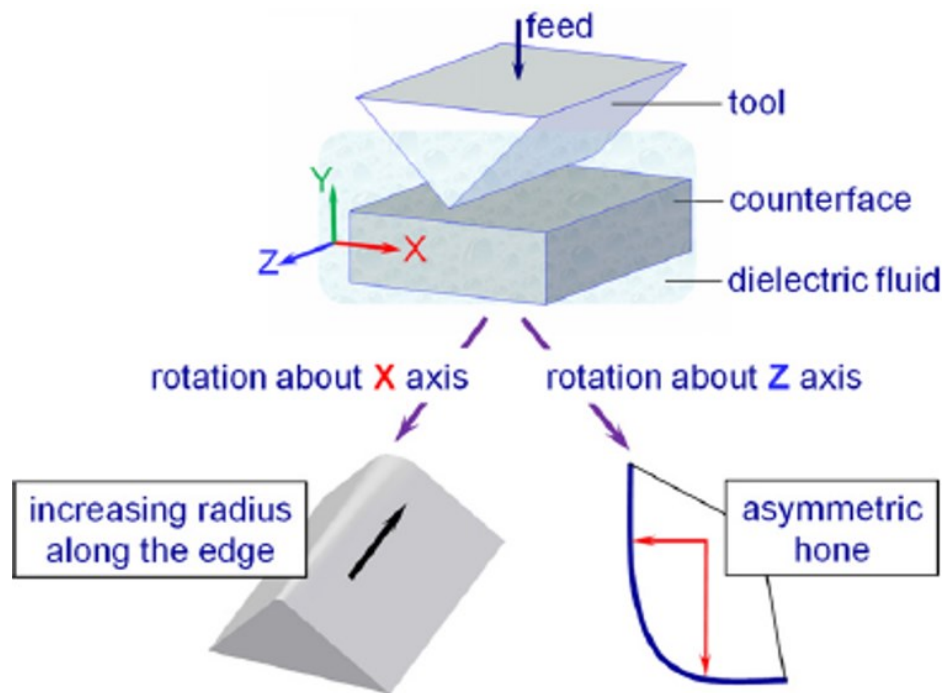
Figure 2.13: Production of Asymmetric and Gradient Edges Using EEEH [25].

2.2.6 Elastic Bonded Superabrasive Grinding

In this process, an elastic bonded polishing wheel is substituted in place of a regular

grinding wheel to hone the cutting tool as shown in Figure 2.14 [26]. The cutting edge

roundness and asymmetry can be altered by changing the depth of cut and the grinding

path of the polishing wheel. The normal force in the grinding wheel bond is increased with

the depth of cut as there is more elastic deformation at the point of honing. As a result,

the material removal rate is increased. Asymmetry can also be achieved by adjusting the

chamfer angle Y_b as shown in Figure 2.14. When Y_b is decreased, the rake face of the

tool has a greater material removal rate and a cutting tool with an asymmetry can be

produced. However, due to the elastic property of the elastic bonded superabrasive wheel, there will be material pile up on the rake face. Thus, a symmetrical edge radius cannot be produced when the grinding path is parallel to the chamfer since the pile up stacks on the rake face. This can be addressed to some extent by further adjusting the grinding path.
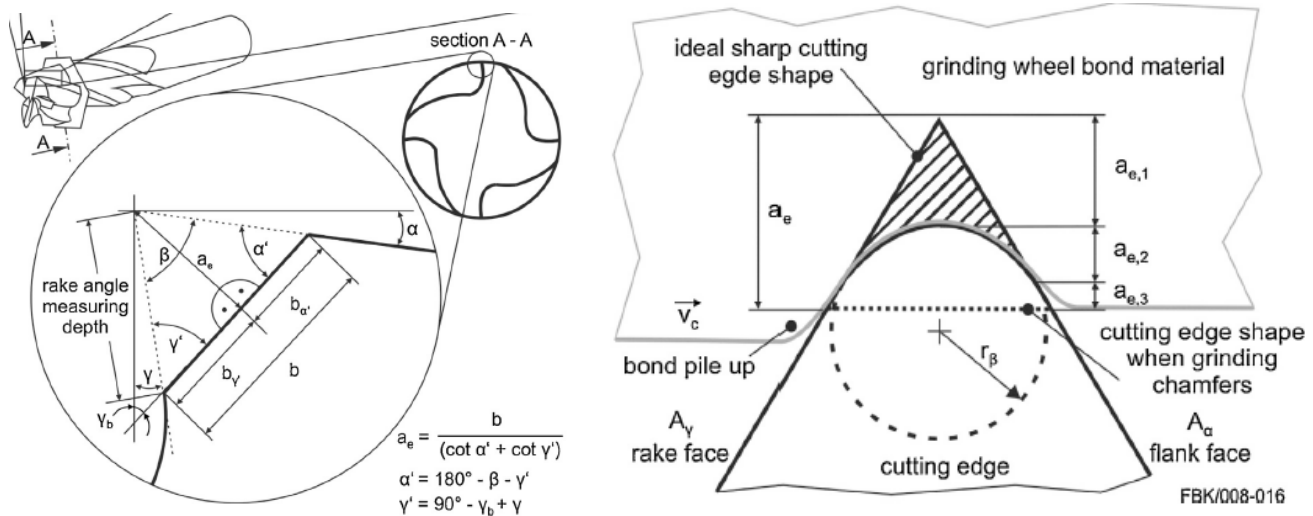
Figure 2.14: Elastic-Bonded Superabrasive Grinding [26].

There are limitations to the elastic superabrasive grinding method. In the case of end mills, only the peripheral cutting edges of the tool is targeted and edges away from the periphery are completely neglected. Supplementary edge honing technique is hence needed to hone the rest of the cutting tool. In addition, since the pile up stagnates on the rake face, it limits the ability to remove material on the flank side.

2.2.7 Abrasive Flow Machining (AFM)

Abrasive flow machining (AFM) is a process that is commonly used to deburr and increase the surface finish of workpieces with a complex geometry. Semi-sold media mixed with abrasives is extruded from the inlet to outlet in a passage and the workpiece is held in a fixture along its path as show in Figure 2.15 [27]. The media usually consists of a polymer (e.g. styrene butadiene rubber) and lubrication oils. The passage could either be one-way, two-way or orbital. When the media is extruded, the pressure difference between the inlet and outlet pushes the abrasive to move inside the passage. As the abrasives glide against the surface of the part, material removal happens. The outcome of the process is dependent on the part orientation and the composition of the media. This process has been extended to hone cutting edges with edge radii ranging from 10 to 60 µm [28]. The process performance is somewhat difficult to predict as the flow inside the passage is intricate [27], and the process capability is limited when honing asymmetric edges [9].
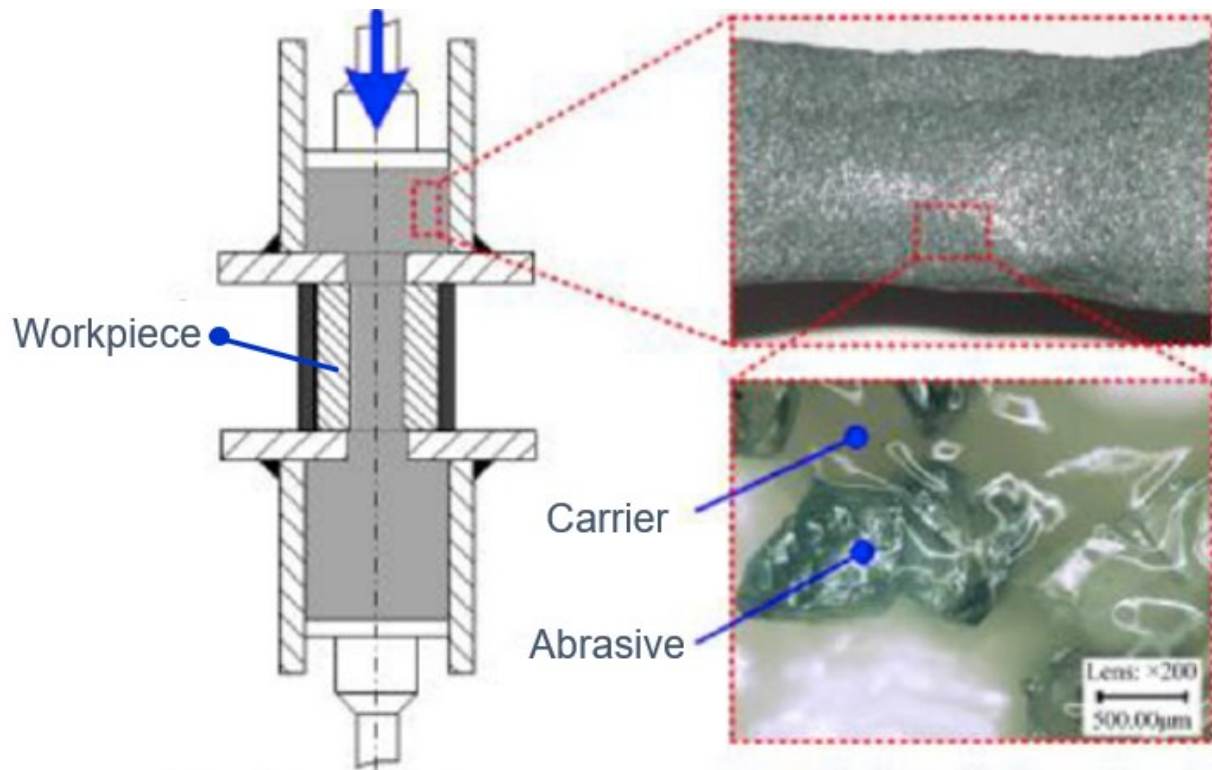
Figure 2.15: Abrasive Flow Machining [27].

2.2.8 Magneto Abrasive Machining (MAM)

Magneto-abrasive machining (MAM) is a process that uses abrasives suspended in a magnetic fluid for surface finishing. This has also been applied for edge hone drilling tools in a setup similar to drag finishing [29]. The experimental setup consists of an inner and outer boundary that rotate coaxially about an axis [Figure 2.16]. Drilling tools are held in a rotating spindle and situated in between the boundaries filled with the magnetic abrasive slurry. A magnetic field is then applied which forces the abrasives to apply pressure on the tool edge to hone it.
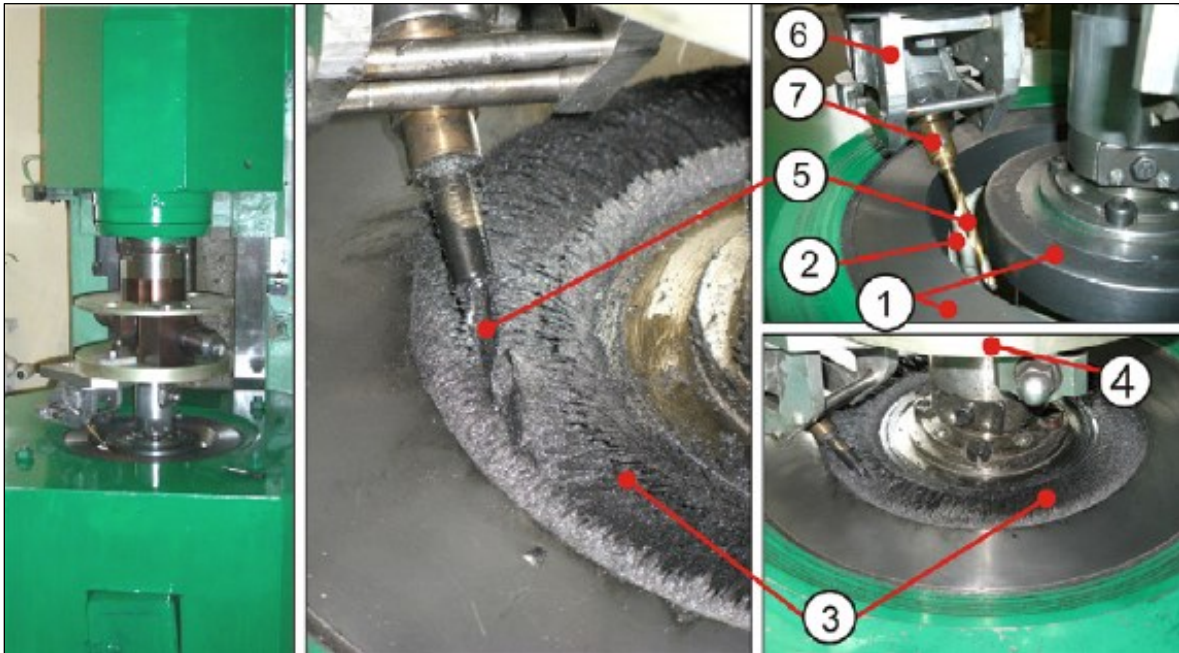
Figure 2.16: Magneto Abrasive Machining [29].

The abrasive type and size both play an important role in this edge honing process. It is found that the splintering-type abrasive powder with smaller grain size produces a lower average edge chipping and produces the best honing performance. The splintered shape abrasives have sharper edges that remove material more efficiently as compared to blocky abrasives.

2.2.9   Cutting Edge Honing in Liquid Abrasive Bath

This technique is described in a patent that teaches honing of a cutting edge using a liquid bath with suspended abrasives [30]. The liquid media is circulated in a circular container and it can be water, soap or other media that can be easily circulated. The cutting edge of the tool is submerged into that bath and displaced either along or against the bath flow

about the center axis of the container; the tool rotates about its own axis but against the cutting direction.

As show in Figure 2.17, the abrasive media flows into the rotating tool with velocity (V_{M1} and V_{M2}) causing the abrasives to apply pressure on the cutting edge and initiate the honing process. The tool in this case rotates in a counter-clockwise direction and has a tangential velocity (V_{C1} and V_{C2}) of same magnitude but opposite directions. The resultant velocity V_{R1} is greater than V_{R2} which causes a greater material removal at the flank face at V_{R1} and vice versa for the rake face at V_{R2}. As a result, this honing method is favourable to produce an edge radius with a form factor K < 1.
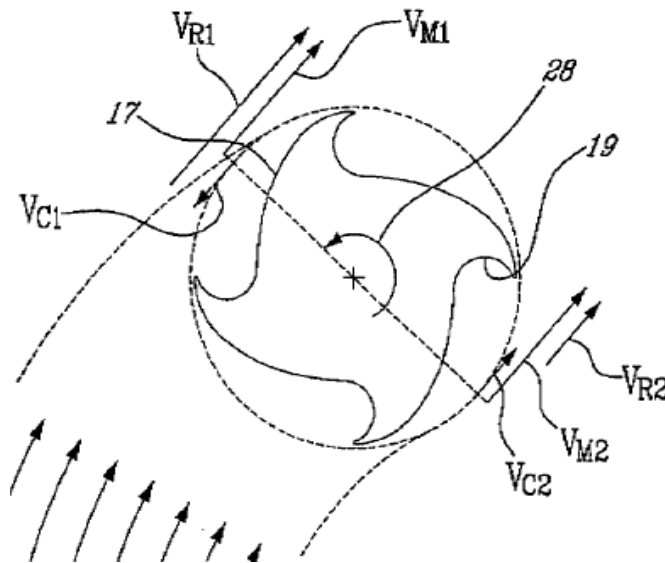
Figure 2.17: Kinematics of Cutting Edge Honing in a Liquid Bath with Abrasive Media [30].

2.3   Non-Newtonian Fluids

As can be seen in several videos on social media, an aqueous suspension of cornstarch is able to "thicken" significantly that allows people walk to or run across it [Figure 2.18] but they start to sink in when they remain still. This interesting phenomenon has gained interest from different technology sectors as the suspension can transform itself reversibly into a solid-like state based on the mode in which it is loaded. Many commercial products have utilized this property of non-Newtonian fluids in such products as skis, tennis rackets and flexible body armor [31]. In a recent publication, a non-Newtonian fluid has been used to absorb vibration by exploiting its viscoelastic property [32]. In the next section, fundamentals of fluid flow are revisited and the current understanding of the science behind this "smart" fluid is reviewed.

Figure 2.18: A Person Walking Across a Pool of Non-Newtonian Fluid without Sinking [33].

2.3.1   Fundamentals of Fluid Flow

A fluid is defined as a substance that is continuously deformed under the influence of a shear force [34]. When a surface is in contact with the fluid, the fluid at the point of contact is subject to the no slip condition. As shown in Figure 2.19, a fluid element is deformed when the top part of the fluid element moves at the same velocity δu as the top plate while the bottom part stays stationary with the bottom plate.
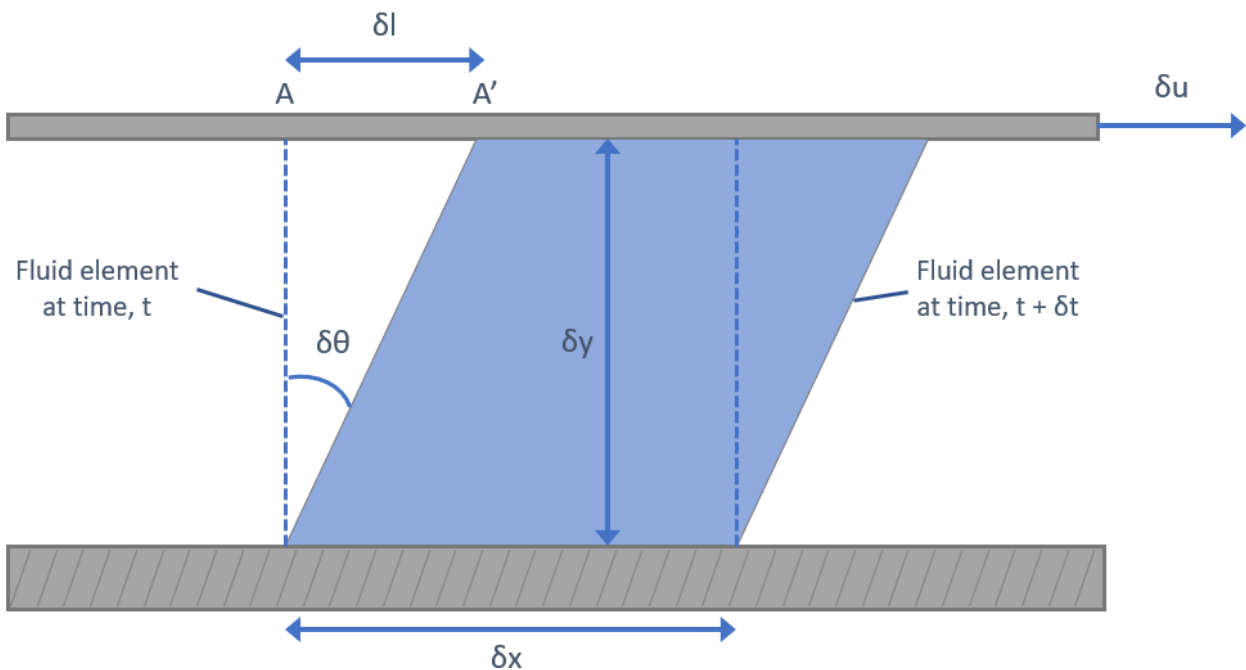
Figure 2.19: Shear of a Fluid Element due to Shear [34].

$\delta\theta$ is the deformation of the fluid and let $\dot{\gamma}$ be the deformation rate:

$$\dot{\gamma} = \lim_{\delta t \to 0} \frac{\delta\theta}{\delta t} = \frac{d\theta}{dt} \tag{2.1}$$

To find $\delta\theta$:

$$\lim_{\delta t \to 0} \tan\delta\theta = \frac{dl}{dy} \tag{2.2}$$

Since $\delta\theta$ is small:

$$d\theta = \frac{dl}{dy} \tag{2.3}$$

Also,

$$\lim_{\delta t \to 0} \delta l = \lim_{\delta t \to 0} \delta u \cdot \delta t \tag{2.4}$$

$$dl = du \cdot dt \tag{2.5}$$

Sub 3 and 5 into 1, we obtain the deformation rate or shear rate $\dot{\gamma}$:

$$\dot{\gamma} = \frac{du}{dy} \tag{2.6}$$

The shear stress of a fluid element is proportional to the deformation rate:

$$\tau = \mu\dot{\gamma} \tag{2.7}$$

where μ is the viscosity of the fluid. Viscosity is defined as the resistance of a fluid to deformation or shear [34]. For a Newtonian fluid, μ is constant and an inherent property of the fluid, and so the shear stress is proportional to the shear rate. On the other hand, the relationship between the shear stress and shear rate for non-Newtonian fluids is:

$$\tau = \eta\dot{\gamma} \tag{2.8}$$

where the apparent viscosity η is given by:

$$\eta = k|\dot{\gamma}|^{n-1} \tag{2.9}$$

k and n are defined as the flow consistency index and flow behaviour index respectively, and can be determined experimentally. As shown in equations 2.8 and 2.9, for a non-Newtonian fluid, the shear stress is not directly proportional to the shear rate as $n \neq 1$. A

few examples of non-Newtonian fluids are cornstarch suspension, ketchup and toothpaste. As shown in Figure 2.20, when n = 1, the fluid is Newtonian so that the apparent viscosity is constant. If n < 1, the apparent viscosity decreases with increasing shear rate and it is called shear thinning or Pseudoplastic fluid. In contrast, when n > 1 the viscosity increases with increasing shear rate and it is known as a shear thickening or a dilatant fluid.
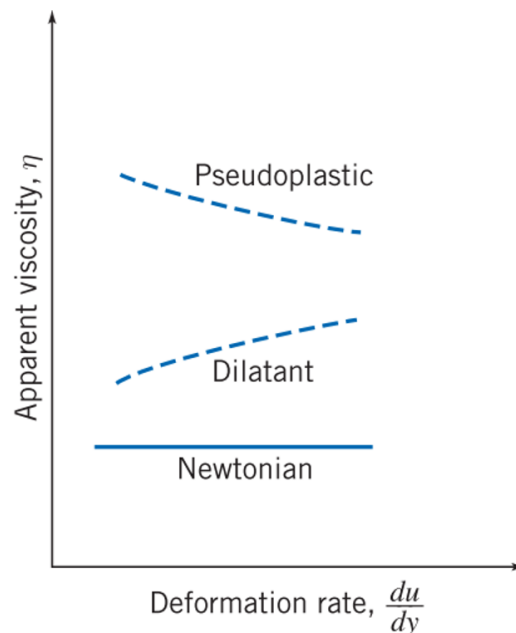
Figure 2.20: Apparent Viscosity vs Deformation Rate of Newtonian, Dilatant and Pseudoplastic Fluids [34].

        In order to determine the material properties of a fluid, rheology testing is performed. The meaning of "rheo" is "flow" in Greek and "ology" is "the study of" [35], so rheology is the study of the flow and deformation of a material. It provides a better understanding of the properties of fluids such as viscosity, viscoelastic behaviour, thixotropic effect etc. Rheology testing is usually performed with a rheometer. The fluid is

placed between a stationary and a rotary surface, so that the fluid is sheared as shown in Figure 2.19.

As seen in Figure 2.21, the two surfaces may correspond to different geometries such as concentric cylinders, cone-and-plate and parallel plate, depending on the testing requirements. The rotary part, "bob" can be rotated to pre-programmed conditions and the resistance of the fluid to the deformation is measured. Based on the geometry of the setup, the shear stress, shear rate and viscosity can be calculated.
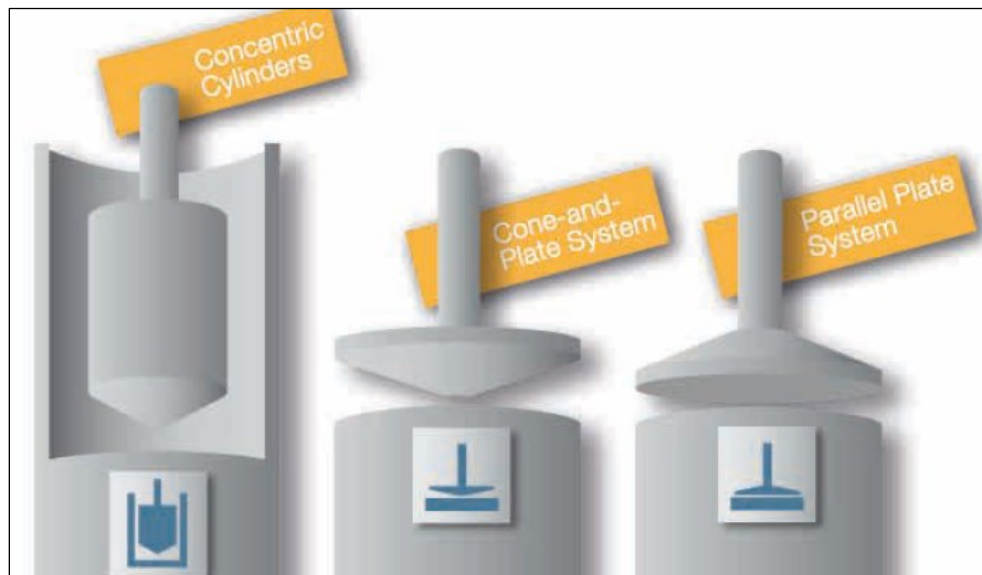
Figure 2.21: Different Geometric Setups for Rheometer [36].

2.3.2 Viscosity of Non-Newtonian Fluids

Typically, there are two distinct regimes for non-Newtonian fluids when plotting the viscosity against the shear rate [Figure 2.22] [37]. At relatively low shear rate, shear thinning is dominant, and shear thickening is observed when a critical shear rate is exceeded. The critical shear rate is defined as the rate at which the fluid transitions from

thinning to thickening regime, and it is inversely proportional to the percentage of particles in the suspension.

In the shear thinning regime, particles streamline as layers and causes a decrease in viscosity as they flow smoothly against each other [Figure 2.22]. In the shear thickening region, the stress is high enough to bring the particles to collide with each other [Figure 2.23]. As the fluid between the particles are being squeezed out, the hydrodynamic pressure rises. This lubrication hydrodynamic force increases inversely with the distance between the particles [37]. The particles are held together by a strong lubrication hydrodynamic force and hydrocluster is formed as they collide. The flow is impeded by these hydroclusters and leads to an increase of energy dissipation and viscosity [Figure 2.22]. When the shear stress is disbanded, the formation of hydroclusters is dissolved and the suspension can reverse from a shear thickened state to the equilibrium state.
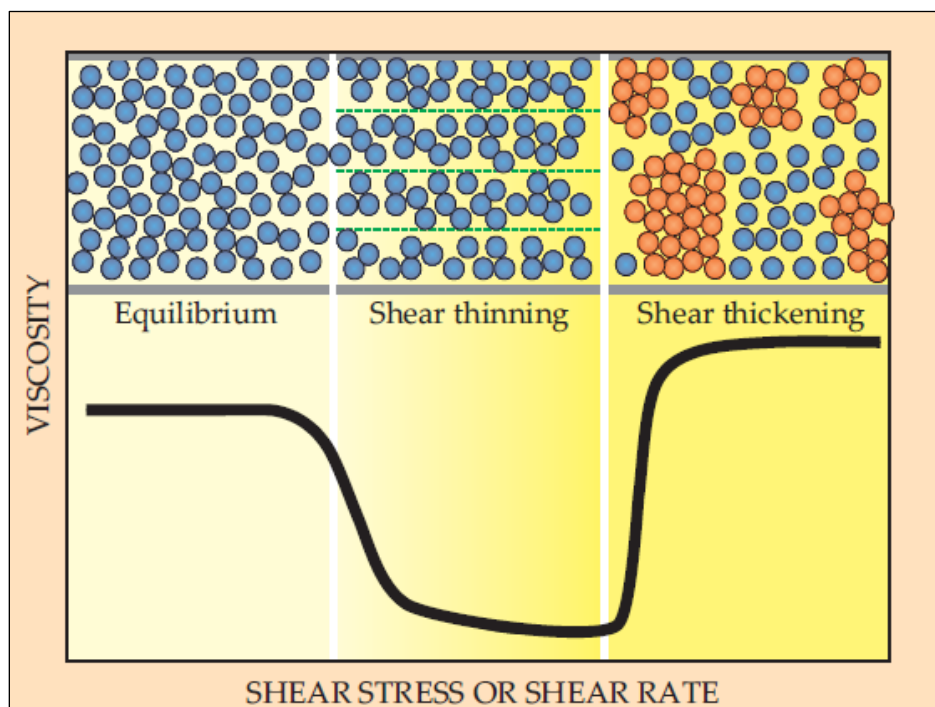
Figure 2.22: The Viscosity of a Shear Thickening Fluid at Different Stress States [37].
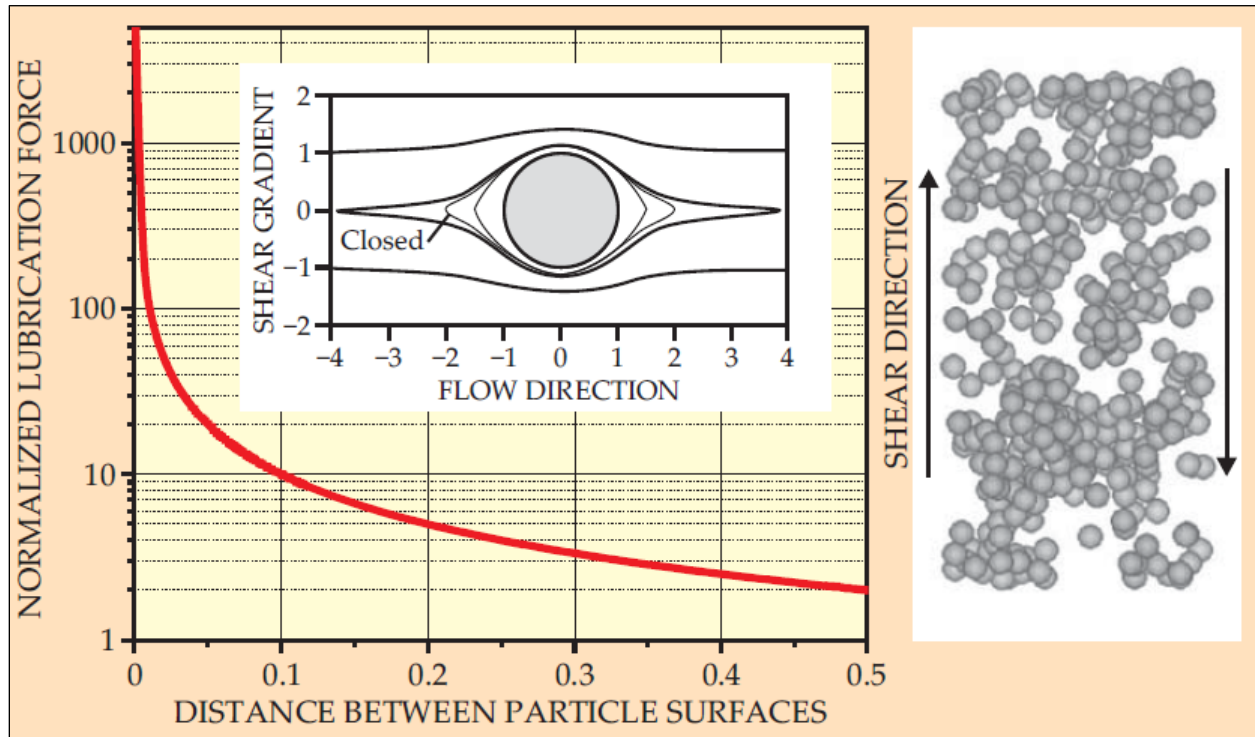
Figure 2.23: Collision of Non-Newtonian Particles to Form Hydrocluster due to Shearing [37].

2.3.3 Shear Thickening

Cornstarch-water suspension is a non-Newtonian fluid. Its viscosity has been reported for different weight percentages of cornstarch at various shear rates. As shown in Figure 2.24, an abrupt increase in viscosity was noticed when the weight percentage reached 52.5% [31]. This dramatic increase of viscosity is denoted as discontinuous shear thickening (DST) where the cornstarch appears to be "jammed". DST was not observed when using refined cornstarch even though the refined and bulk cornstarch have a similar particle diameter (Refined: 15.0 ± 4.2 μm, Bulk: 15.8 ± 4.7 μm). A possible explanation for this would be that the bulk cornstarch corresponds to a larger size deviation that allows for the particles to be more tightly compacted [2].
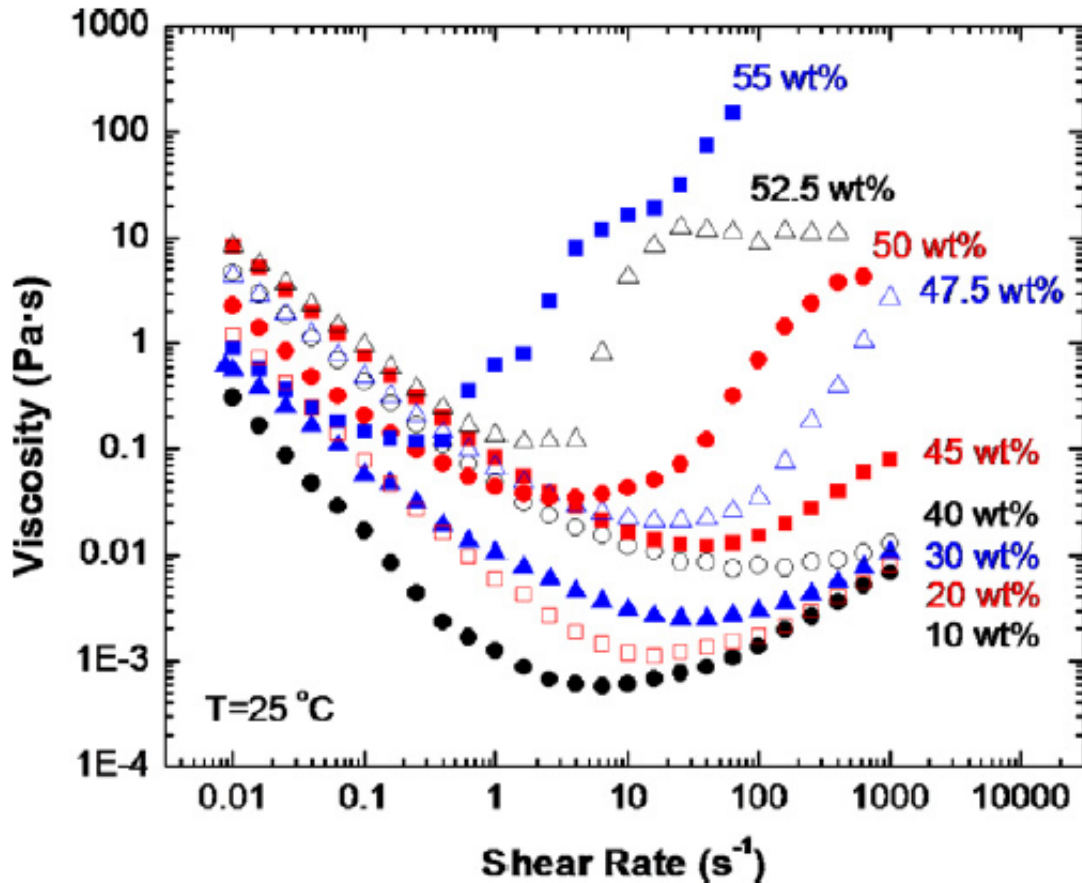
Figure 2.24: Steady State Shear Rate Ramp of Cornstarch Suspension at Different Weight Percentages [31].

In order to determine the percentage of cornstarch needed for an average adult to walk or run across the suspension, the average stress required is about 50 kPa. However, the measurement device could only measure a shear rate up to 10 kPa and the rest of the data was extrapolated as shown in Figure 2.25 for both refined and bulk cornstarch. Based on the result, it was concluded that the applied stress from a walking/running adult would result in a viscosity of 55 and 270 Pa·s in the bulk and refined cornstarch respectively.
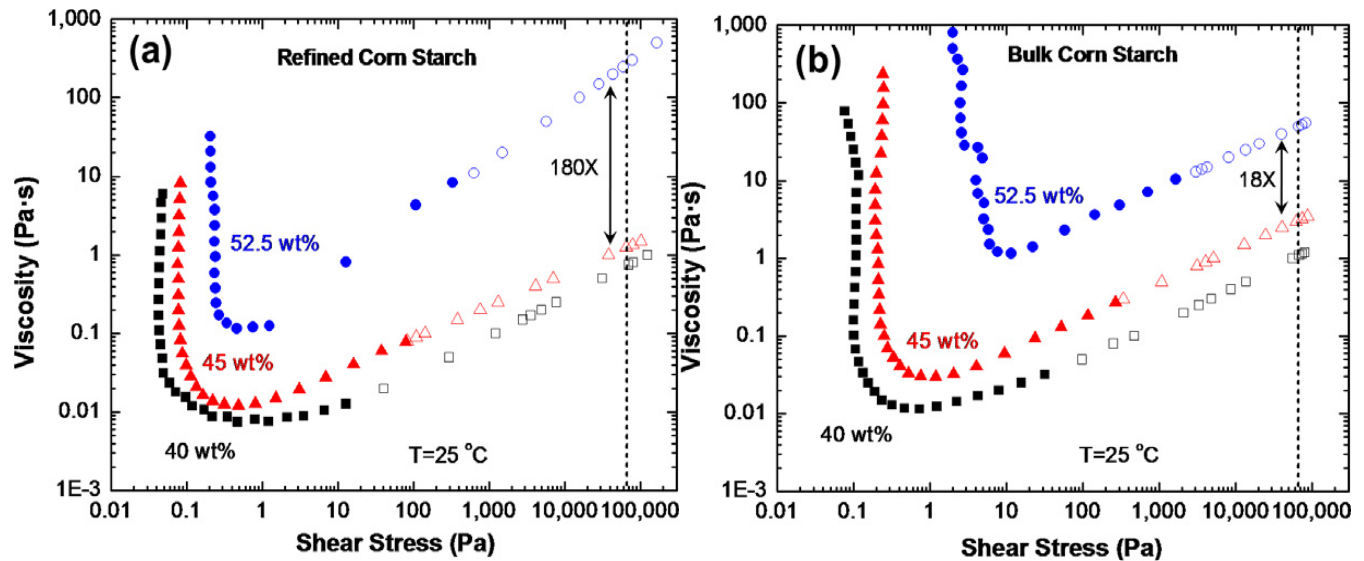
Figure 2.25: Steady State Shear Stress Ramp of (a) Refined and (b) Bulk Cornstarch Suspension at Different Weight Percentages [31].

Two examples may be compared to the above viscosity: ketchup (50Pa·s) and peanut butter (250 Pa·s). Although one could contemplate a person walking across a pool of peanut butter, a pool of ketchup might not be feasible. In fact, the steady state ramp data neglected the effects of any impact and the boundary effect. Therefore, the steady state data is an underestimation of the viscosity in which only the shear thickening effect was considered.

The shear thickening mechanism above has been exploited to improve the surface finish of complex tools. In the shear thickening polishing method, a bath of a non-Newtonian fluid is used to reduce the surface roughness of the cutting tool with a complex shape [38]. As shown in Figure 2.26, the cutting insert is held in a fixture and the polishing tank is rotated. The bath consists of a multi-hydroxyl polymer, dispersant, deionized water and fine diamond abrasive.
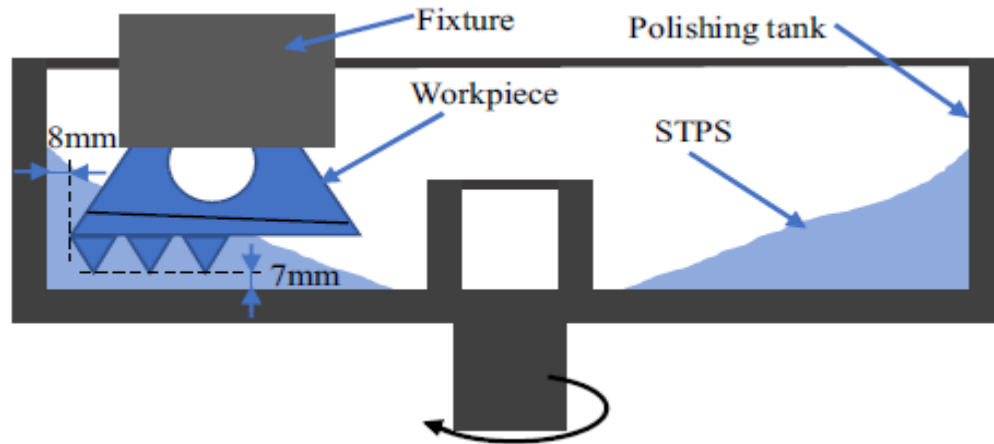
Figure 2.26: Shear Thickening Polishing Method [38].

When the fluid moves relative to the cutting insert, the fluid is sheared. The apparent viscosity of non-Newtonian fluids is increased exponentially with respect to the shear rate, and thereby causing shear thickening. As a result, a particle cluster is formed with the diamond abrasives wrapped around a multi-hydroxyl polymer cluster as shown in Figure 2.27. The abrasives are then forced onto the workpiece causing material removal.
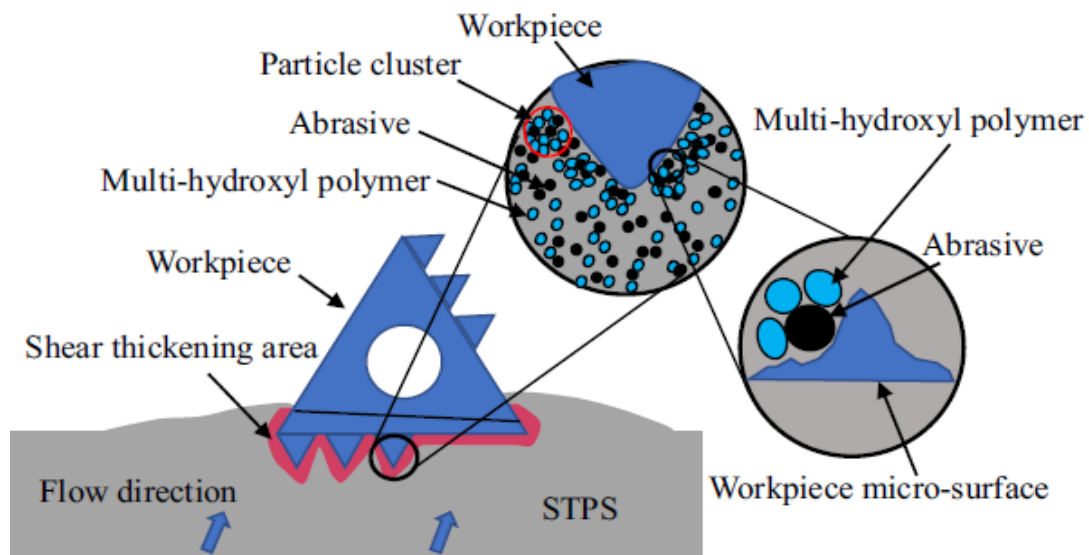
Figure 2.27: Mechanism of the Shear Thickening Polishing Method [38].

The rotational speed is the most important factor that determines polishing performance in this process. The viscosity of the STF is increased by an increase of rotational speed causing more abrasive material removal. In addition, the surface roughness is decreased with an increase in abrasive concentration. However, an excessive percentage of abrasives cause an increase of the surface roughness, due to this causing interference in the shear thickening process.

2.3.4 Dynamic Jamming

As discussed in the previous section, the steady state shear ramp data [Figure 2.24] captures the shear thickening property of the cornstarch suspension. However, experiments have shown that the stress generated can be much higher than that when a transient loading is involved [12]. In fact, not only the cornstarch suspension can be thickened but it can also be solidified or jammed. In this section, the dynamic jamming behaviour is investigated and differentiated from the shear thickening mechanism.

Force transmission in non-Newtonian fluids was investigated by driving an object through the cornstarch bath to near a clay boundary [39] [Figure 2.28 (a)]. On doing this, an imprint was found on the clay and its geometry was studied. It was found that the size and curvature of the imprint is dependent on the speed and size of the moving object as shown in Figure 2.28 (b). The shape and size of the depression resembled the object with an increase in velocity [Figure 2.28 (c)]. Note that in order to deform the clay, a viscosity that is an order of magnitude higher than the maximum measured value in the steady state shear ramp test [Figure 2.24] is required.
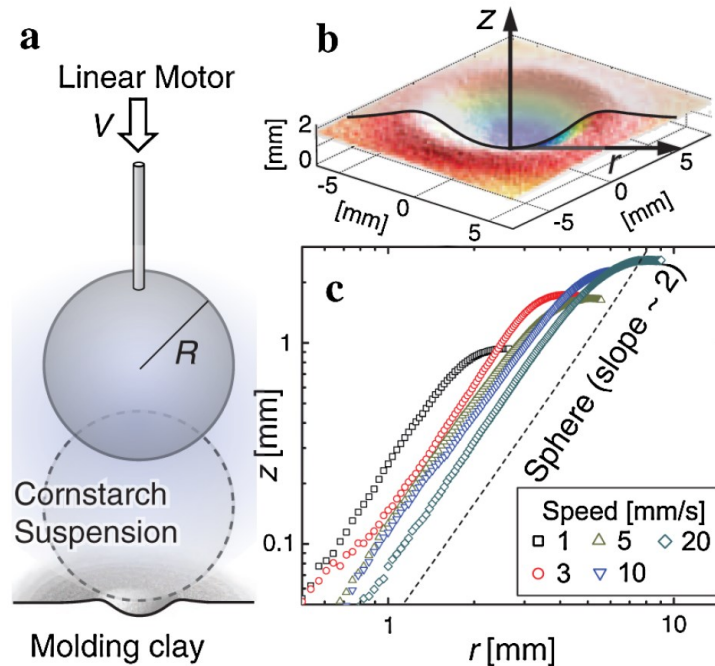
Figure 2.28: (a) Imprint Caused by a Spherical Object Stops Near the Molding Clay (b) Depression Profiles at Elevation Z vs Radius r (c) Digitized Depression Profiles at Various Speed [39].

The moving spherical object was stopped at sequentially reduced heights before hitting the clay, which changed the depression and its curvature of the feature on the clay. Since the object never touched the clay, the dimple of the clay was deformed by a solidified suspension in between that had greater yield stress than the clay. Furthermore, the depression on the clay tended to become more focused but shallower at lower speed. At high speed, the depression on the clay resembles the shape and size of the spherical object. This implied that the higher shear rate could produce a harder jamming region that resembled the size of the spherical object. When a circular cylinder was used instead of a spherical one, the depth of the imprint was deeper than the spherical object and the shape of the indentation on the clay became hemispherical at high velocity [Figure 2.29].
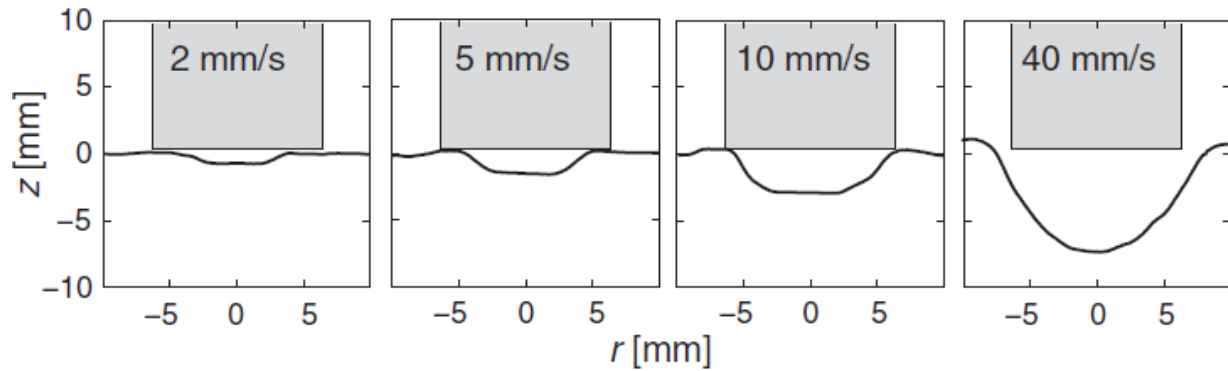
Figure 2.29: A Circular Cylindrical Object Travels at Various Speed and Stopped Near the Clay Surface.

Two interesting observations, bulk oscillation and stop-go-cycles [40] were observed when dropping settling objects such as hollow cylinder, stainless steel and ping pong ball into a container with cornstarch suspension. The trajectory of the settling object was recorded by filming the steel wired attached at the end of the object using a high speed camera as shown in Figure 2.30, as the cornstarch is opaque.
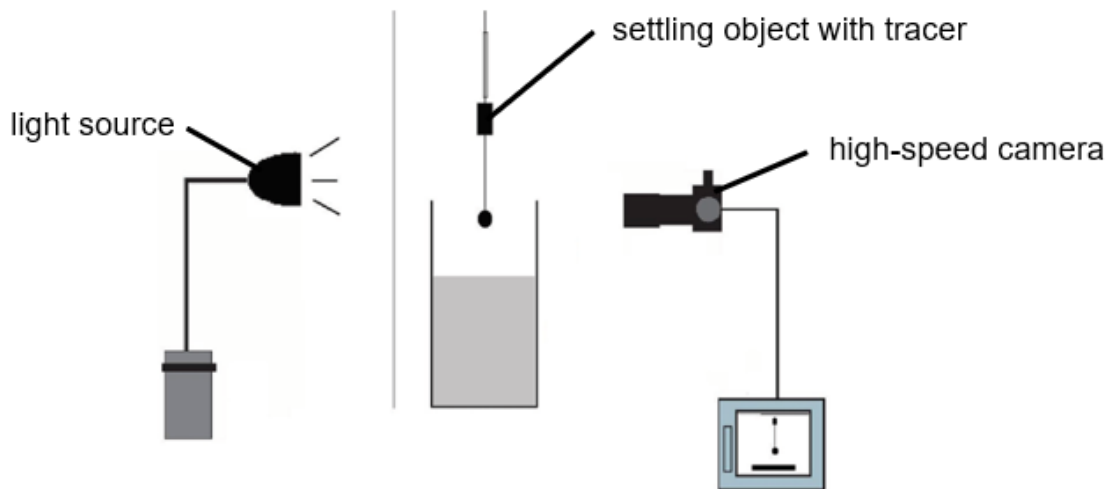
Figure 2.30: Setup for Observing the Bulk Oscillation and Stop-go-cycles [40].

The bulk oscillation referred to the settling object reducing its speed to about its terminal velocity but in an oscillating fashion and the stop-go-cycles referred to the object coming to a full stop when it reached the bottom of the container but bounced up and down until it was completely stopped. The stainless steel ball did not exhibit the bulk oscillation until the volume fraction of the cornstarch bath reached 39%. This might be result from the lack of cornstarch particle to interact with each other to form a hydrocluster network during impact. Intuitively, a more pronounced bulk oscillation and stop-go-cycles were observed with a higher volume fraction of the cornstarch because of the sufficient particles to form a jamming region upon impact.
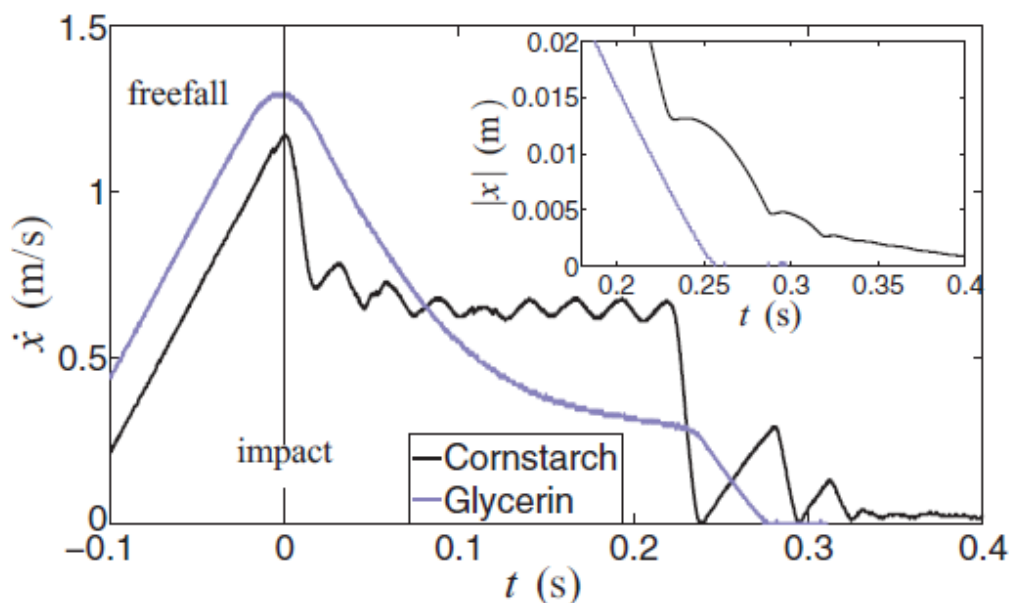
Figure 2.31: Velocity of a Settling Object in Cornstarch and Glycerin Suspensions [40].

In addition, when the object was dropped into the cornstarch bath with a smaller cross-section container (height remains the same), the object was quickly reduced to terminal velocity and then experienced a momentary stop and proceeded with a less pronounced bulk oscillation [Figure 2.32]. The brief zero velocity moment might have

been caused by the jamming domain of the suspension that could not propagate out like the one in a larger container. The jamming domain was "trapped" between the boundaries and the object causing a temporary stop. Similarly, the bulk oscillation was also interfered by the "trapped" jamming domain which caused more friction acting on the object to reduce its velocity.
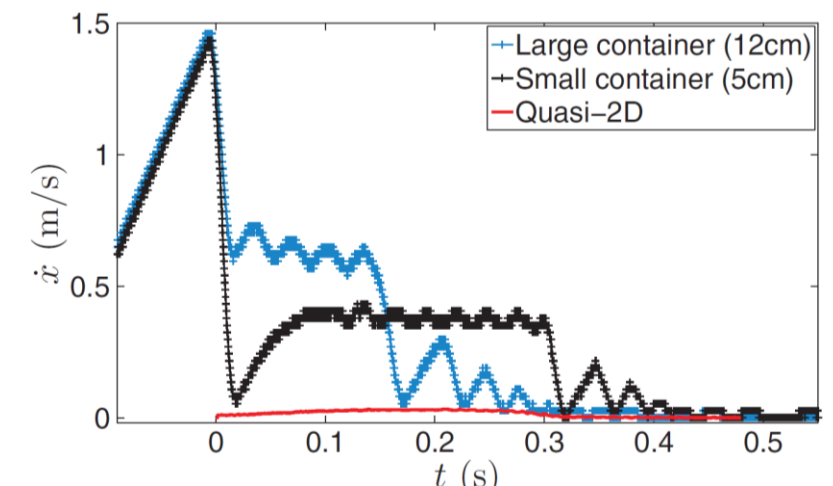
Figure 2.32: Velocity vs time of the Settling Object in Different Sizes of Container [40].

The trajectory of the settling objects was significantly influenced by their mass and shape. The bulk oscillation had an increased amplitude as the mass of the settling object increased but was not observed when the mass was too light. Since the mass of the object related to the sinking velocity and impact, it implied that a certain amount of shear rate or impulse was needed to trigger the dynamic jamming behaviour of the cornstarch suspension. Furthermore, a variable mass cylinder was used and the amplitude of the bulk oscillation was significantly increased while the heavier cylinders show no damping during the bulk oscillation. These findings might be due to the flat bottom of the cylinder

object not letting the jamming region propagate as easy as the sphere one. As a result, the jamming behaviour was more pronounced.

The effect of the boundary was further investigated by varying the suspension depth with an ultrasound setup as shown in Figure 2.33 [12].
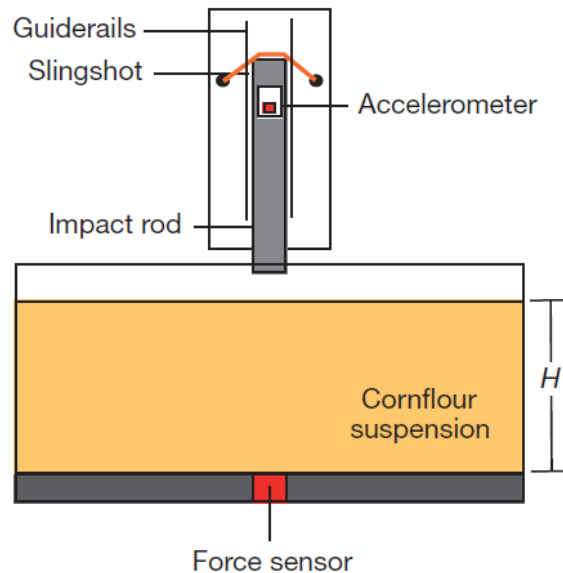
Figure 2.33: Force Measurment when Varying Suspension Depth H [12].

The cornstarch suspension was being impacted and the acceleration of the impactor was monitored and plotted against time. The first a_{rod} peak was noticed for all the depths at t = 10 ms [Figure 2.34]. When the depth of the bath was the highest (H = 20.5 cm), there was only a small visible peak at t = 75 ms. This peak became earlier and more pronounced as the depth of bath decreased. The third peak was also noticed when the depth was lowered to 10.5 cm and less. This might correspond to the stop-go cycles described by [40] as which the solidified suspension stored and released the impact energy. The force response at the bottom of the boundary was also simultaneously recorded at H = 8.5 cm [Figure 2.34]. When the impactor first hit the suspension (where

the first peak was occurred), the force was not felt at the bottom but only when the second peak occurred. This implies that the stress transmitted from the impact to the bottom took time to propagate. However, the second peak from the a_{rod} and the force respond measured from the bottom was simultaneous. This implies that once stress propagates to the boundary and the solidified region has been formed, the force transmission back to the impactor was instantaneous. The solidified region exhibited a true solid-like behaviour where the force transmitted from one end of a solid to the other end is simultaneous.
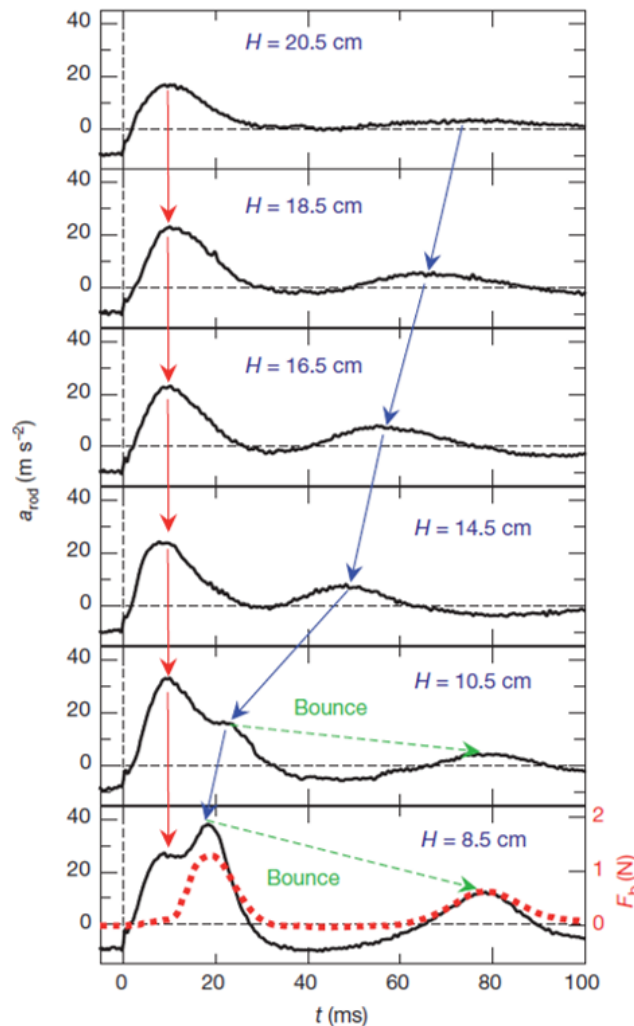
Figure 2.34: Acceleration of the Impacting Rod vs Time for Varying Suspension Depth H [12].

The force response due to the boundary effect was further studied by allowing the impactor to travel at a constant velocity to near the bottom of the boundary. As shown in Figure 2.35, the force was slowly rising as the rod travelled deeper into the suspension due to the buoyant forces. A sudden rising force was recorded as the rod near the bottom of the container. This is attributed to the cornstarch suspension forms a jammed domain which interacted between the rod and the bottom boundary.
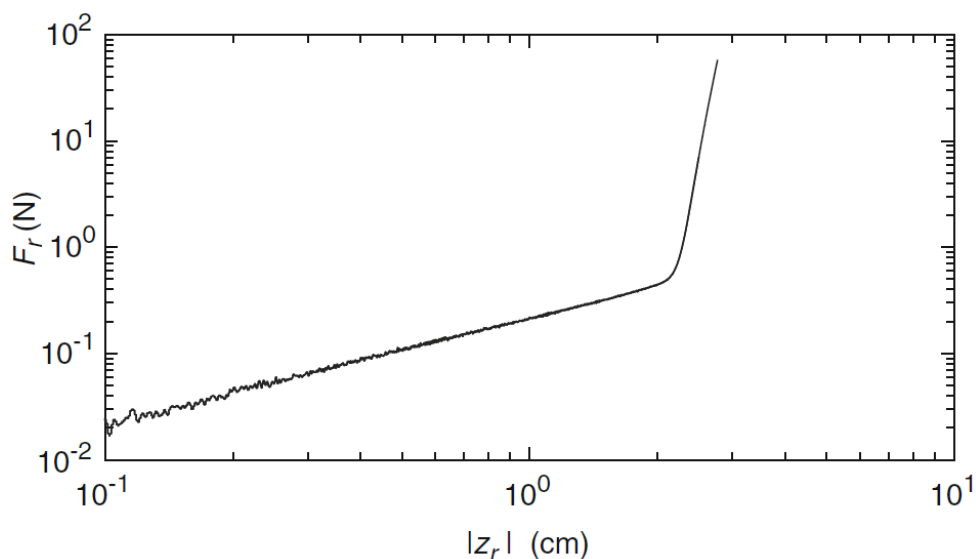
Figure 2.35: Force Response of a Rod Traveled at a Constant Speed into a Cornstarch Bath [41].

The effect of impact on non-Newtonian fluids has been studied in [12]. In this experiment, a large volume of a non-Newtonian suspension was poured into a confined boundary so that the propagation of the jammed region from the impact would not be affected by the boundary. The dynamic behaviour was captured by force response and x-ray imaging [Figure 2.36]. The pressure on the metal rod surface was measured to be 1 MPa and this stress was way above the expected stress exerted by an average adult walking on top the cornstarch (50 kPa) [12]. X-ray imaging indicated that the momentum

of the rod was absorbed by the red-coloured jammed mass, and the direction change of the arrow in the yellow portion indicated that the front was propagating outward.
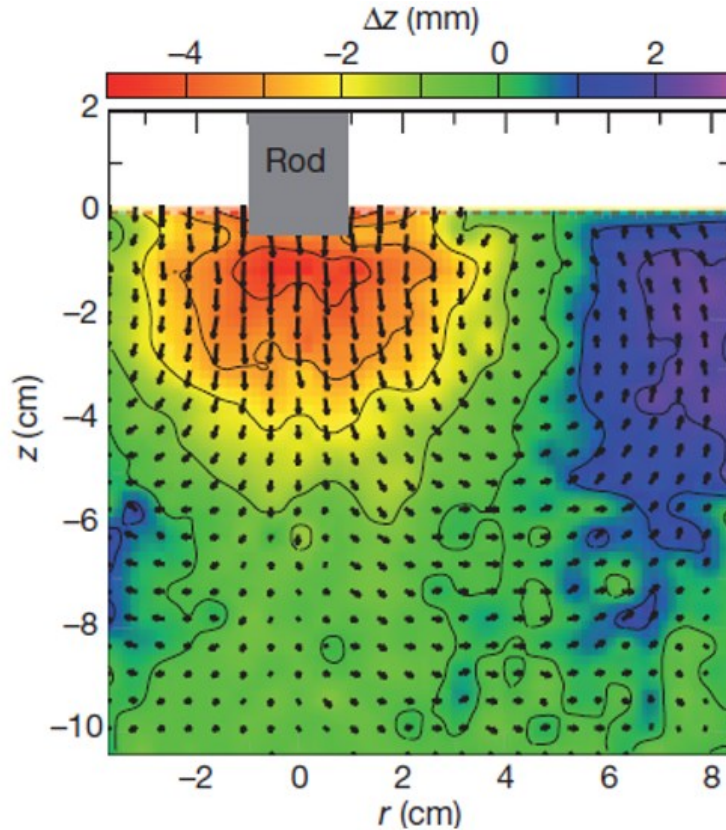
Figure 2.36: Displacement Field of Cornstarch Suspension Being Impacted [12].

A model was proposed to explain the solidification of the dense suspension when being impacted due to densification [12]. When the particles are pushed together, the jammed front propagate at a speed of v_f:

$$v_f = \frac{\emptyset_J}{\emptyset_J - \emptyset_0} v_p \qquad (10)$$

where $\emptyset_J$ and $\emptyset_0$ are the packing fraction of the jammed and initial unjammed state respectively. According to the equation 10, speed of the propagating front is the fastest when the packing fraction near the jammed state. In addition, the sudden impact on the

surface causes the particles to shear thicken at a high shear rate. Hydroclusters were formed due to the local densification and grew rapidly along and outward from the impacting axis. As a result, a solid plug mass was formed underneath the impactor and the fluid adjacent to the solid plug mass was driven along the flow direction [Figure 2.37].
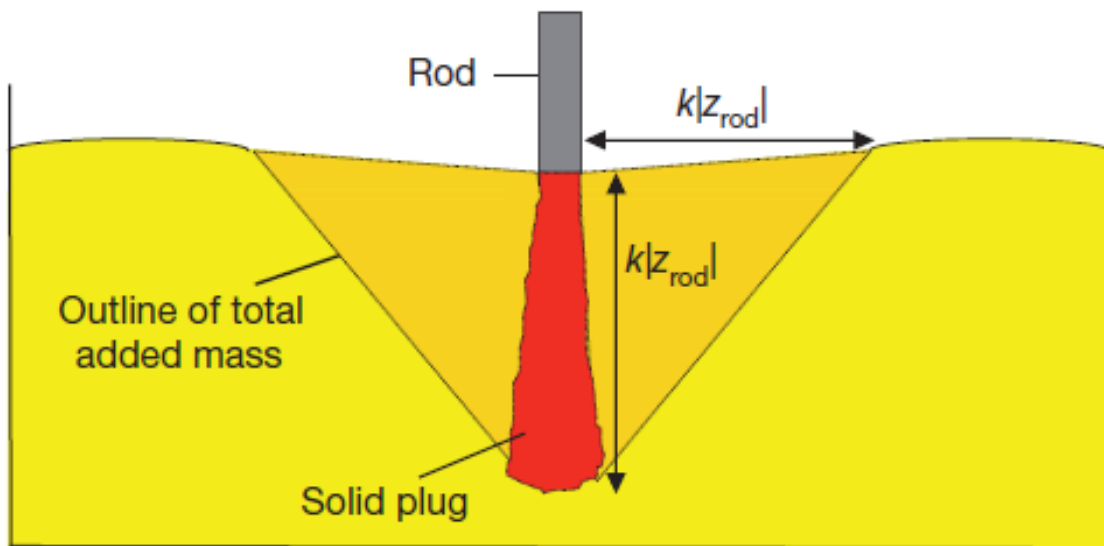
Figure 2.37: Illustration of a Solid Plug Developed on Impact [12].

However, the solidification of non-Newtonian fluids was verified to be due to dynamic shear jamming instead of densification in [42]. During this research, an impactor was traversed through the cornstarch bath at a constant velocity. Due to the opaque nature of the fluid, an ultrasound transducer was used to scan the bath from underneath as shown in Figure 2.38.
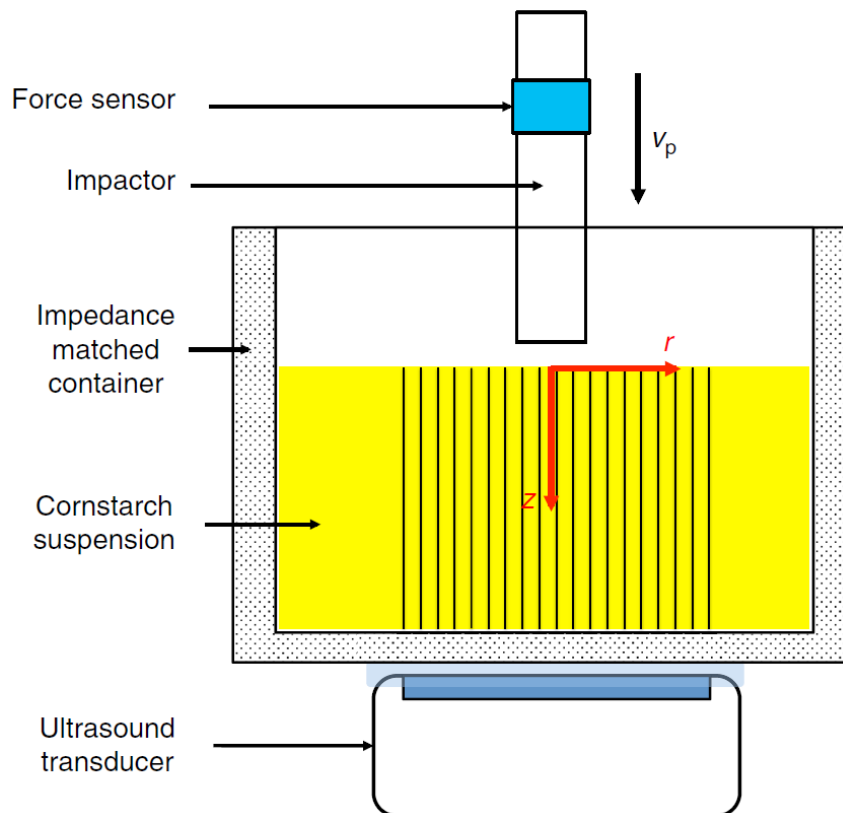
Figure 2.38: Ultrasound Setup to Capture the Flow Field of Cornstarch Being Impacted [42].

The speed of sound was calibrated with different cornstarch packing fraction as shown in Figure 2.39 (a) and compared to the experiment. They observed that when the suspension with a packing fraction of 0.48 was impacted, a solid plug jamming region was formed ahead of the impactor and propagated downward at half of the impactor velocity which agrees with the densification theory. Nevertheless, the change in density of the jamming front was insignificant. By the densification theory, the compression of the particle was needed in ordered to shear thicken the suspension into a jammed state [12]. This implies that the local density of the compression has to be equal of greater than the density of the isotropic jammed suspension. However, Figure 2.39 (b) shows the measured maximum change in sound to be 16 ms^{-1} which corresponds to an increase of

0.02 in packing fraction based on the calibration data in Figure 2.39 (a). The increase of density was insignificant at the jamming region as the maximum increase in density was way lower than that corresponding to the fully jammed state.
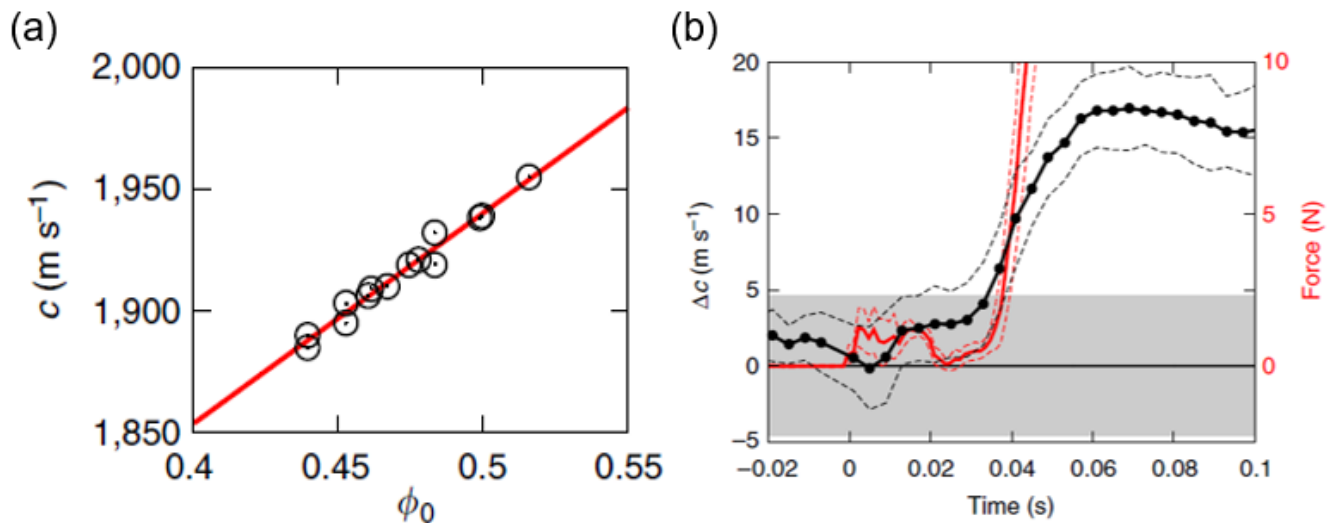
Figure 2.39: (a) Calibration Curve for the Speed of Sound Travelling in Different Packing Fraction of Cornstarch Suspension (b) Change in Speed of Sound when Suspension at a Packing Fraction of 0.48 was Impacted.

Different simulation results have also been compared to verify that jamming can be induced by shear in frictional grain systems that are non-Newtonian suspensions [43]. In the simulation of a frictional grain model, four different states in the system was observed [Figure 2.40]. When the density of the model is below the critical packing fraction ϕ_s, the system is unjammed. When the density is approaching ϕ_s from above, the system is fragilely jammed under small shear where the strong force bearing network could propagate in only one direction. Also, with the increase of shear, the force bearing network might collapse and the system becomes unjammed again. When the density is approaching the jamming packing fraction ϕ_j from below and the minimum required shear

stress is induced, the shear-jammed state is found. At this state, the strong force bearing network can be found propagating in all directions. This further proved that the dynamic shear jammed state could occur at below the isotropic jammed packing fraction.
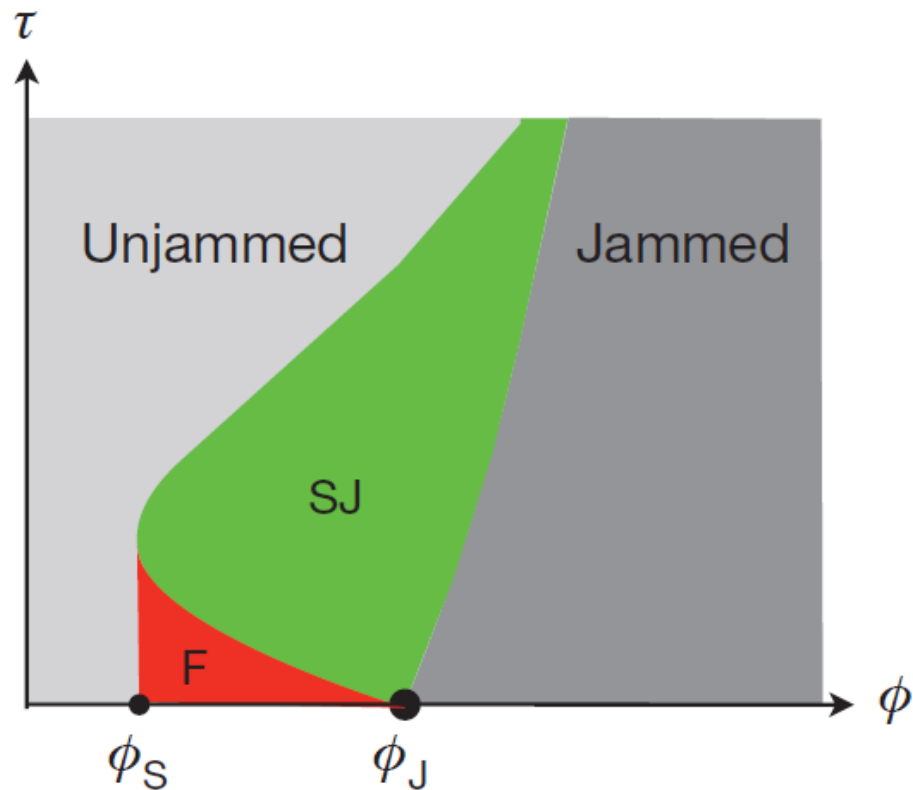
Figure 2.40: Jamming Phase Diagram in Relation with Shear Stress and Particle Density [43].

The effect of the boundary and the impacting angle on dynamic jamming were examined in [44]. In the experiment, a high speed ultrasound imaging system was used to acquire the 3D flow field of the cornstarch bath as shown below.
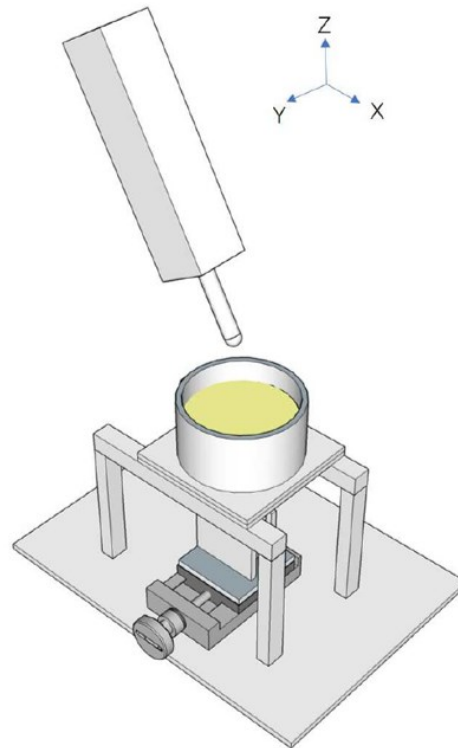
Figure 2.41: Ultrasound Imaging for Tilted Impact [44].

An ultrasound transducer was placed under a cylindrical bath of cornstarch suspension and an impactor was located above it with an adjustable impacting angle and speed. The hemispherical head was used to ensure that the impactor contacted the bath in the same manner regardless of the impacting angle [44].

When the impact was normal to the suspension surface (impact angle = 0˚) as shown on the first column in Figure 2.42, the transient flow ahead of the impactor was fluid-like and propagated with a speed 10 times faster than the impactor whereas the one behind it turned into extremely viscous and almost solid-like state to resist the impact. As the front continued to approach the bottom boundary, the viscous flow behind the front was squeezed due to the interaction with the boundary and its motion was stopped completely. As a result, a sudden jamming was produced between the front and the

bottom boundary. On changing the impacting angle, the jamming front propagated parallel to the impacting angle when it was far away from the boundary. Note that the shape of this front was consistent regardless of the impacting angle as shown in Figure 2.42.
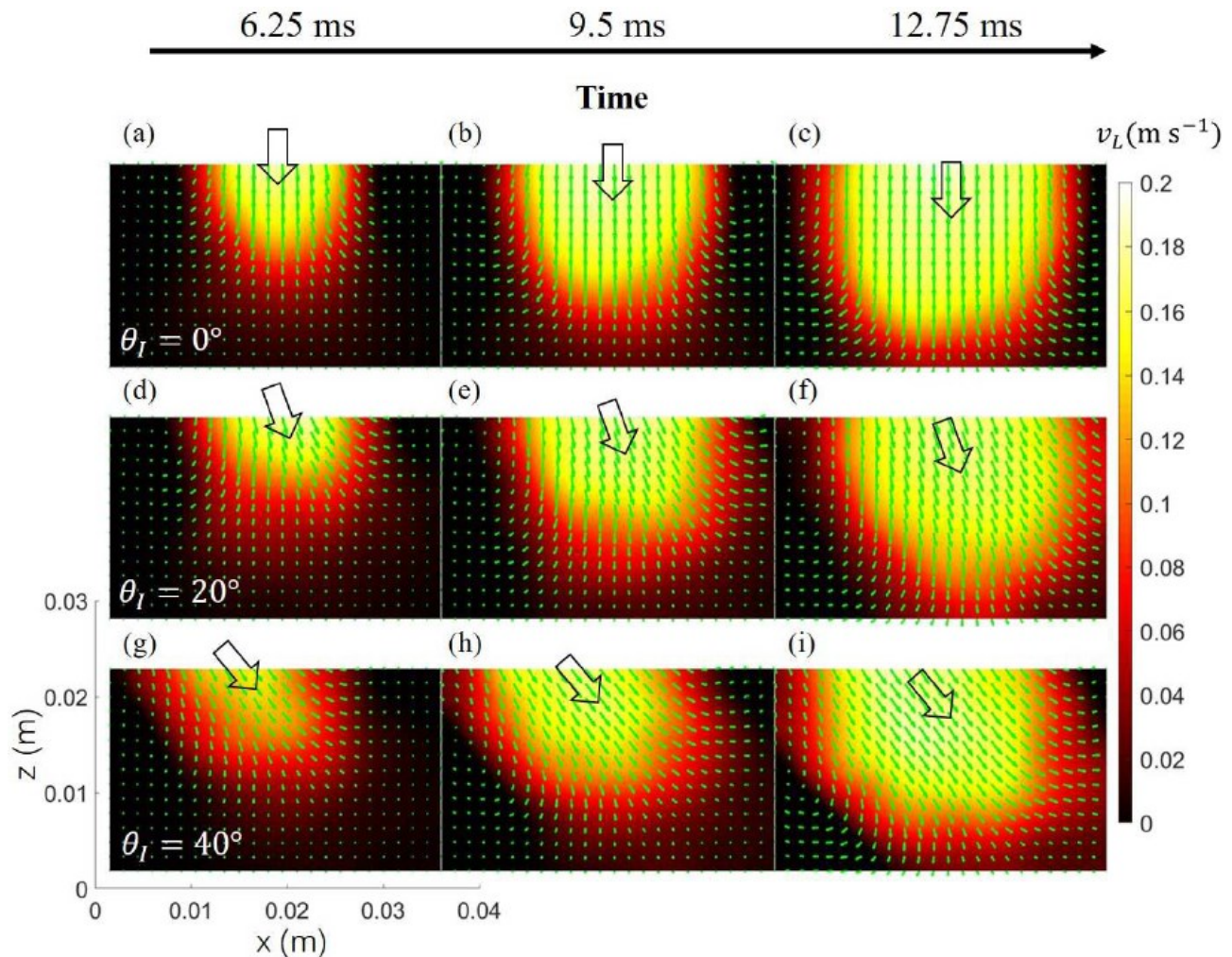
Figure 2.42: Velocity Field of Cornstarch Suspension Being Impacted at Different Angles [44].

As the flow propagated closer to the boundary, the fluid near the bottom gets squeezed by the incoming flow from above forming a squeezed flow as indicated with the blue arrows in Figure 2.43. The moving solid-like flow (the yellow zone in Figure 2.43) is

pushed away by the squeezed zone and the squeezed zone eventually becomes an almost static region. The moving solid-like fluid was then grown outward to the right side. Ultimately, the solid-like jamming front propagated to the side and not because of towards the point P but because of the interaction of the squeeze flow and the rigid boundary.
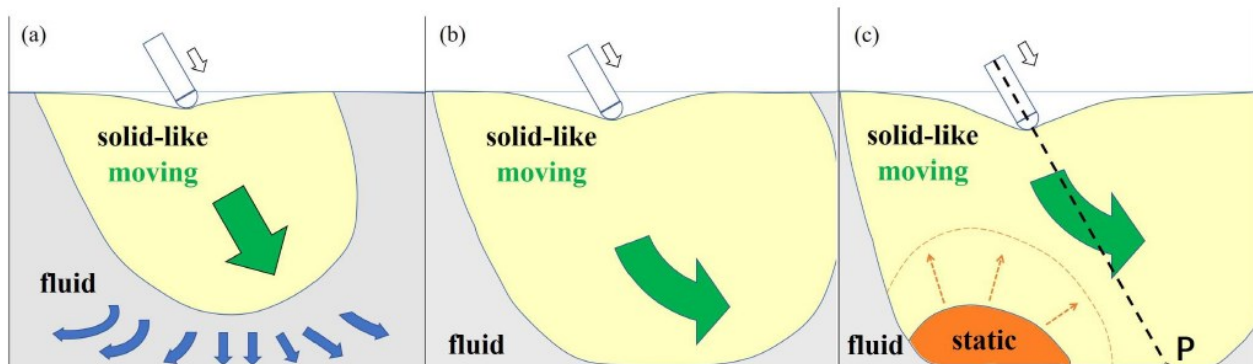
Figure 2.43: Illustration of the Tilted Impact Induced Solidfication Domain Interacting with the Boundary [44].

Cornstarch suspension was pulled using a circular plate connected to the rheometer to study the shear jamming mechanism [Figure 2.44] [45]. The force was measured by the rheometer and velocity field was obtained by placing the ultrasound transducer underneath the container.
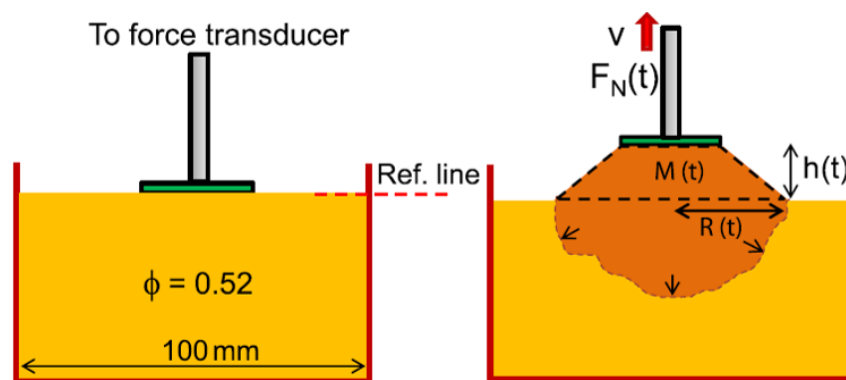
Figure 2.44: Setup for Observing the Behaviour of the Cornstarch Suspension Under Extension [45].

The force required to pull the cornstarch bath sharply increased as the pull velocity increased, and the shape of the suspension being pulled could be modelled as a truncated cone when it was jammed. From ultrasound imaging, as the bath was pulled, the fast-growing velocity field was propagated from the circular plate to the bottom of the container at a rate faster than the extension rate. This jamming front interacted with the boundary creating a squeeze flow that solidify the suspension causing a slow down in the velocity field. This dramatically increased the force needed to pull up the circular plate.

The suspension depth was varied to examine the effect of the boundary. It is found that the force rises sharply at an earlier pulling distance when the depth was reduced. Since the depth was decreased, the distance from the jamming front needs to reach the boundary also reduced. As a result, the jamming front took less time to interact with the rigid boundary which is confirmed by [12] that the jamming front needed time to travel from the originated shear point to the confining boundary.

The dynamic jamming mechanism of non-Newtonian fluids has been investigated and utilized in a surface finishing application in [46]. In this work, coupons were rotated and translated in an aqueous suspension comprising abrasives and cornstarch to reduce the surface roughness. First, the force response was captured to show that the onset of dynamic jamming is due to the combined action of spindle rotation and orbital motions [Figure 2.45 (a)] in close proximity to a solid boundary. This distinguished between the mechanisms of shear thickening and dynamic jamming and indicated the shear rate to be not the only parameter that influences the thickening behaviour and hence the finishing action. This work indicated the finishing action to be brought about by abrasives that are forced against the rotating coupons by the jammed domain ahead of the tool motion

[Figure 2.45 (b)]. This solid-like jammed domain was found to be capable of exerting normal stresses up to 1 MPa [12].
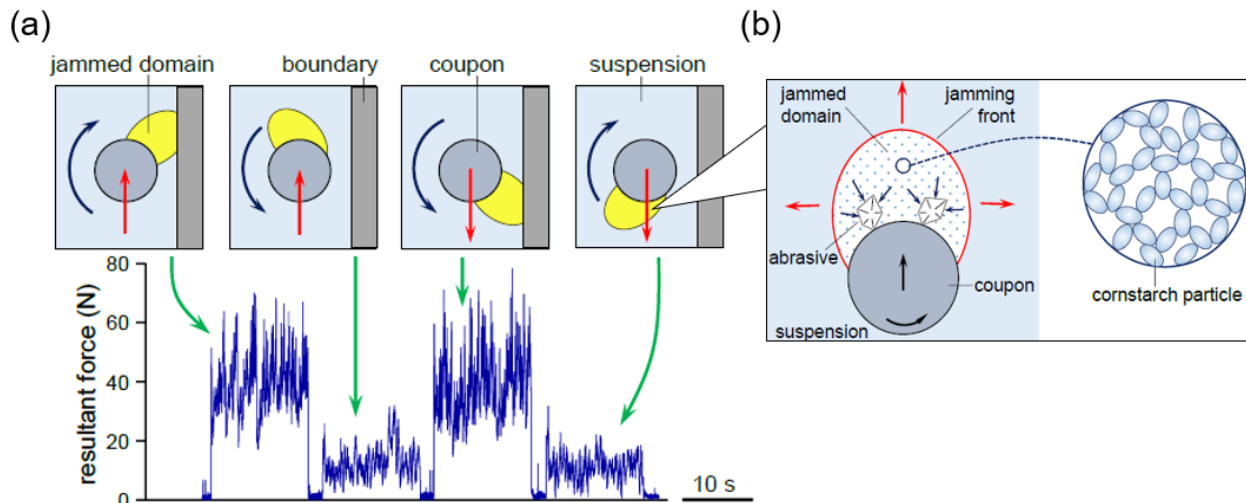
Figure 2.45: (a) Kinematics and (b) Dynamic Jamming as a Mechanism of Material Removal in Surface Finishing [46].

Another important finding was the influence of various finishing paths of the coupon in relation to the solid boundary. Twin boundary orbit, scallop path and linear reciprocating movements were tested to investigate the relative reduction of roughness [Figure 2.46]. It was found that the twin boundary obtained the best reduction of roughness despite the fact that linear reciprocating motion produced the highest force response [Figure 2.47].
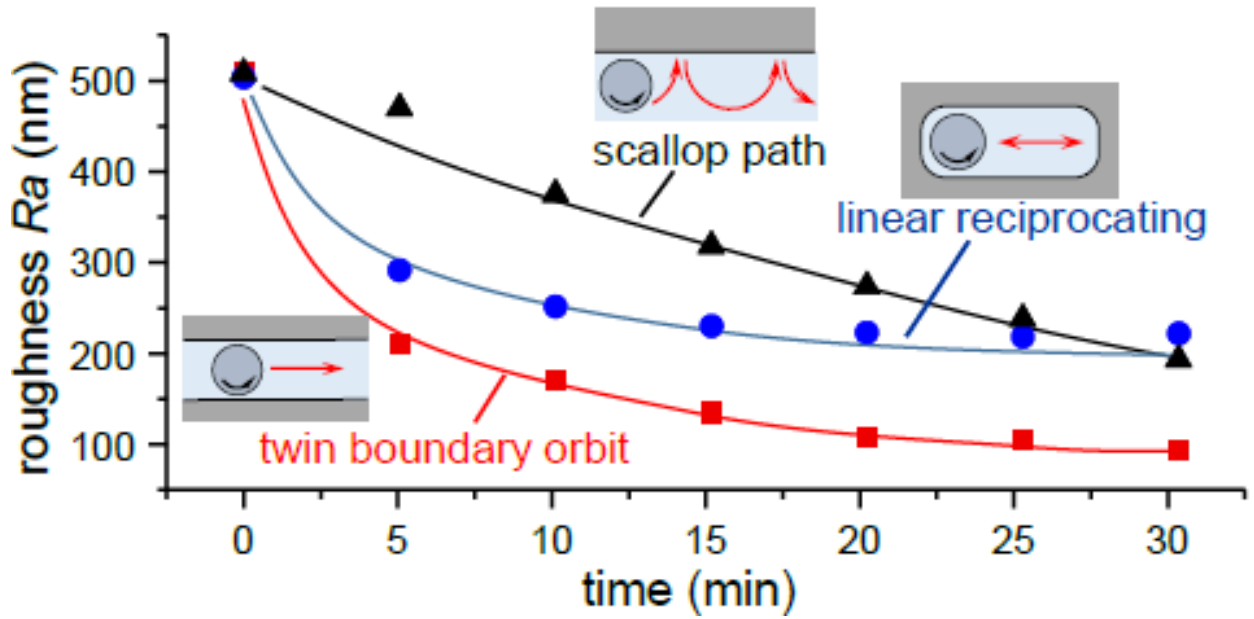
Figure 2.46: Path Dependence on Finishing Performance [46].
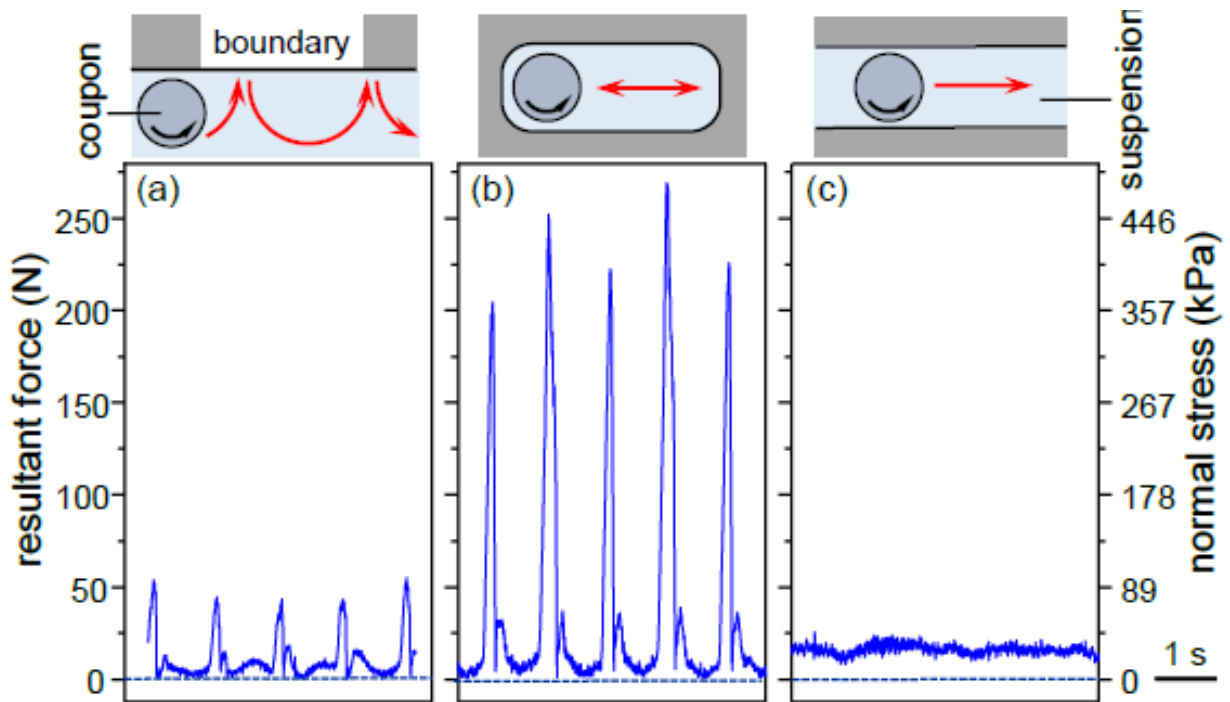
Figure 2.47: Path Dependence on Force Response [46].

2.4   Concluding Remarks

According to studies reviewed in this chapter, an appropriate roundness on the cutting edge can prolong cutting tool life up to 200% and customization of edge asymmetry can influence the dominant wear on the tool [9]. Thus, manufacturers can tailor cutting tools through edge honing techniques to accommodate different cutting conditions for maximum productivity. The reduction of surface roughness on cutting tools by edge honing can enhance film adhesion and consequently improve wear resistance of the coated cutting tools [20]. Therefore, a comprehensive edge honing technique should accommodate varying cutting tool complexities, generate smooth roundness and micro-shape the geometry on the edge radius.

Current edge honing techniques have limitations which prohibit an efficient means to edge hone cutting tools. The most common disadvantages from the discussed techniques is the inability to efficiently hone complex tools with asymmetric and gradient edge. For example, brushing and drag finishing lack the control required to produce an accurate pre-defined edge microgeometry; AJM and AFM conditionally produce asymmetric and gradient edge radius due to their complex abrasive flow and material removal mechanism; Laser machining and EEEH can produce a pre-defined edge geometry but tensile residual stresses is often found on tool edges due to high thermal process load. Accordingly, novel techniques should efficiently hone complex tools, incorporate the ability to conform to the shape of varying tools and provide a localized honing performance on the desired location of a tool.

Using non-Newtonian fluids as a novel finishing media demonstrated the capability to remove fine material due to dynamic jamming mechanism [46]. Various papers have shown that the jamming mechanism is quite localized and can generate normal stresses up to 1 MPa [12]. The localized jammed domain can be activated due to impact or interaction with the rigid boundary. In this context, the properties of non-Newtonian fluids seem to match with the requirements for cutting edge honing. Therefore, this thesis investigates an efficient method to produce high quality, customizable cutting edges on complex cutting tools using non-Newtonian abrasive slurry.

Chapter 3

Experimental

The objective of the experimental work in this thesis was to explore the feasibility and identify the mechanisms underlying edge honing of cutting tools using the non-Newtonian behaviour of aqueous suspensions of cornstarch in which abrasives were mixed. In particular, the ability of this process to generate symmetric and asymmetric edges, hone edges of tools with a complex macrogeometry, and fabricate edges with a gradient microgeometry along the length of the edge were investigated. The work considered the effects of such process parameters as spindle speed, rotational direction, orbital speed, suspension composition and boundary configurations. This chapter details the experimental apparatus and procedures, and the measurement equipment.

3.1   Experimental Apparatus

All experiments were performed in the Machining Systems Laboratory (MSL) at McMaster University.

An experimental apparatus was manufactured as shown in Figure 3.1. It consists of a rotary boundary and a spindle. The rotary boundary is driven by a 2 horsepower motor and can rotate to a maximum speed of 60 rpm. The spindle is driven by a 0.45 horsepower motor and can reach a maximum speed of 5310 rpm. Both rotary boundary and spindle can rotate in clockwise and counter-clockwise directions. The spindle can be loaded with different cutting tools and has 3 degrees of freedom so that its position is adjustable relative to the rotary boundary. This setup was fixed to a rigid T-slot table.
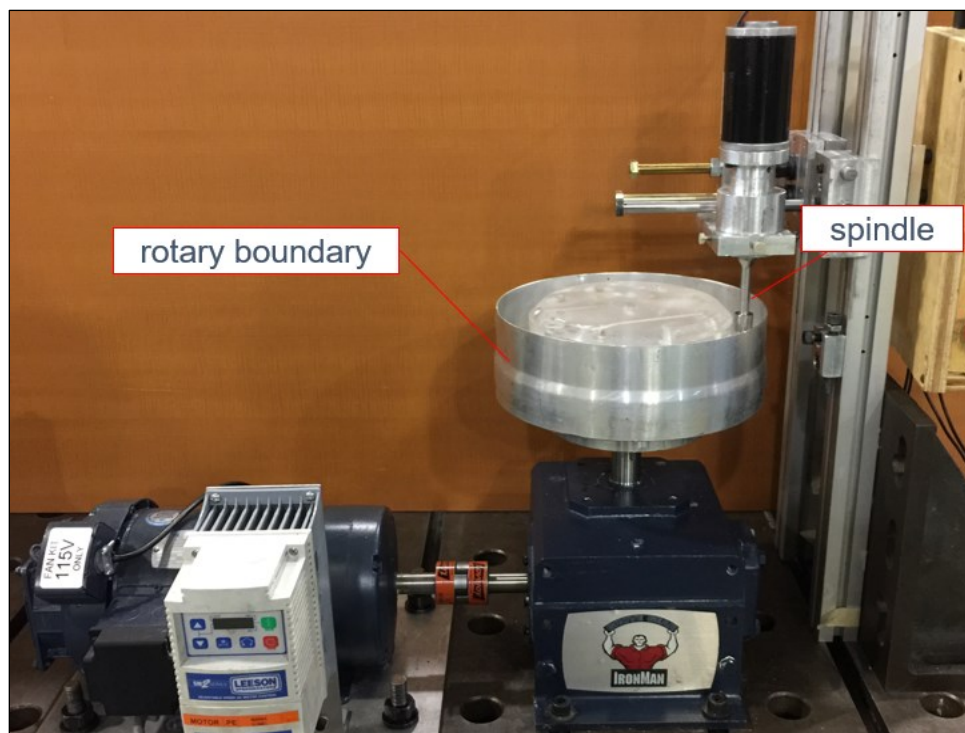
Figure 3.1: Experimental Apparatus.

3.1.1   Rotary Bowl

The rotary bowl consists of outer and inner boundaries in between which the slurry comprising the cornstarch mixture and abrasives was filled to hone the cutting tools with different kinematics [Figure 3.2]. The outer boundary has an internal diameter of 269 mm and a height of 75 mm; whereas the inner boundary is interchangeable to different sizes and geometries depending on the experimental objective. Unless otherwise mentioned, the inner boundary with a diameter of 205 mm was used. The outer boundary is made of aluminum; the inner boundary was made of materials such as aluminum, acrylic or machinable wax again depending on the experiment.
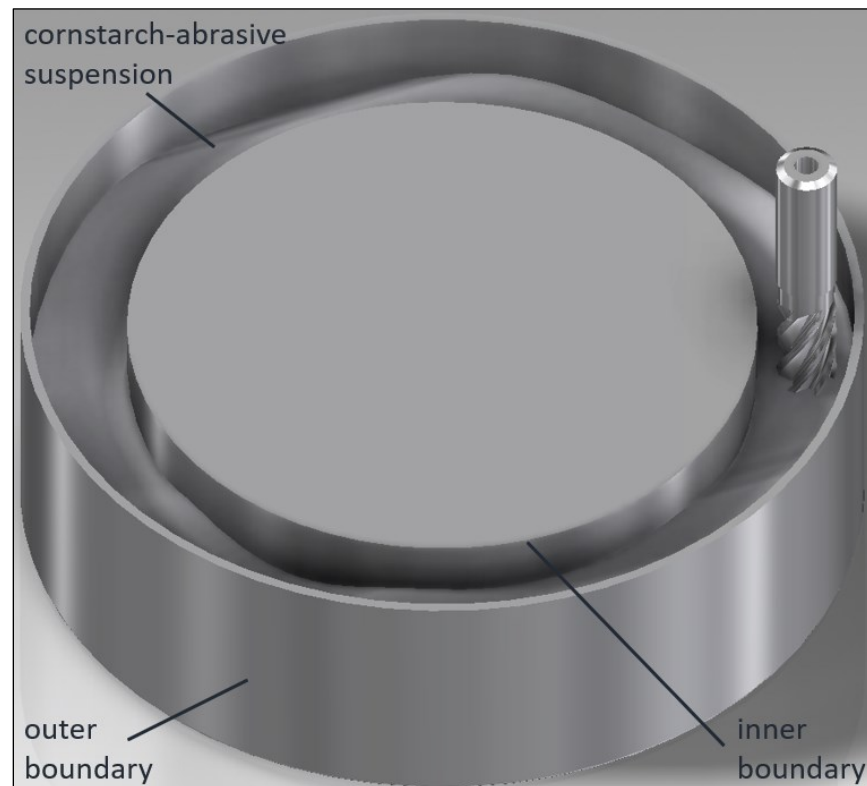
Figure 3.2: Cutting Edge Honing Setup.

3.1.2 Cutting Tool Inserts

Various cutting tool inserts were used to characterize the capabilities of the novel honing process. For example, square and ball-nose inserts were used. Their dimensions are detailed in Figure 3.3. All Inserts used in the experiments were uncoated. The inserts were inspected to ensure that they were sharp, with an edge radius less than 10 μm.
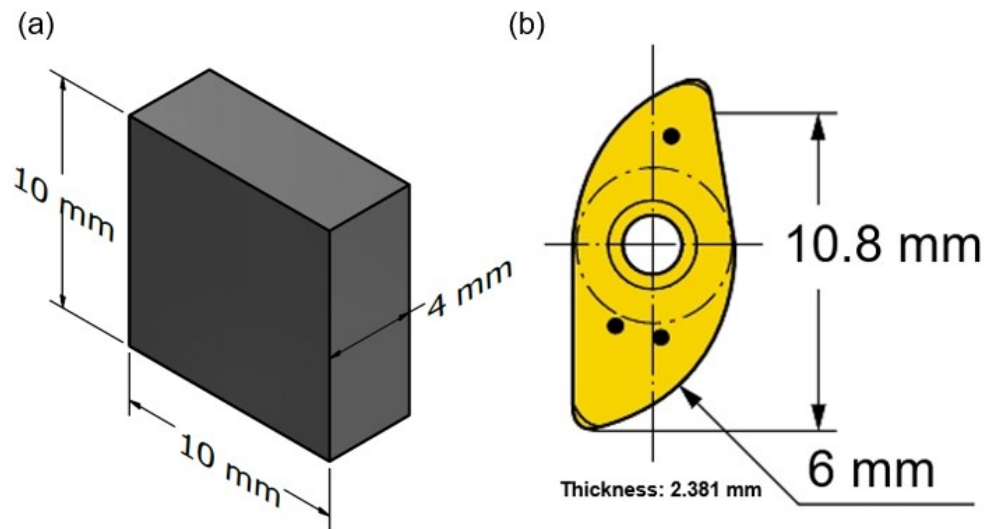
Figure 3.3: (a) Square Insert, (b) Ball-nose Insert.

3.1.3 Tool Holders

Tool holders were manufactured from AISI 1045 carbon steel to hold square and nose-radius inserts. The holders were designed to minimize deformation during the honing process as cornstarch suspension has been reported to be capable of generating normal stresses of up to 1 MPa [12]. The basic geometry of tool holders is as shown in Figure 3.4 (a). They have a diameter of 19.05 mm and the middle was turned down to a diameter of 10 mm to reduce slurry spillage during experiments. A slot was machined at the bottom to hold the insert in place by friction [Figure 3.4 (b & c)]. In addition, the insert is offset

from the bottom of the tool holder by 3.18 mm by using a parallel so the bottom edges

could be exposed to the flow during experiments.
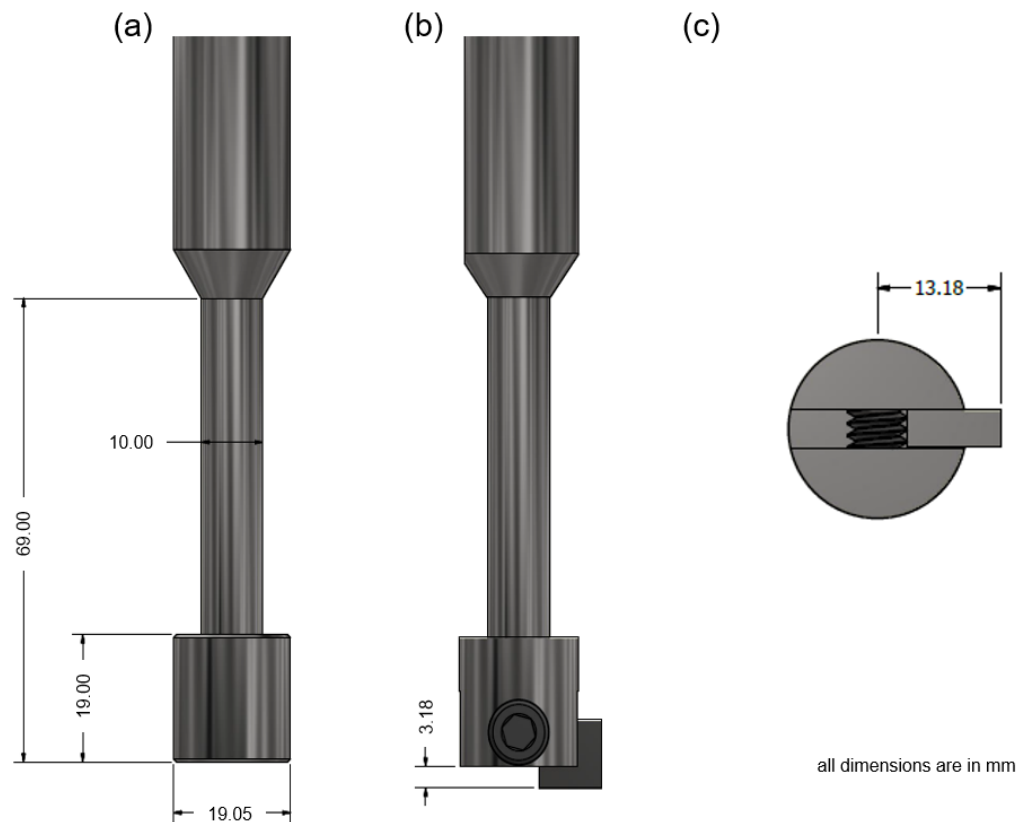
Figure 3.4: (a) Basic Geometry of Tool Holder (b) Front View and (c) Bottom View of Tool Holder Clamping a Square Insert.

Ball-nose inserts came with a customized tool holder from Sandvik Coromant which allows for simultaneous installation of two inserts. Due to the interference of the original design of the tool shank with the rotary boundary, the shank was turned down to a radius of 6.8 mm [Figure 3.5].
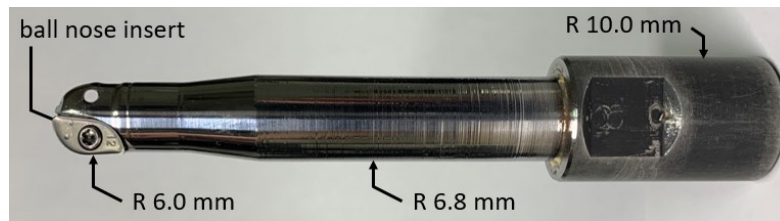
Figure 3.5: Ball-nose Insert Fixed on the Tool Holder.

3.2   Cutting Edge Measurement

After each experiment, cutting inserts were rinsed with water to clear the cornstarch and abrasive mixture prior to measurement. Inserts were then cleaned in an ultrasonic cleaner with acetone for 50 seconds and dried with a lint-free wipe. Cutting edges were measured before and after the experiment using Alicona Infinite Focus white light optical system [Figure 3.6]. This system can measure 3D objects by combining images taken at different heights and present them as one 3D data set [47].
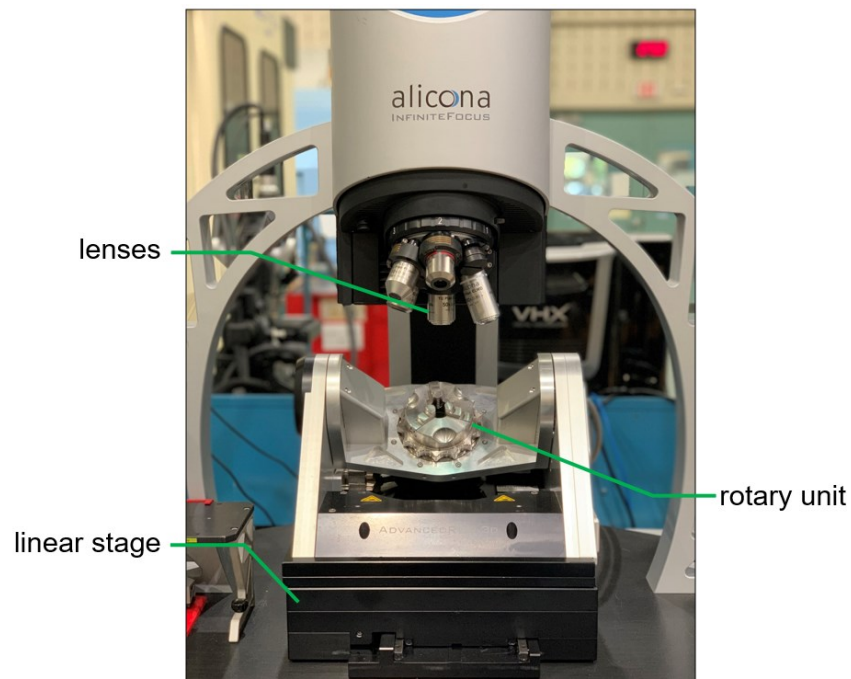
Figure 3.6: Alicona Infinite Focus White Light Optical System.

With the aid of the white light optical system, cutting edge radius, asymmetry and roughness can be measured accurately. 20X magnification was used to measure edge radius and asymmetry; 50X magnification was used to measure the surface finish of the edges. These magnifications were chosen for measurement efficiency as high magnification scanning is extremely time consuming. Measurement limits and accuracies of the optical system are presented in Table 3.1 and Table 3.2.

Magnification	2.5x	5x	10x	20x	50x	100x
Min. measurable roughness (µm)	7	1.2	0.3	0.15	0.06	0.03
Min. measurable area roughness (µm)	3.5	0.6	0.15	0.075	0.03	0.015
Min. measurable radius (µm)	20	10	5	3	2	1

Table 3.1: Measurement Limit of Alicona Infinite Focus White Light Optical System [47].

Objective	Accuracy
Profile roughness	$\sigma = 0.002$ µm
	$\sigma = 0.002$ µm
Edge radius	5 - 20 µm: $\sigma = 0.15$ µm
	> 20 µm: $\sigma = 0.3$ µm

Table 3.2: Accuracy of Measuring Objectives [47].

Different inspection tool holders were designed and 3D printed to aid inspection. During measurement, the inspection tool holder was placed on a stage that can be attached to the optical system [Figure 3.7]. The inspection tool holder gripped the insert at an angle of 45 degrees so that the rake and flank faces of the insert were exposed to sufficient white light during measurement.
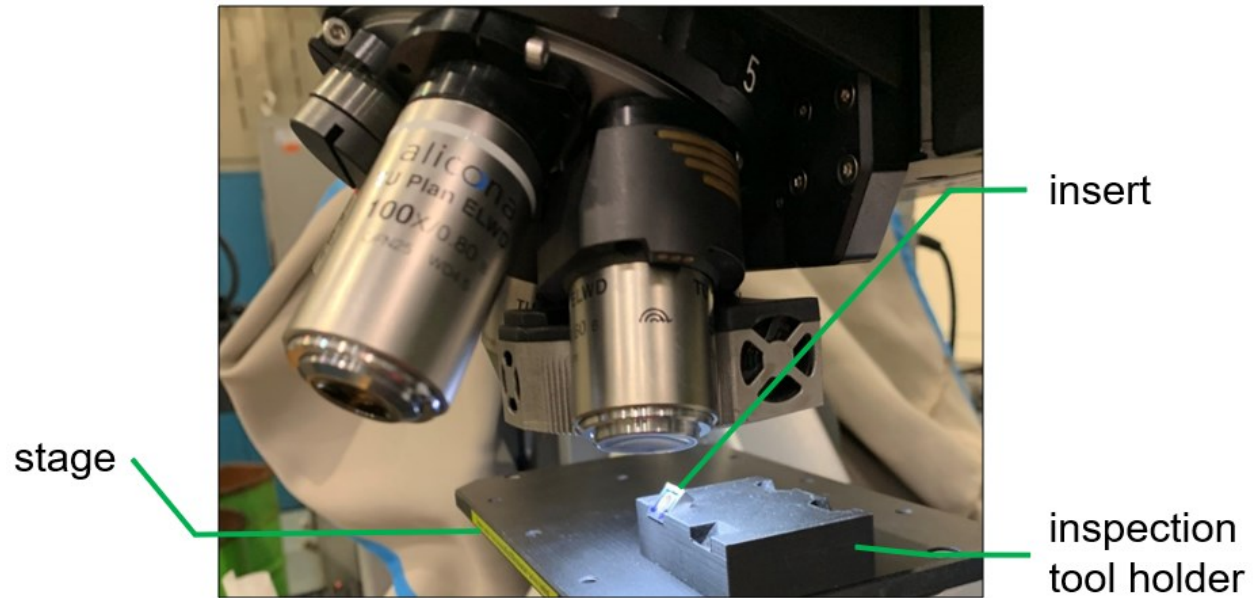
Figure 3.7: Measurement Setup for Square Insert.

In the case of inspecting solid tools, the rotary unit from the white light optical system was used to adjust the measurement position. For example, when measuring edges on the bottom of the tool, it was tilted to 45 degrees [Figure 3.8 (a)]; when measuring peripheral edges, the solid tool was tilted to 0 degrees [Figure 3.8(b)]. The height of the lens was adjusted until the edge was focused on the screen. Then, the rotary unit was rotated until the edge was parallel horizontally or vertically to the guideline on the screen to establish the initial measurement coordinates [Figure 3.9].
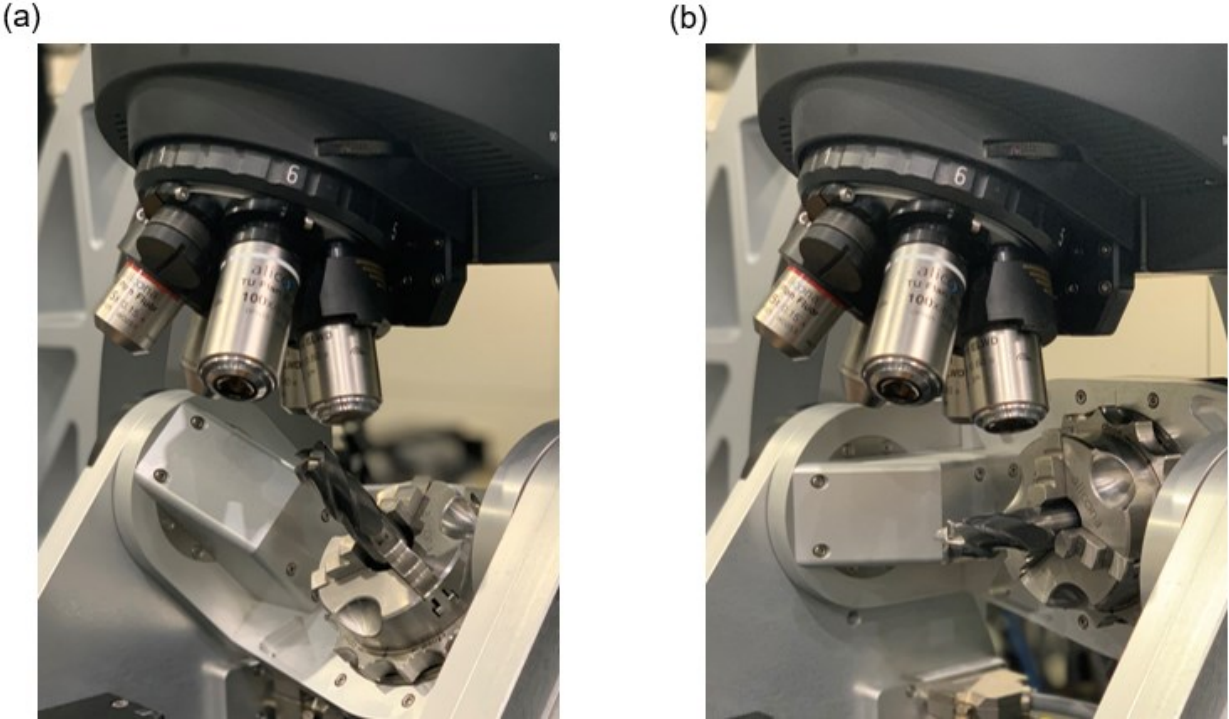
Figure 3.8: Measuring Setup for (a) Bottom Edges (b) Peripheral Edges of a Solid Tool.
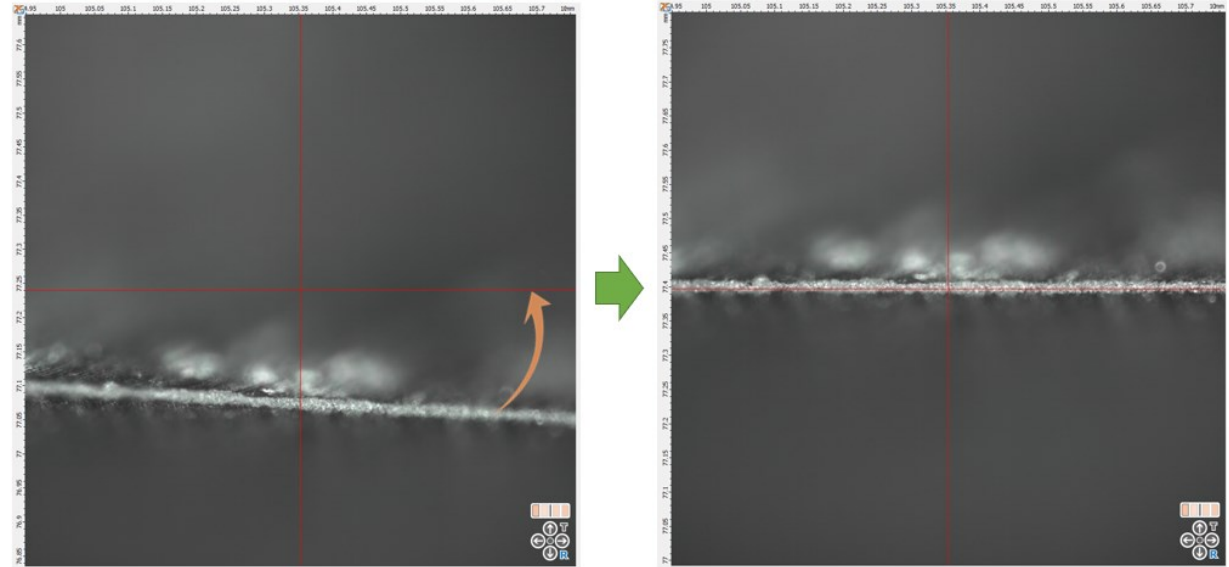
Figure 3.9: Using Guidelines to Align Edge with the Optical System.

When measuring cutting edge radius, 40 profiles were simultaneously measured near the selected location as shown in Figure 3.10 (a). These profiles were processed into one average profile [Figure 3.10 (b)] and the error of the measurement could be obtained by calculating the standard deviation of these 40 profiles.
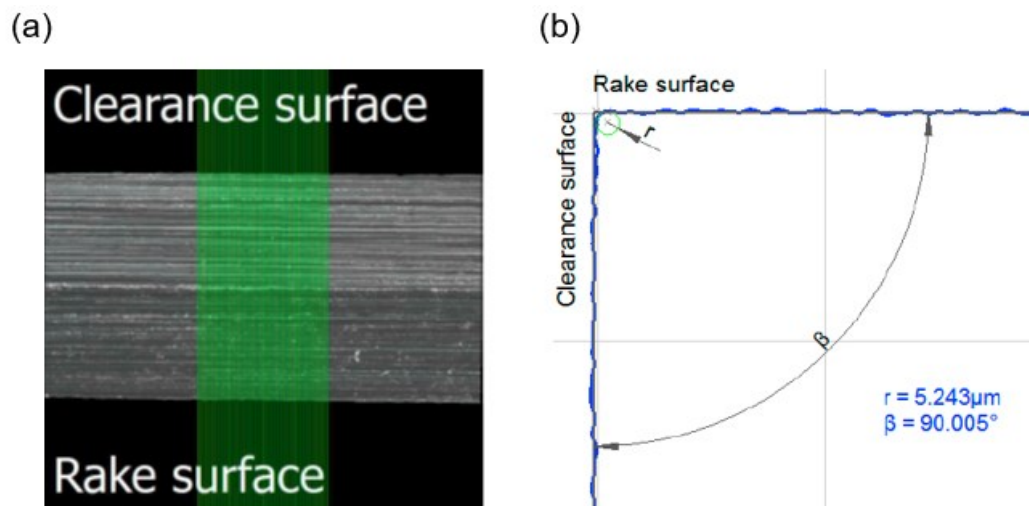
Figure 3.10: (a) Green Lines Indicate 40 Profiles Being Measured (b) Averaged Profile.

3.2.1 Measurement Scheme

Due to the different geometries of the cutting tools, measurement schemes were developed to accurately depict the edge honing performance along the tool edge. Examples of measurement schemes for square, nose-radius and ball-nose inserts are shown in Figure 3.11 - Figure 3.12. For a square insert, 6 points were taken along the edge to ensure that the variability from the honing process is captured.

a = 0.2 mm
b = 1.6 mm

10 mm
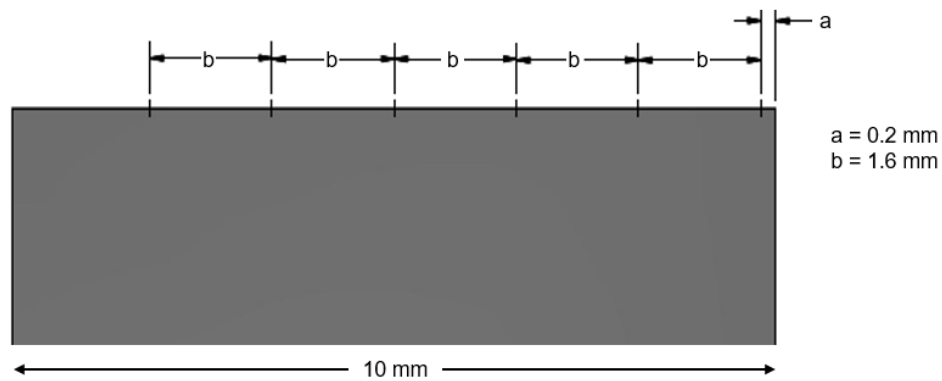
Figure 3.11: Measurement Scheme for Square Insert.

For ball-nose inserts, the measurement schemes were somewhat more involved. Measurements were taken close to the nose-radius due to the interest of honing in this region. As shown in Figure 3.12, a ball-nose insert is measured by dividing the radius into seven sections spanning 17 degrees each. The symbol ⊕ denotes the reference coordinate, relative to which all measurements were accomplished. A list of the measurement coordinates is also shown in Figure 3.12.

Point	X (mm)	Y (mm)
1	0.26	0.02
2	1.90	0.41
3	3.36	1.30
4	4.50	2.52
5	5.22	4.02
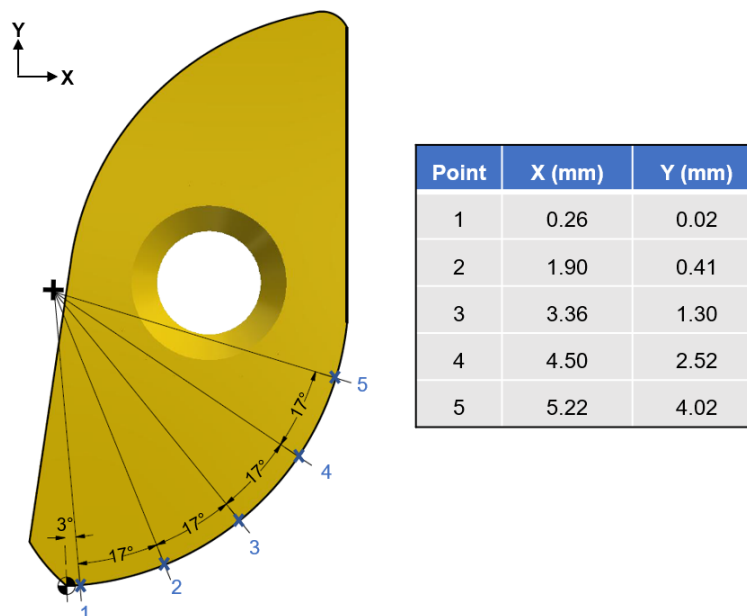
Figure 3.12: Measurement Scheme for Ball-nose Inserts.

3.3   Cornstarch-Abrasive Suspensions

Chefmate Cornstarch was used in the experiments. The rheological response of cornstarch is affected by its moisture content [48], and so cornstarch was purchased in bulk and stored in a humidity-temperature controlled environment.

Brown Aluminum oxide (Al_2O_3) was used throughout this work. Table 3.3 shows the grits sizes that were used during experiments and Table 3.4 shows the material properties and chemical composition of the abrasives.

Grit Size	Min diameter (µm)	Max diameter (µm)
100	106.0	150.0
220	45.0	75.0
320	24.7	30.7
400	16.3	18.3
1200	2.5	3.5
Determination by sedimentation according to German Industry Standard DIN 69 101		

Table 3.3: Abrasive Particle Size.

	Brown Aluminum
Colour	Dark Brown
Hardness (Moh)	9
Bulk Density (kg/m³)	2400
Particle S.G	3.92
Al_2O_3	95.00%
Fe_2O_3	1.00%
TiO_2	3.00%
SiO2	0.72%
CaO	0.30%

Table 3.4: Material Properties and Chemical Composition of Abrasives.

Volume and mass fraction are generally used to specify the amount of cornstarch in a suspension. The mass fraction was chosen in this work as the volume fraction is dependent on how densely the powder is packed. A digital scale with a resolution of 0.1 g was used for weight measurements.

Abrasives were added to the cornstarch-water suspension. The mass fractions were calculated as:

$$CS\% = \frac{m_{CS}}{m_{CS}+m_W} \times 100\% \tag{3.1}$$

$$A\% = \frac{m_A}{m_{CS}+m_W} \times 100\% \tag{3.2}$$

CS% = Percentage of cornstarch

A% = Percentage of abrasive

m_{CS} = Cornstarch mass

m_W = Water mass

m_A = Abrasive mass

Prior to the honing experiments, water, cornstarch and abrasives were mixed in a hexagonal tumbler [Figure 3.13] with a maximum mixing capacity of 3.5 L (or 8 kg) and can tumble at a maximum rotational speed of 100 rpm. The tumbling direction could be changed at intervals to ensure proper mixing. At high tumbling speeds, partially mixed cornstarch suspension could shear thicken and inhibit proper mixing. A low tumbling speed of 30 rpm was therefore chosen to mix the suspension for at least 30 minutes with the tumbling direction changed every minute.

85

Figure 3.13: Hexagonal Tumbler.

Chapter 4

Results and Discussion

4.1   Preliminary Edge Honing Experiments

Preliminary experiments were performed to investigate the feasibility of using aqueous cornstarch and abrasive slurry to edge hone cutting tools as well as set apart the shear thickening and dynamic jamming mechanisms of such slurry. During the preliminary experiments, the following parameters were used unless otherwise mentioned: 50% by weight cornstarch was mixed with water; 15% of 17 μm and 2.5% of 68 μm Al_2O_3 was added on top of the total mass of the suspension. Once the slurry was properly mixed, it was poured into the single boundary container to a height of 40 mm.

Process kinematics were varied to examine the required conditions for edge honing with cornstarch and abrasive slurry. The first one involved an orbital motion with

no spindle rotation [Figure 4.1 (a)]. The second one involved spindle rotation with no orbital motion [Figure 4.1 (b)], and the third one both orbital and spindle motions [Figure 4.1 (c)]. These three configurations are detailed in the following.
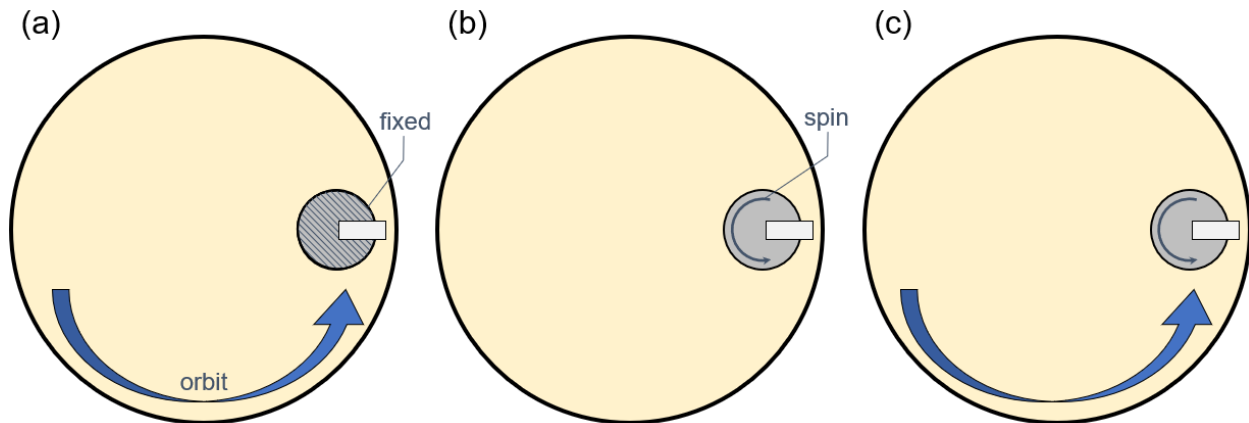
Figure 4.1: (a) Orbital motion, (b) Rotational Motion, (c) Combined Motions.

As shown in Figure 4.1 (a), honing experiments were first performed at different linear speeds of 2, 5, 10, 20 and 40 m/min. The tool spindle was also fixed at three different orientations as shown in Figure 4.2. For orientation at 0˚, the flank face of the insert has a gap width of 2 mm to the outer boundary. Each experiment lasted 5 minutes and the cutting insert was cleaned immediately prior to measurement as detailed in Section 3.2. Average r_β was measured on two exposed edges following the measurement scheme detailed previously in Figure 3.11.
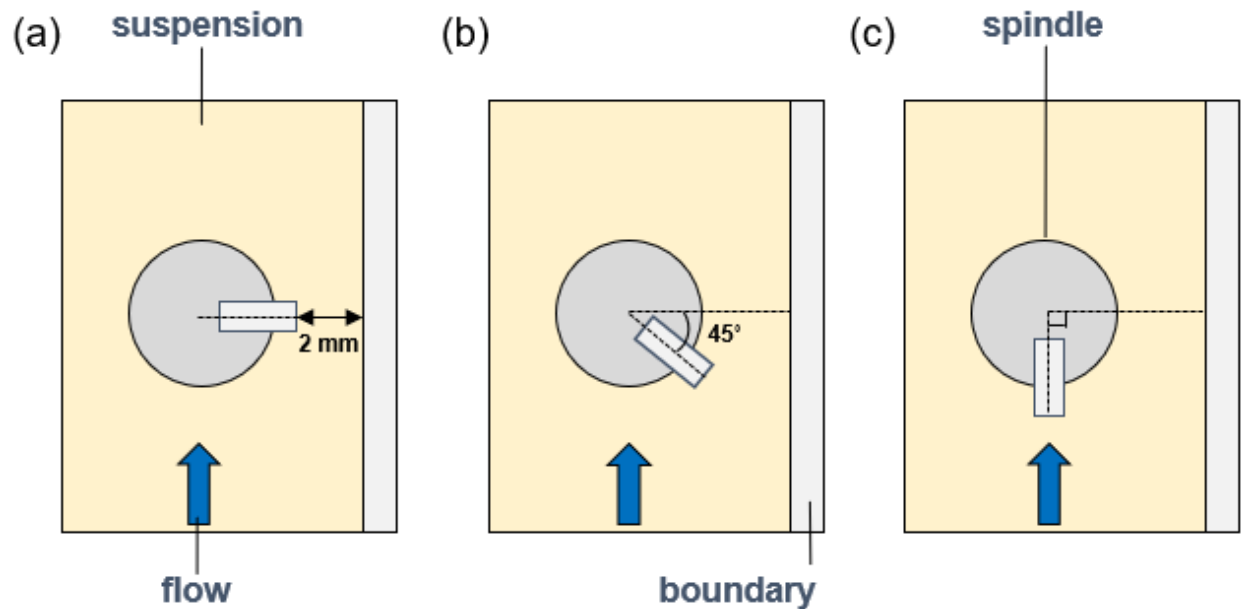
Figure 4.2: Three Tool Holder Orientations: (a) 0˚, (b) 45˚, (c) 90˚.

For the 0˚ orientation shown in Figure 4.2 (a), the shear rates corresponding to the tested linear speeds on the edges were 17, 42, 83, 167 and 333 s^{-1}. For orientation at 45˚ and 90˚ as shown in Figure 4.2 (b) (c), the shear rates were lower due to the increased gap from the rigid boundary. These shear rates spanned across the regime where cornstarch slurry shear thickens as shown in Figure 2.24. However, cutting edge honing was not significant as shown in Figure 4.5.

The next set of experiments was performed with only spindle rotation. The spindle speed was measured by pointing with a laser tachometer with an accuracy of $\pm0.05\%$ to the opening on the spindle housing [Figure 4.3].
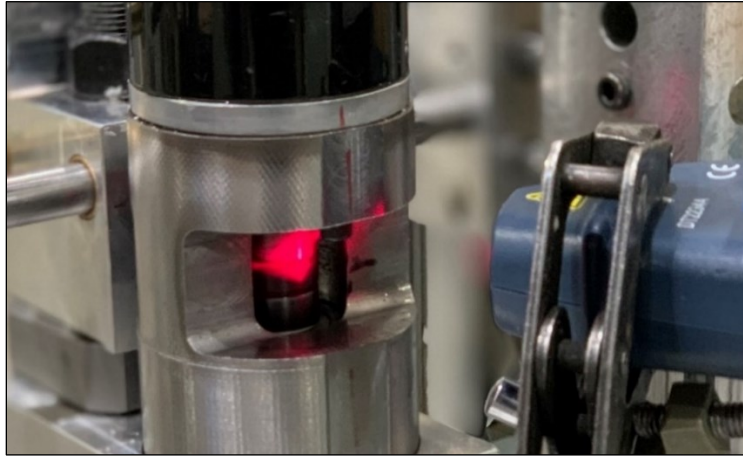
Figure 4.3: Laser Tachometer Measuring Spindle Speed.

The spindle speed was varied over 100, 500, 1000 and 3000 rpm. Tool diameter of 26.4 mm with a gap width of 2 mm from the tool to the outer boundary corresponds to shear rates of 69, 345, 690, 1035 and 2070 s^{-1}. Similar to the experiments with only orbital motion, these shear rates also span shear thickening regime of cornstarch slurry as shown in Figure 2.24. However, cutting edge honing was still not observed with the above testing conditions. The results are summarized in Figure 4.5.

Finally, orbital and spindle motions were combined to test the edge honing feasibility as shown in Figure 4.1 (c). The spindle speed was set to 1500 rpm with a gap width of 2 mm and 6 mm as shown in Figure 4.4 which corresponds to the shear rates of 2092 and 349 s^{-1} respectively. The leading edge as highlighted in orange, was measured before and after experiments.
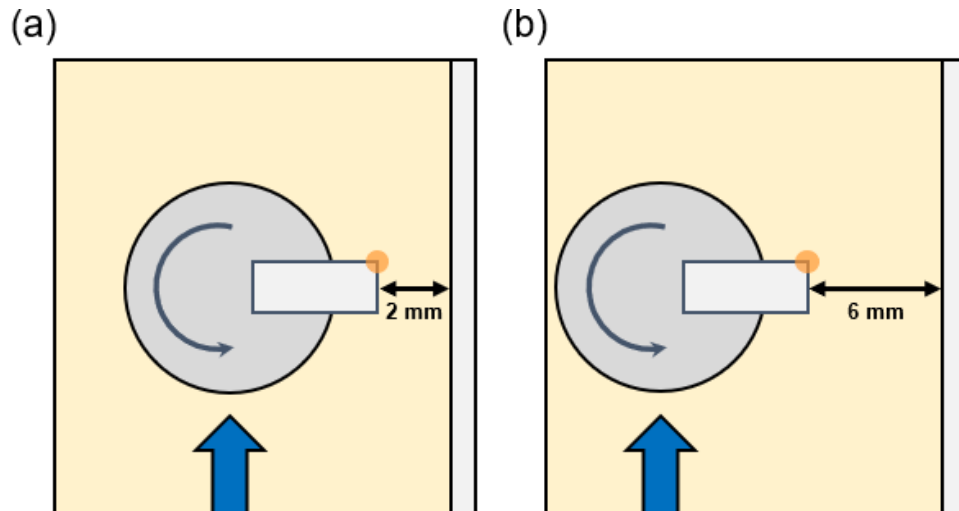
Figure 4.4: Combined Motions with (a) 2 mm and (b) 6 mm Gap Width.

As summarized in Figure 4.5, the combined orbital and spindle motions rendered a significant change in r_β and K values. For both 2 mm and 6 mm gap widths, r_β increased from 5 μm to almost 9 μm and K decreased from 0.7 to 0.32 and 0.55 respectively. Although the shear rates used in the orbital or spindle motion experiments covered the regime of before, during and after the shear thickening region of cornstarch slurry, r_β and K values of the inserts fell within the standard deviations of the values prior to the experiments. This concluded that the pressure generated solely by the shear thickening mechanism is not sufficient to edge hone the cutting inserts. The combined motions of orbiting and spinning were able to create a dynamic jammed domain in the presence of a rigid boundary as reported in [46]. This jammed domain provided a sufficient normal stress to indent the abrasives against the rotating and translating edges to remove material and thus hone it.
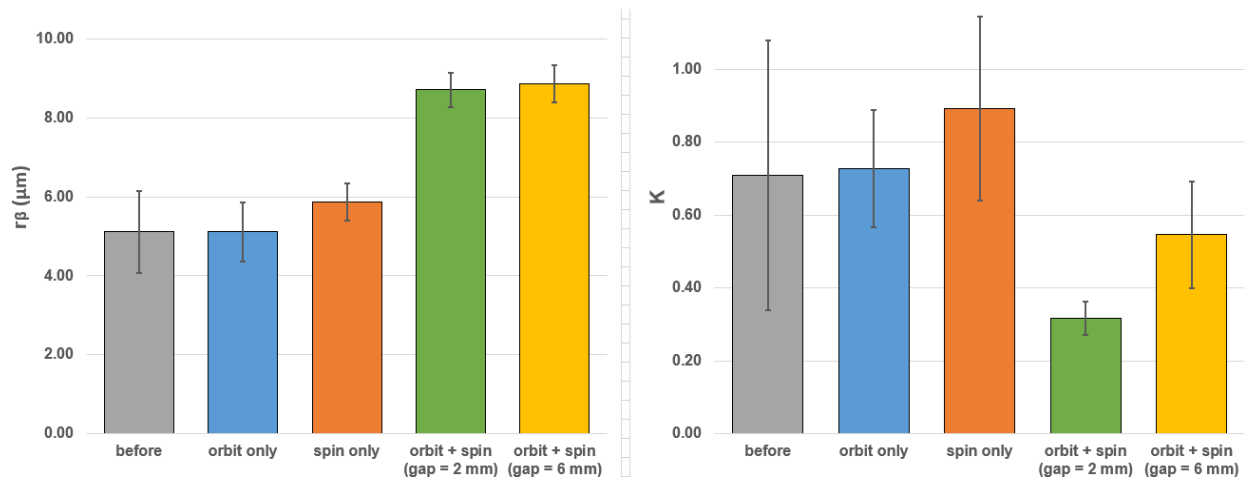
Figure 4.5: Effect of Orbital, Spindle and Combined Motions with Different Gap Widths on (a) Cutting Edge Radius and (b) Asymmetry.

When examining the cross-sectional profile of the honed insert, it was determined that r_β is not an effective parameter to characterize the performance from the preliminary experiments. Figure 4.6 shows a profile of a honed insert from the 2 mm gap width experiment. The honed cutting edge is asymmetric with a flank face segment length S_α being larger than rake face segment length S_γ. This indicates that the material removed from the flank face was considerably greater than that on the rake face and caused the characterization algorithm to fit a smaller circle on the profile. Unless the cutting edge is symmetrical, r_β cannot be used to compare the cutting edge honing performance.
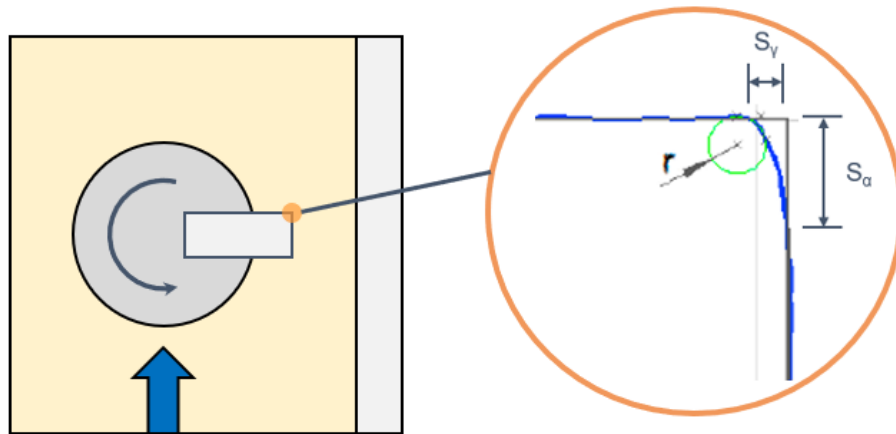
Figure 4.6: Honed Leading Edge with Asymmetric Profile.

Since the segment length shows a clearer response from the preliminary experiments, segment lengths S_γ and S_α were used to compare the edge honing performance instead of using r_β. As shown in Figure 4.7, solely orbital or spindle motion did not hone the cutting edges as $S\gamma$ and $S\alpha$ both fell within the variability prior to honing. Although the required critical shear rate to activate the shear thickening of cornstarch slurry was reached, the stress generated from such conditions in order to edge hone the cutting inserts was insufficient. However, when combining the orbital and spindle motions, S_α was dramatically increased. This provides an indication that the combined motions can render sufficient stress for the abrasives to remove material from the cutting tool edge. This agrees with the findings in [46] that the combined orbital and spindle motions in the non-Newtonian-abrasive slurry can create a dynamically jammed domain that causes a significant rise in normal force on the testing coupons for fine material removal through abrasion [Figure 2.45 (c)].
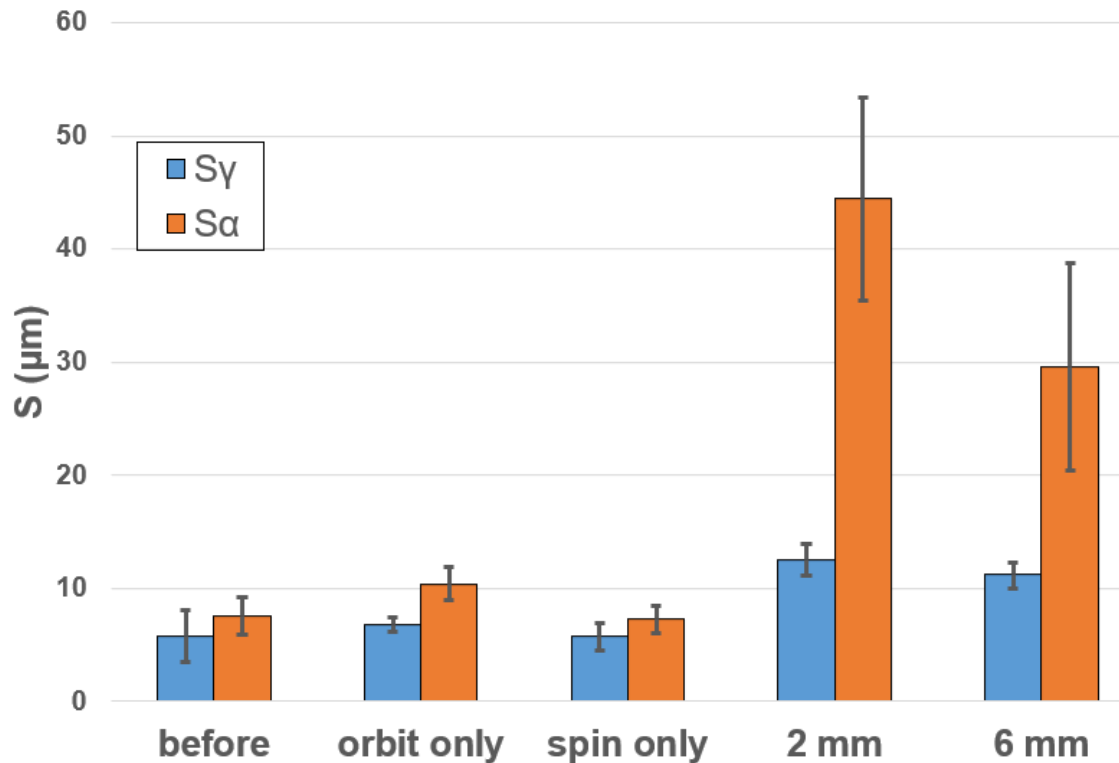
Figure 4.7: Effect of Orbital, Spindle and Combined Motions at Different Gap Widths on Segment Length S_{γ} and S_{α}.

From Figure 4.7, it is also evident that a decrease in gap size from 6 mm to 2 mm somewhat increased the cutting edge honing performance on S_{α}. This might be attributed to the jammed domain in front of the spindle experiencing a more intense squeeze flow (green arrows in Figure 4.8) with a smaller gap width. In addition, the jammed slurry has more difficulty exiting the jammed domain as the gap width is narrower. As a result, the highly strained and squeezed slurry is jammed in a smaller gap width thus producing a higher normal stress to hone the insert.
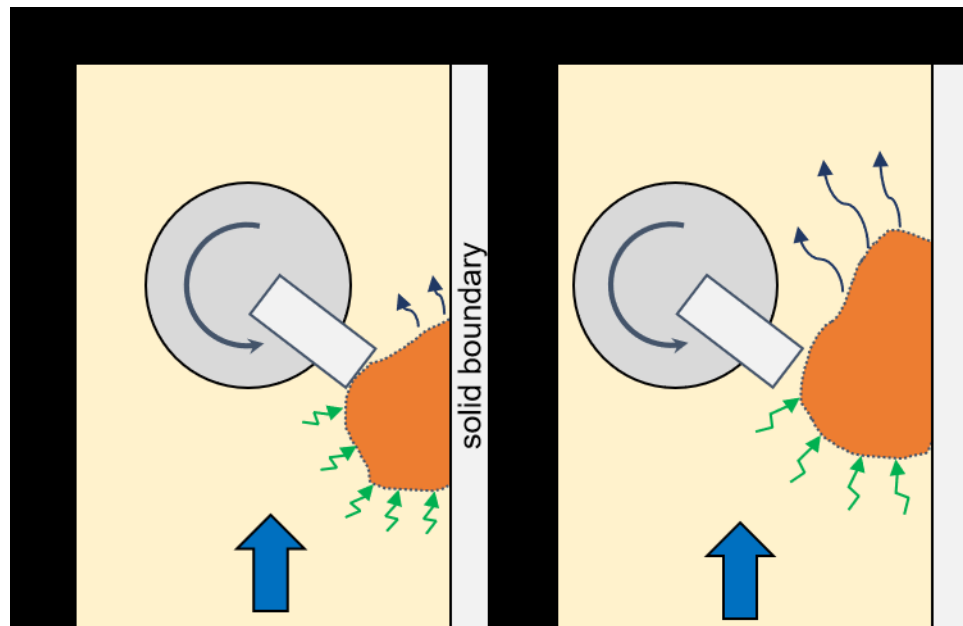
Figure 4.8: Illustration of the Effect of Gap Width on the Jammed Domain (a) 2 mm, (b) 6 mm Gap Width.

As reviewed in chapter 2, the presence of a rigid boundary can greatly affect the behaviour and magnitude of the normal stress due to the dynamically jammed domain. Therefore, further investigation on the effect of the solid boundary on edge honing performance was conducted by experimenting with different combinations of orbital and spindle motions as shown in Figure 4.10. As the slurry was orbiting in the same direction of the spindle [Figure 4.10 (a & c)], the leading edge S_α increased; whereas when the spindle rotated in the opposite direction, there was no significant changes to the S_α value. In addition, as the slurry orbits in the same direction of the spindle [Figure 4.10 (a & c)], a jammed and sheared slurry pile-up appeared in front of the spindle as shown in Figure 4.9 (a).The pile-up material exhibiting a matt surface (as opposed to glossy) is a signature of shear thickening. Alternatively, the pile-up disappeared when the spindle direction was reversed [Figure 4.9 (b)]. This indicates that the spindle motion redirects the slurry flow in

between the spinning tool and the rigid boundary. As a result, the slurry interacts with the rigid boundary and formed a dynamically jammed domain. Upon reversal of the spindle direction, the jammed domain cannot be sustained due to there being no interaction with the rigid boundary as the spindle redirects the flow away from the boundary. The pile-up is an indication of the development of the dynamically jammed domain in front of the spindle as the slurry was jammed in between the tool and the boundary. Thus, the dynamically jammed cornstarch and abrasive slurry honed the cutting insert which leads to an increase in S_α on the edge.
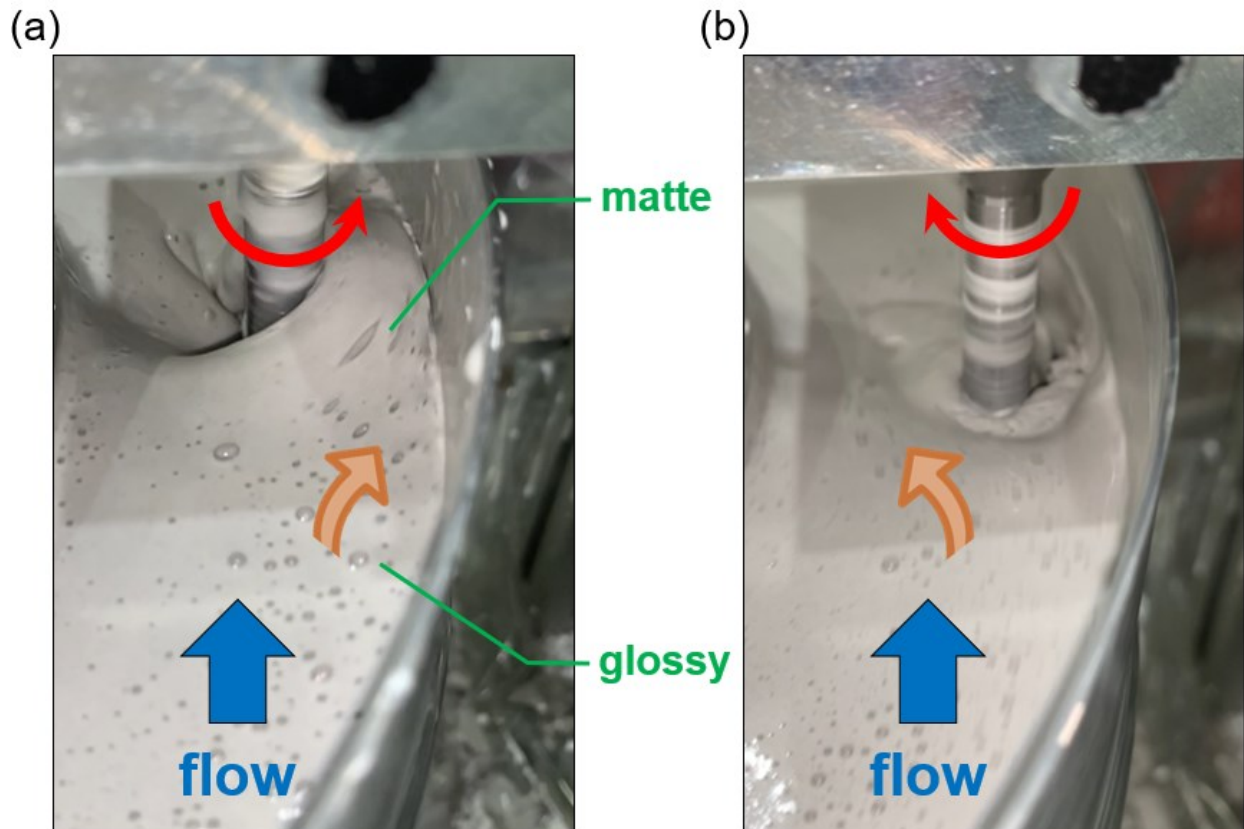
Figure 4.9: Orbit and Spin in (a) Same (b) Opposite Direction.
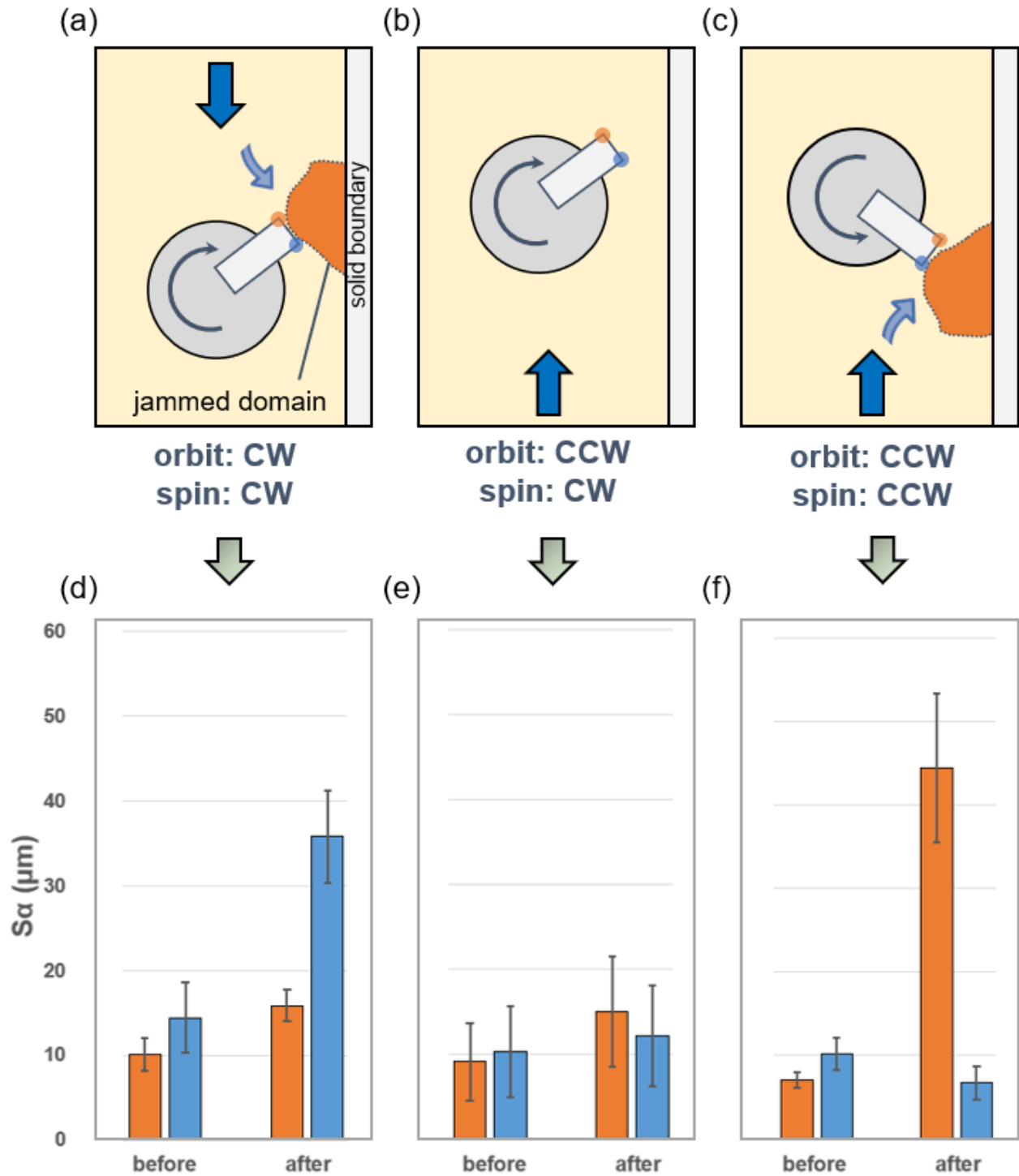
Figure 4.10: (a – c) Illustration of Orbital and Spindle Directions on Development of the Jammed Domain. (d – e) Honed Flank Face Segment Length S_α Correspond to the Honing Kinematics.

It was observed that the trailing edge showed a decrease in r_β in the above experiments. For example, the cutting edge highlighted in orange in Figure 4.10 (a) and the one highlighted in blue in Figure 4.10 (c) became sharper. SEM pictures were taken on the leading and trailing edges. As shown in Figure 4.11 (b), the leading edge has been rounded off and is particularly asymmetric with $S\alpha$ being much higher than $S\gamma$. In addition, abrasion tracks can be found on $S\alpha$ section in which they appear to be normal to the grind marks. In contrast, Figure 4.11 (a) shows the SEM picture of the trailing edge which has been sharpened. The grind marks on the flank face (top) have been completely polished with a smooth surface with no abrasive tracks.
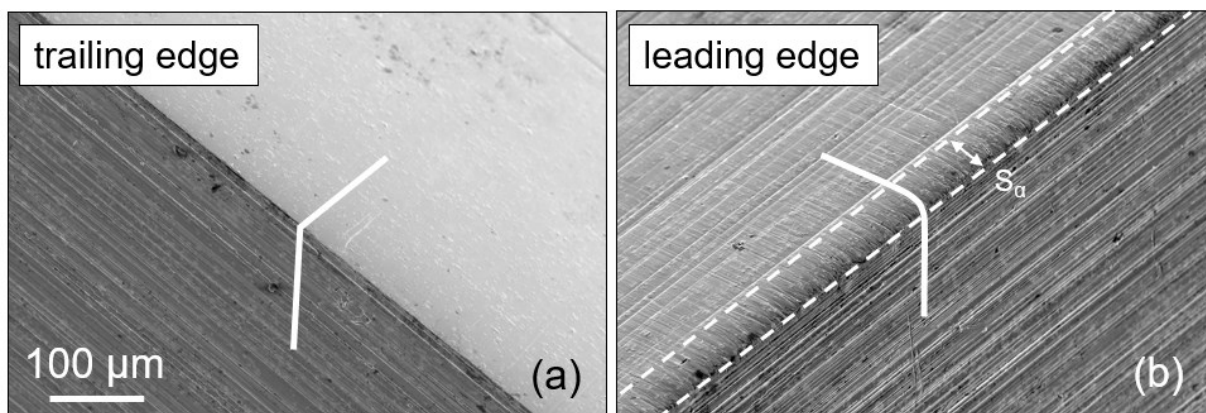
Figure 4.11: SEM Picture of (a) Trailing Edge (b) Leading Edge.

The surface topography of the top face of the insert has been further analyzed to understand the abrasive slurry flow. Figure 4.12 (a) shows the top surface where three distinct sections were observed based on the measured surface roughness: Section 1 appears to have the shortest segment length but a relatively smooth surface; Section 2 has the longest segment but a majority of the grind marks remained; Section 3 has the smoothest surface finish in which the grind marks are removed. The above observations

demonstrate that the abrasive slurry honed the leading edge as well as polish a small portion of section 1 and then separated off the surface. Figure 4.12 (b) shows possible slurry streamlines from the above findings. First, the leading edge cuts into the solid-like jammed domain. This honed the leading edge as well as polish a small portion of section 1. Then, the solid-like domain sheared and separated from the flank face resulting in the grind marks remaining intact in section 2. Finally, the jammed domain reattached to the flank face in section 3 where the relative velocity between the rotating insert and the abrasive slurry removed and polished the flank face leaving a smooth surface and a sharp edge.
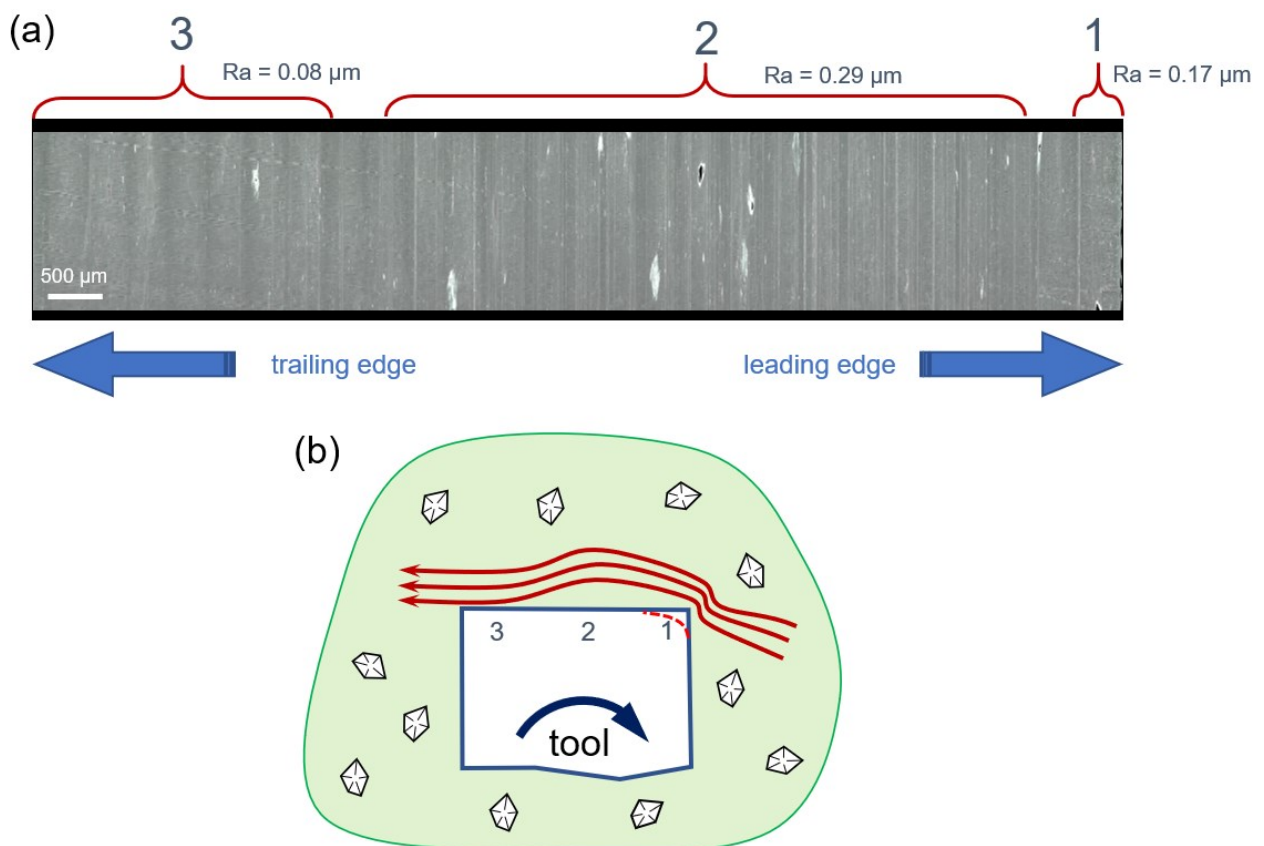
Figure 4.12: (a) Top View of the Insert (b) Deemed Slurry Flow.

A supplementary experiment was performed to confirm the sharpening effect as shown in Figure 4.13 (a). For the purpose of demonstrating such effect, an insert with a relatively large and symmetrical cutting edge radius (r_β = 44 µm, K = 1) on the trailing edge was used [Figure 4.13 (b & d)]. After five minutes of honing, the cutting edge radius was reduced to 15 µm [Figure 4.13(c)]. The sharpening action was due to the material being removed from the flank face as the abrasive slurry reattached itself to section 3 as illustrated in Figure 4.12 (b) which causes a significant reduction in r_β.
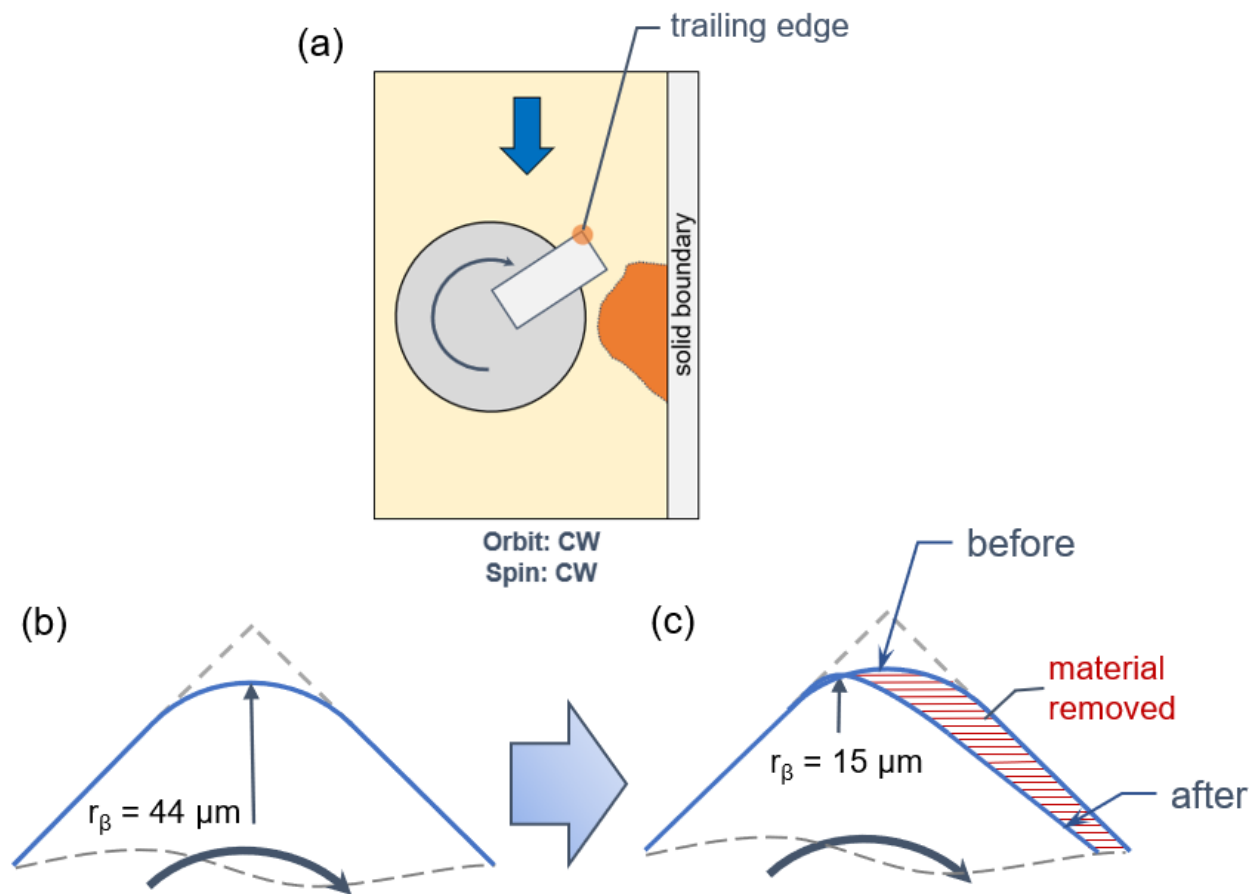
Figure 4.13: (a) Honing Kinematics (Trailing Edge Highlighted in Orange) (b) Trailing Edge Profile Before (c) Trailing Edge Profile Before Profile After Sharpening.

4.2   Drill Refurbishment

One of the interesting findings from Section 4.1 is that when the cutting edge cuts into the dynamically jammed domain, cutting edge honing happens; Contrarily, when the cutting edge exits such domain, r_β becomes smaller due to material removal from the flank face. This principle can be applied to refurbish worn solid tools such as drills and end-mills. Experiments were performed on drills to verify this.

Black oxide finished HSS twist drills of a diameter of 31/64" and point angle of 118˚ were used to perform the honing and sharpening experiments. The experimental parameters are listed in Table 4.1 and the experimental kinematics for both honing and sharpening experiments are as illustrated in Figure 4.14.

CS %	abrasive %		linear speed, direction (m/min)	spindle speed, direction (rpm)	gap (mm)	boundary config	time (min)
	17 μm	68 μm					
50	15	2.5	10, CCW	3000, variable	2.0	single	10

Table 4.1. Parameters for Drill Experiments.
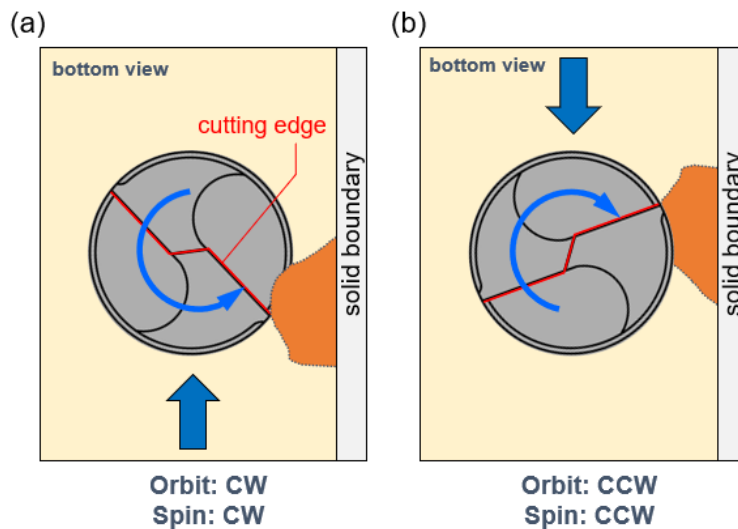
Figure 4.14: Bottom View for (a) Honing (b) Sharpening Drills.

Figure 4.15 (a) shows the edge honing results for a twist drill using the kinematic motions as shown in Figure 4.14 (a). It would be reasonable to assume that the edge radius would increase radially along the tool edge due to the increased local velocity. However, the results revealed a rather uniform r_β increased from an average of 6 μm to 12 μm. This might be due to the geometry of the twist drill affecting the slurry flow at the bottom edges. r_β near the center received almost no honing due to the zero linear velocity. Conversely, a severely chipped drill with varying r_β along tool edge was chosen for the sharpening experiment [Figure 4.15 (b)]. By reversing the rotational motion, the cutting edges become trailing edges which then exit the jammed domain causing a material removal on the flank face. As a result, cutting edge sharpening took place reducing the r_β to an average of 3 μm.
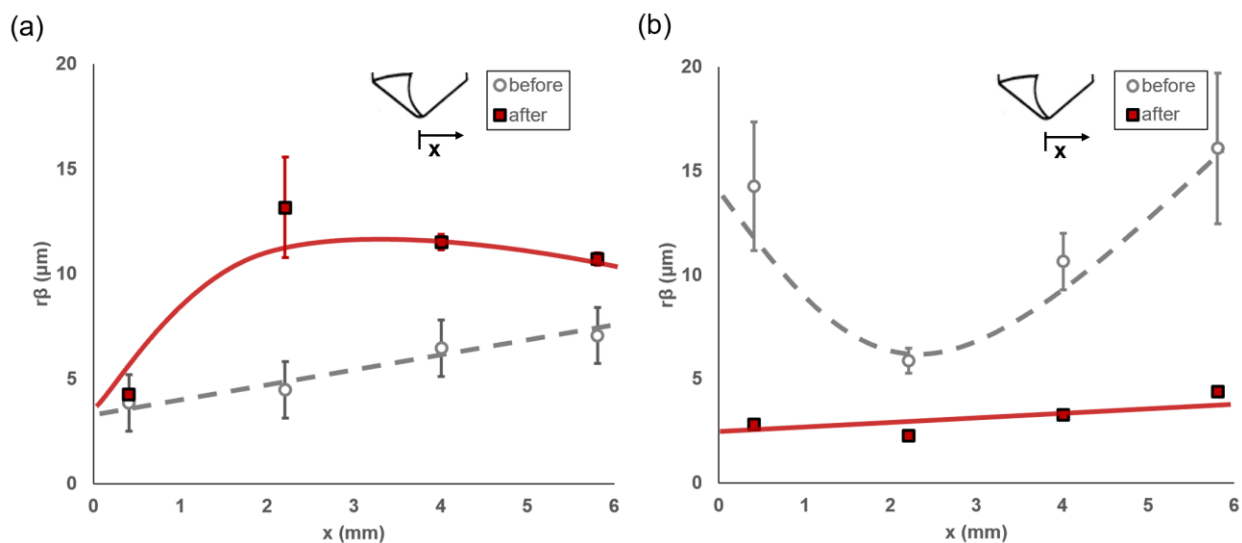
Figure 4.15: Cutting Edge (a) Honing (b) Sharpening Results for Drills.

4.3   Edge Asymmetry Experiments

From the preliminary experiments, the cornstarch-abrasive slurry demonstrated its ability to edge hone cutting tools through dynamic jamming instead of discontinuous shear thickening mechanism. However, the generated edges were asymmetric. It is hence imperative to develop a technique to control the edge asymmetry. In this section, the orientation of the insert relative to the tool holder was systematically varied to examine its influence on edge asymmetry.

During preliminary experiments, the square inserts were held radially in the tool holder [Figure 4.16 (a)], which generated edges with K value on the leading edge less than 1. This is due to the flank face of the insert experiencing more exposure to the jammed domain during the honing process. In other words, the asymmetry of the cutting edge can be controlled by varying the relative exposure of the rake and flank faces. To test this hypothesis, tool holders were manufactured with different θ so that the leading edge can cut into the jammed domain at different angles [Figure 4.16 (b)]; thus, allowing the jammed domain to hone the rake and flank faces differently. Table 4.2 lists the parameters used in the asymmetry experiments.
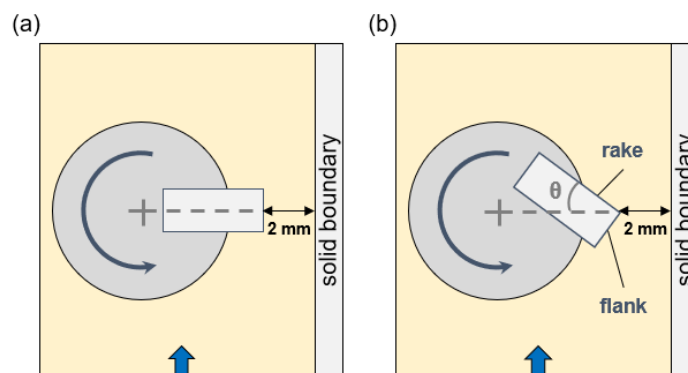
Figure 4.16: (a) 0˚ (b) θ = 23˚, 35˚, 45˚ Tool Holder.

CS %	abrasive %		linear speed, direction (m/min)	spindle speed, direction (rpm)	gap (mm)	boundary config	tool holder	time (min)
	17 µm	68 µm						
50	15	2.5	10, CCW	3000, CCW	2.0	single	variable	10

Table 4.2: Parameters for Edge Asymmetry Experiments.

As shown in Figure 4.17, K values increased with θ. This is due to θ controlling the level of exposure of rake and flank faces that cut into the dynamically jammed domain. As shown in Figure 4.19 (a - c), the lower the θ, the greater the surface area of flank face abraded by the jammed domain causing the increased flank segment. As θ increased, the rake face was exposed more to the jammed domain which resulted in the increased rake segment length. In order to obtain a symmetrical cutting edge, the rake and flank faces need to be equally exposed. It was found that when $\theta \approx 35°$, the cutting edge was symmetrical. Note that when cutting edge is honed to be symmetrical (K = 1), r_β is maximized even with the same honing parameters (that is except different θ) as shown in Figure 4.18. This is an artifact of the fitting algorithm that tends to fit a larger circle on the symmetrical edge compared to an asymmetric one. Three different honed edge profiles using tool holder configurations of θ = 23 °, 35° and 45 ° are as shown in Figure 4.19 (d - e) and the SEM pictures of the above configurations are as shown in Figure 4.20.
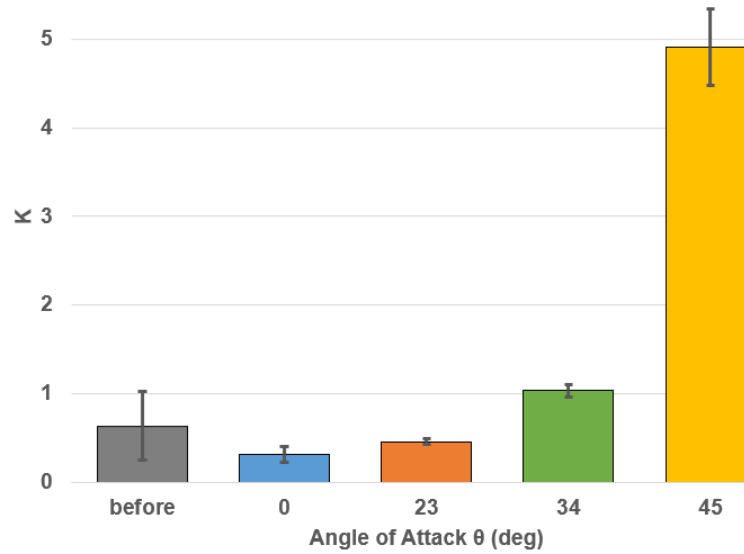
Figure 4.17: Cutting Edge Asymmetry K vs Angle of Attack θ.
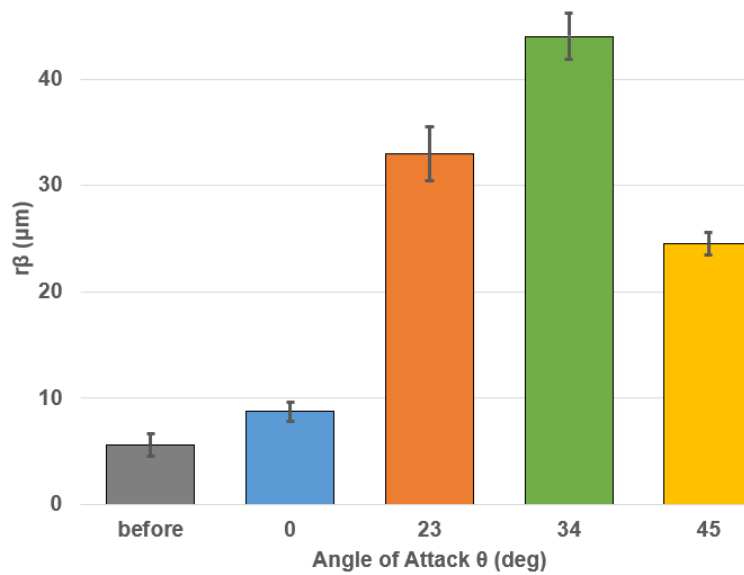
Figure 4.18: Cutting Edge Radius r_β vs Angle of Attack θ.
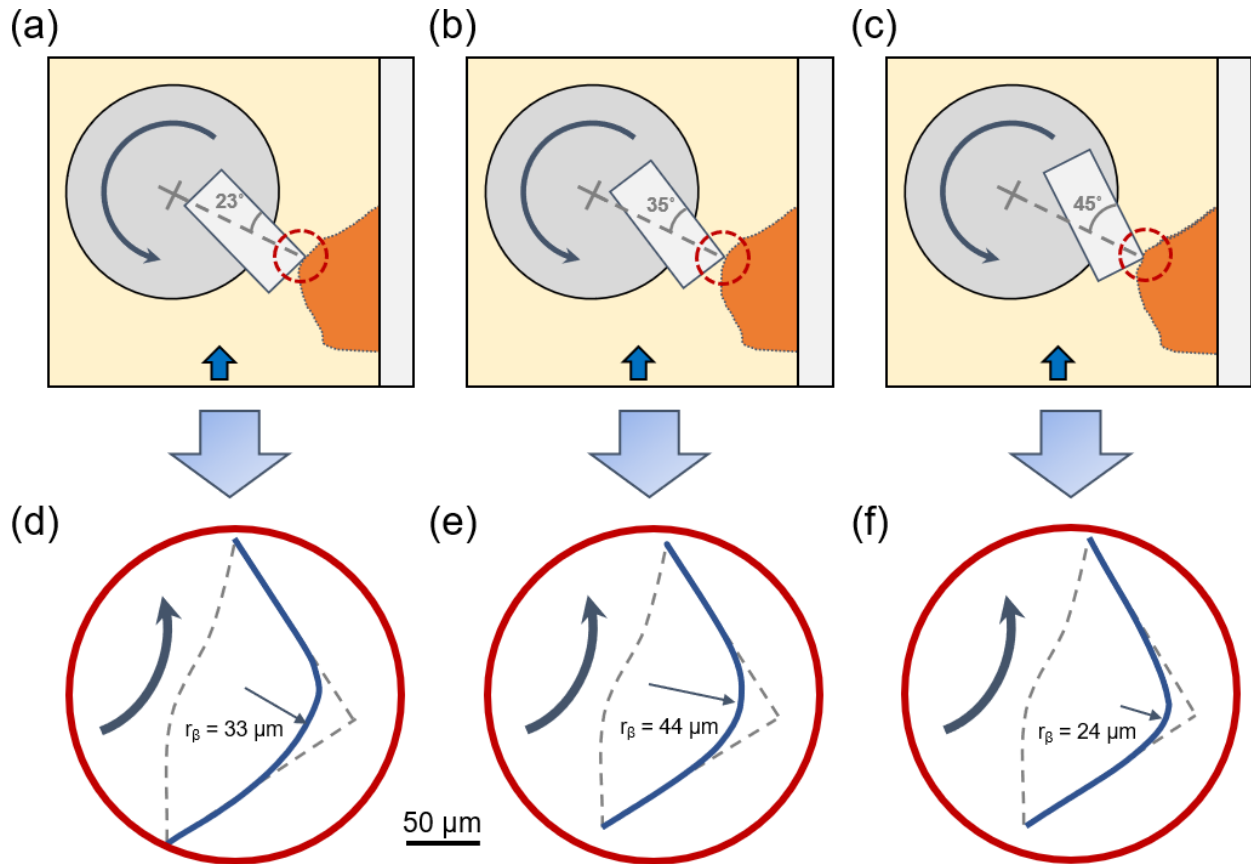
Figure 4.19: (a-c) Inserts of θ = 23˚, 35˚ and 45˚ Interact with Jammed Domain. (d-e) Honed Cutting Edge Profiles Correspond to Respective θ.
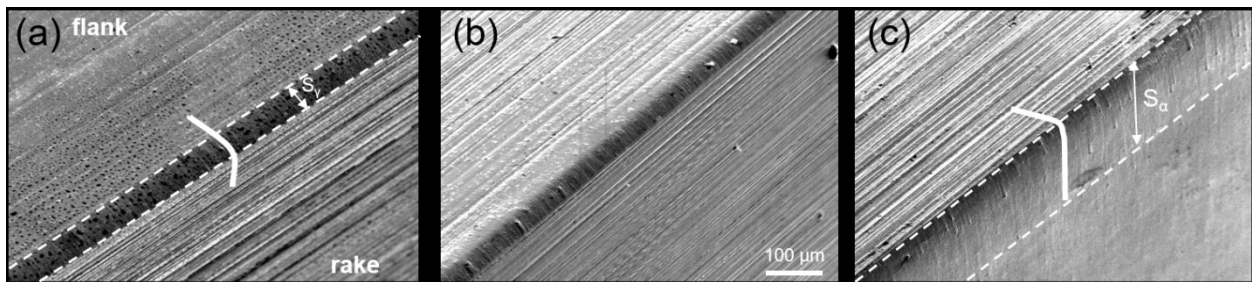
Figure 4.20: SEM Pictures of Honed Edges by Setting θ = (a) 23˚, (b) 35˚ and (c) 45˚.

4.4   Effect of Single and Twin Boundaries

Experiments were conducted to compare the edge honing performance using single and twin boundaries as illustrated in Figure 4.21.
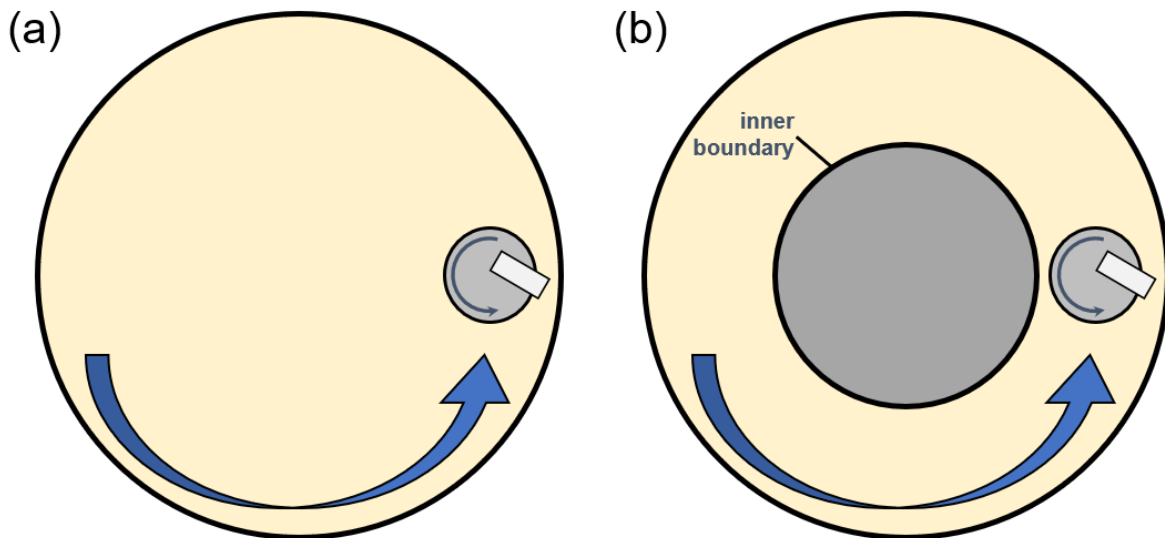
Figure 4.21: Single vs Twin Boundary Experiments.

During these experiments, a 35° tool holder was chosen as in Figure 4.21 to compare the honing performance as it produced symmetric cutting edges. Cutting inserts were honed for a total of 12 minutes but were taken out to measure r_β and K values every 2 minutes. The inserts were cleaned immediately prior to measurement as described in Section 3.2. Between experiments, a dummy tool on the spindle was used to prevent slurry segregation. The corresponding parameters are listed in Table 4.3.

CS %	abrasive %		linear speed, direction (m/min)	spindle speed, direction (rpm)	gap (mm)	boundary config	tool holder	time (min)
	17 µm	68 µm						
50	20	2.5	10, CCW	3000, CCW	2.0	variable	35°	12

Table 4.3: Parameters for Boundary Experiments.

As shown in Figure 4.22, the single boundary configuration seems to correspond to a slightly better performance during the first 4 minutes, after which the twin boundary configuration caught up. r_β reached 97 and 110 μm respectively for single and twin boundary experiments at the end. The difference is within the process inherent variability. Both experiments took only two minutes to reach r_β = 25 - 30 μm which is the typically required r_β value for machining stability as was reported by [9]. In addition, Figure 4.23 shows the edge asymmetry for both experiments converged from initially K ≈ 2 to K ≈ 1 in just 2 minutes. Note that the sizable standard deviation of K value before honing was due to the chipping from the ground inserts, which was significantly reduced after honing for just 2 minutes.
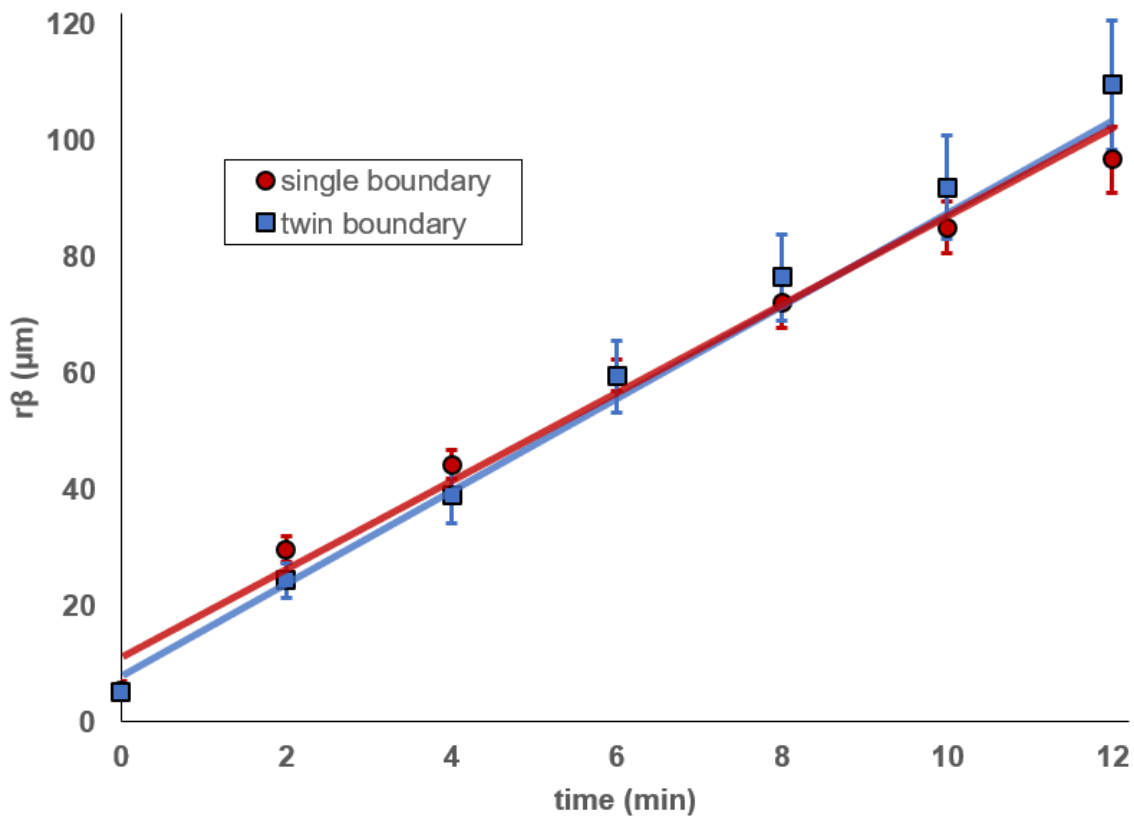
Figure 4.22: r_β vs Time for Single and Twin Boundary Experiments.
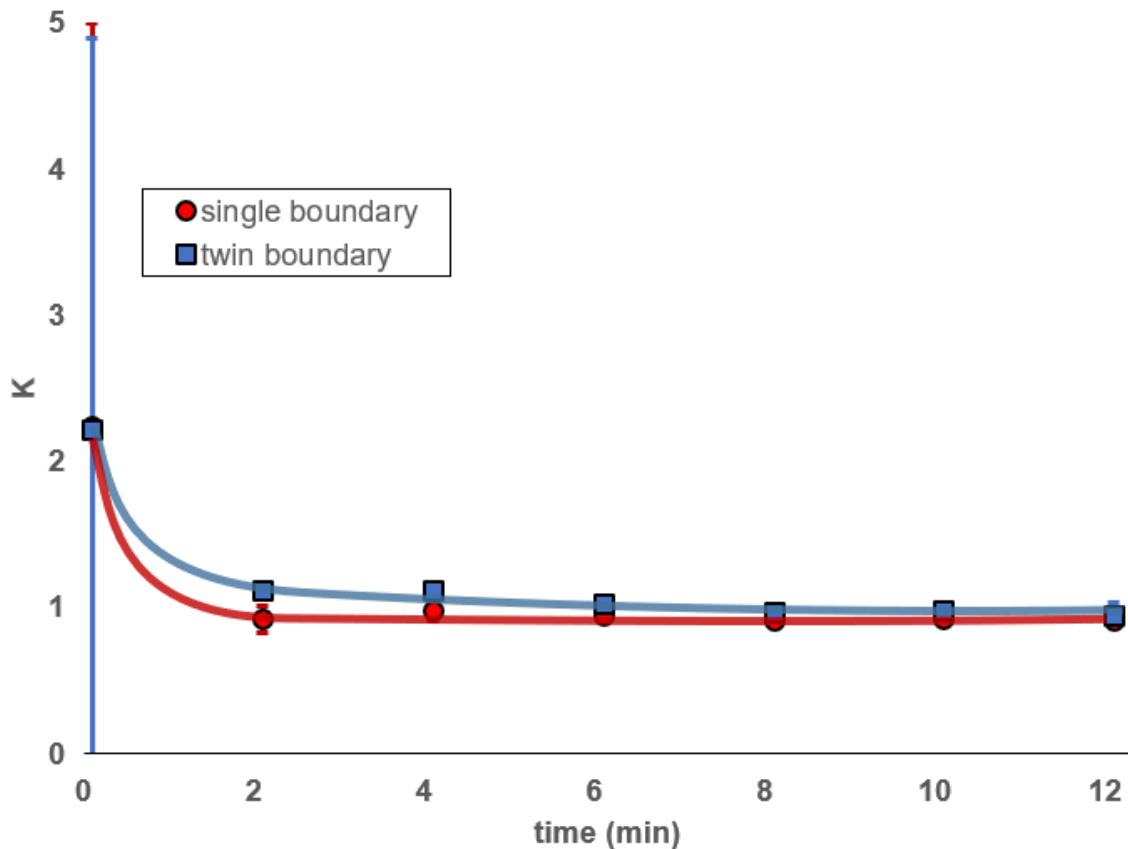
Figure 4.23: K vs Time for Single and Twin Boundary Experiments.

Although the force response was 1.5 times higher with the twin boundary configuration as reported in [46], the r_β values were similar for both boundary configurations. This proves that the jammed domain can only develop at one location where the spindle rotates and draw all the incoming slurry in between the boundary and the rotating tool (orange portion in Figure 4.24); at this location, the slurry is dynamically jammed as it interacts with the rigid outer boundary. The jammed domain cannot develop at the inner boundary side as the slurry was being directed to the outer boundary by the spindle. The higher forces in [46] appear to be related to the confinement of the slurry.

Although the inner boundary did not increase the edge honing performance, it reduces the volume of slurry required by ~60%. An appropriate inner boundary can hence effectively reduce honing cost by reducing the use of slurry and abrasives.
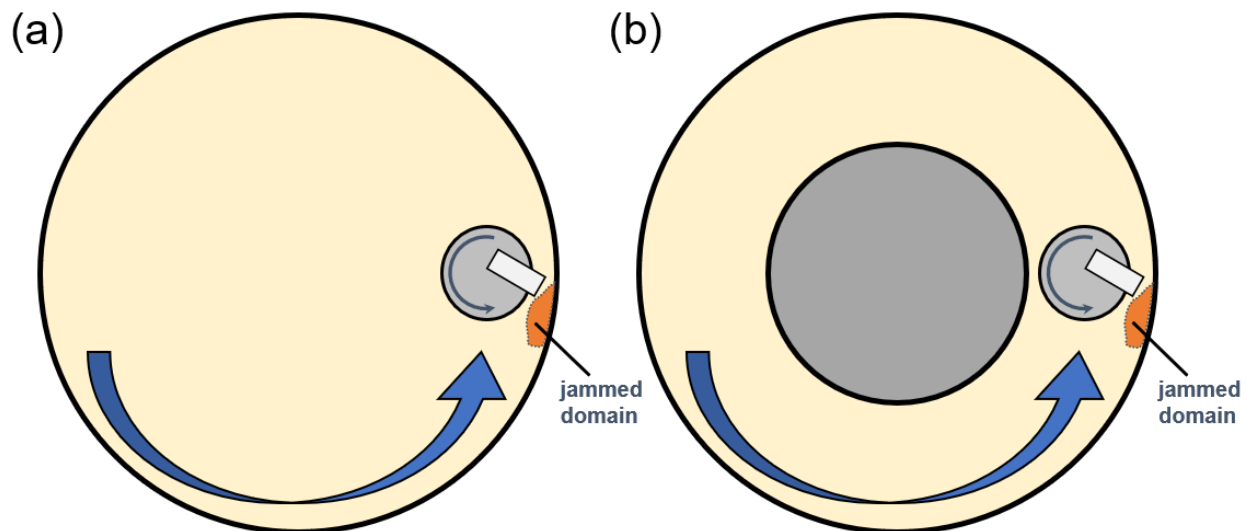
Figure 4.24: Jammed Domain in Both Single and Twin Boundary Configurations.

4.5   Effect of Cornstarch Percentage

The novel cutting edge honing process is significantly affected by the concentration of cornstarch in the slurry. It has been reported that the cornstarch percentage between 50 to 55% could vary the force response by up to 98% [49]. Experiments were hence performed to investigate the effect of cornstarch percentage on the honed microgeometry of cutting tools.

Cornstarch percentage experiments were performed by varying the cornstarch percentage from 48% to 51%. Cornstarch percentage was capped at 51% as a higher percentage would cause the jammed slurry in front of the tool to pile-up and spill over the

rotary boundary. The average r_β and K values were measured to examine the edge honing results. A 35° tool holder configuration was chosen to perform the experiments as symmetric and well-defined cutting edge radius were produced by such a tool holder as shown previously in Section 4.3. Experimental parameters for cornstarch percentage experiments are listed in Table 4.4.

CS %	abrasive %		linear speed, direction (m/min)	spindle speed, direction (rpm)	gap (mm)	boundary config	tool holder	time (min)
	17 μm	68 μm						
variable	15	2.5	10, CCW	3000, CCW	2.0	twin	35°	10

Table 4.4: Parameters for Cornstarch Percentage Experiments.

As shown in Figure 4.25, the cutting edge asymmetry K was affected by the cornstarch percentage. At low cornstarch percentage, a high K value was obtained but approached being symmetrical (K = 1) with increased cornstarch percentage. This is due to the inability of the less viscous jammed domain to hone the flank face segment. In addition, the cutting edge honed by the low cornstarch percentage slurry has K values fluctuating along the cutting edge which results in a relatively large standard deviation. The standard deviations were relatively lower for 50% and 51%; thus, it is not suggested to use a cornstarch percentage lower than 50% to hone cutting tools.
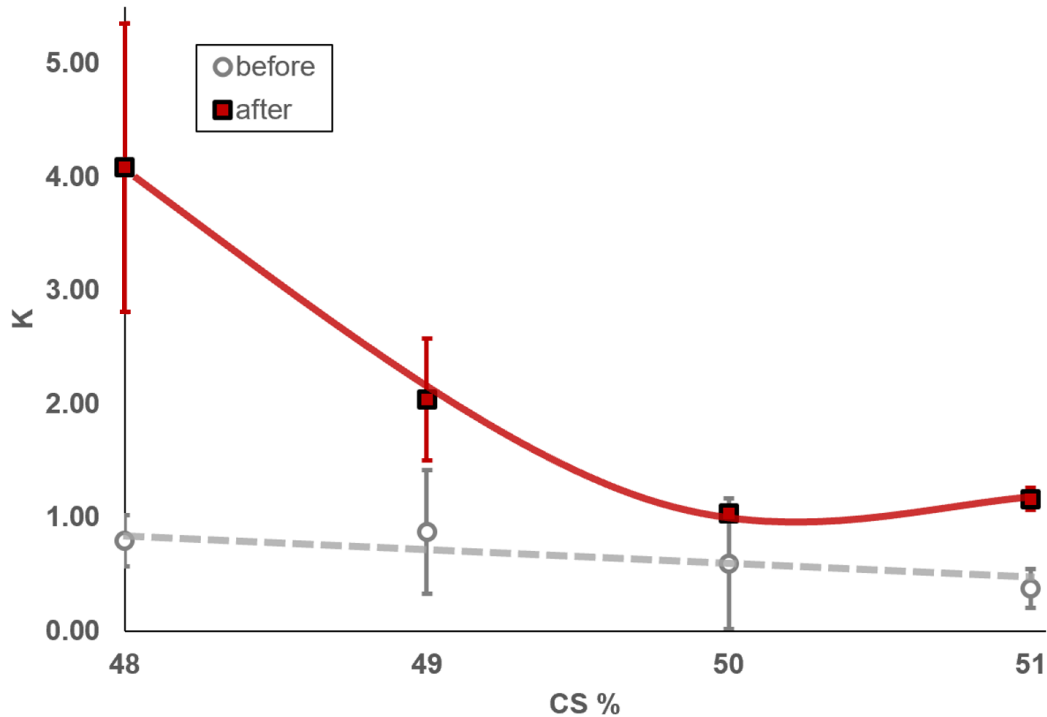
Figure 4.25: Cutting Edge Asymmetry K vs Cornstarch Percentages.

As shown in Figure 4.26, r_β correlated positively to the cornstarch percentage. The increased performance was due to the ability of the slurry to form a more intense and squeezed jammed domain that indented the abrasives more effectively to hone the cutting edge. Besides, the jammed domain was also more intense than the lower percentage one based on the observation that there was a lot more pile-up in front of the spindle. As a result, the jammed domain could generate higher normal stress and cause more effective abrasion for edge honing. Moreover, the low performance for 48 and 49 cornstarch percentage was not only due to the smaller and less jammed domain but also due to the asymmetrical cutting edge radius as indicated in Figure 4.25. As discussed before, the fitting algorithm tends to fit in a smaller circle onto an asymmetrical profile.
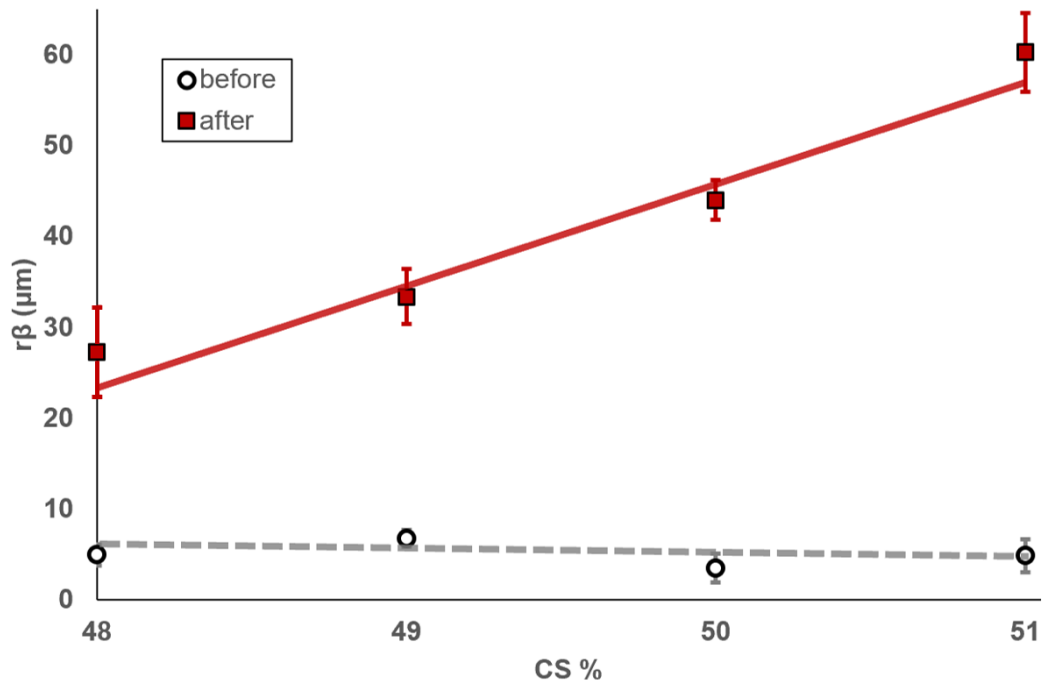
Figure 4.26: r$_\beta$ vs Cornstarch Percentages.

4.6   Effect of Process Kinematics

In the preliminary experiments, the combined orbital and spindle motions resulted in the formation of the dynamically jammed domain in front of the spindle. In the following, these two parameters were varied along with different parameters such as cornstarch percentage to examine the effect on the honing performance. Note that some error bars are omitted for better readability; the maximum standard deviation was 20%.

First, spindle speed experiments were performed by varying the spindle speed from 1500 to 3500 rpm while using two cornstarch percentages: 50% and 51%. The experimental parameters are listed in Table 4.5 below.

CS %	abrasive %		linear speed, direction (m/min)	spindle speed, direction (rpm)	gap (mm)	boundary config	tool holder	time (min)
	17 μm	68 μm						
variable	15	2.5	10, CCW	variable, CCW	2.0	twin	35°	10

Table 4.5: Parameters for Spindle Speed Experiments.

As shown in Figure 4.27, an increase in spindle speed generally leads to an increase in r_β for both cornstarch percentages as the jammed domain can generate higher normal stress. These results agree with Preston's law stating that the material removal rate is positively related to the pressure and velocity [50]. However, the edge honing performance reduced when the spindle speed increased from 3000 to 3500 rpm for a cornstarch percentage of 50%. This was due to the increase in spindle speed leading to the formation of a vortex around the tool body [Figure 4.28] which prevents the cutting insert from being honed by the dynamic jammed domain. Similar finding was reported in [49] that the high spindle speed would lead to a creation of vortex which decreased the surface finishing ability of the non-Newtonian-abrasive slurry. In order to reduce or eliminate the vortex formation, cornstarch percentage was increased from 50% to 51%. This is due to the increase in viscosity leading to higher energy dissipation through friction. At 51% cornstarch, there was no decrease in performance when the spindle reached the highest speed of 3500 rpm, and the insert was honed to an edge radius of 65 μm.
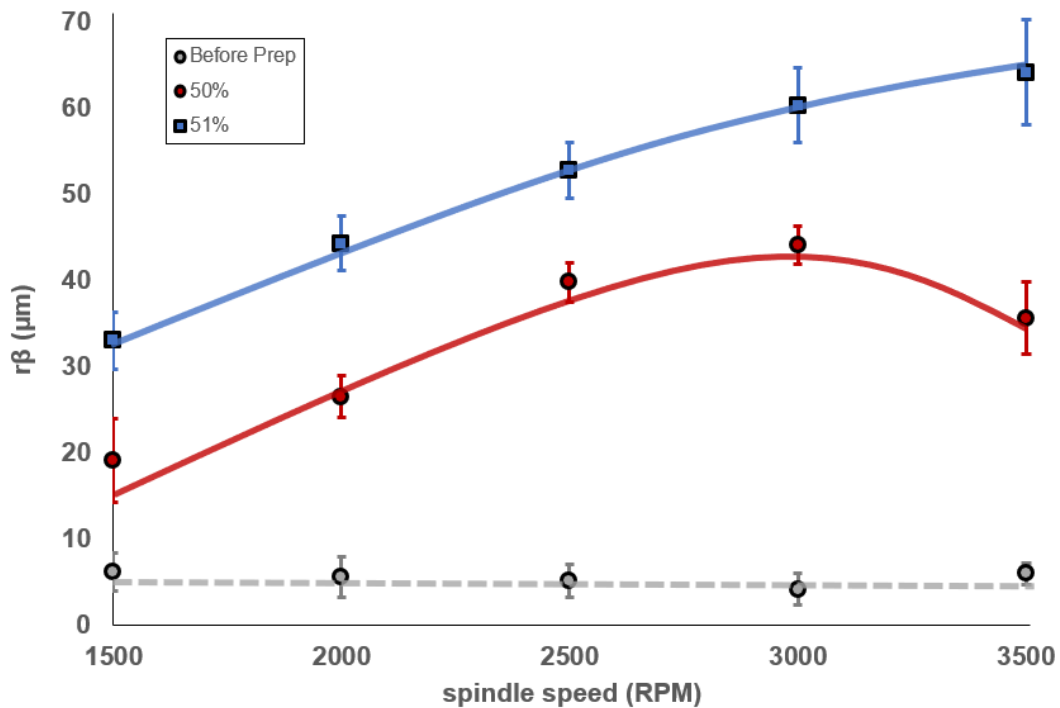
Figure 4.27: r_β vs Spindle Speed at Two Cornstarch Percentages.

Figure 4.28: Vortex Formation at High Spindle Speed.

Next, linear speed experiments were performed by varying over 2.5, 5, and 10 m/min. r_β was measured along the cutting edge from the bottom as discussed in Section 3.2.1 (Measurement Scheme). The experimental parameters are listed in Table 4.6 below.

CS %	abrasive %		linear speed, direction (m/min)	spindle speed, direction (rpm)	gap (mm)	boundary config	tool holder	time (min)
	17 µm	68 µm						
50	15	2.5	variable, CCW	3000, CCW	2.0	twin	35°	10

Table 4.6: Parameters for Linear Speed Experiments.

An interesting observation was made during the orbital speed experiments. As shown in Figure 4.29, r_β was uniform along the cutting edge when the linear speed was at 10 m/min. However, when the linear speed was halved to 5 m/min, a gradient edge was generated with a larger r_β at the lower end of the tool. Further decreasing the linear speed to 2.5 m/min increased the gradient along the tool edge, and also the performance at each location, in comparison to the higher linear speeds.
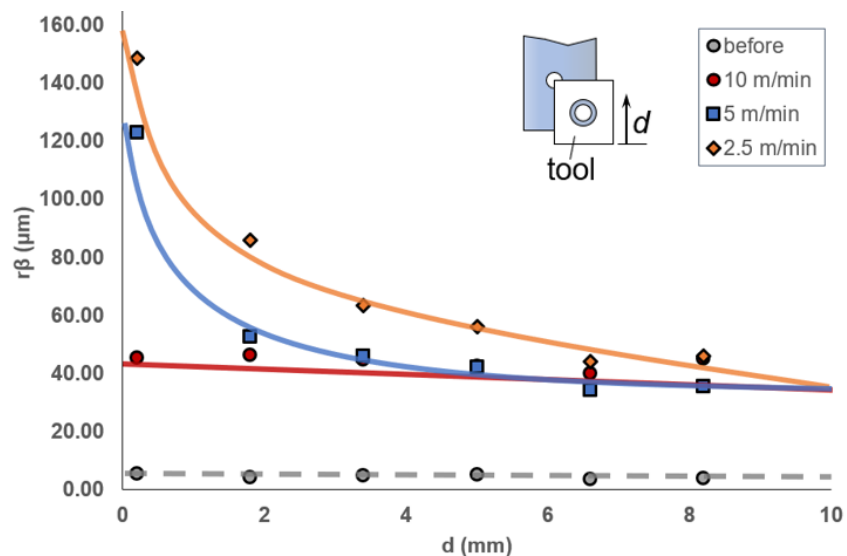
Figure 4.29: r_β vs Tool Height d at Varying Orbital Speeds.

The gradient in edge radius may be due to the segregation of the Al_2O_3 abrasives in the cornstarch slurry. When the linear speed was halved, the slurry would take twice the amount of time to rotate one revolution. This means the abrasives have double the time to sediment to the bottom of the rotary boundary until they would be remixed by the spindle. The segregated abrasives at the bottom of the rotary boundary would more aggressively hone the bottom of the cutting tool which then produced a large r_β near the bottom of the tool. To verify the segregation effect, the linear speed experiment was modified by introducing a secondary spindle on the opposite side of the current testing spindle as shown in Figure 4.30. The additional spindle would serve as a mixer to agitate the slurry. If the sink effect is present, the resultant r_β with twin spindle should have less gradient along the cutting edge than the single spindle case. The linear speed of 2.5 m/min was used since the resultant honed edge showed the most gradient edge radius. The secondary spindle was operated with the same parameters as the testing spindle.
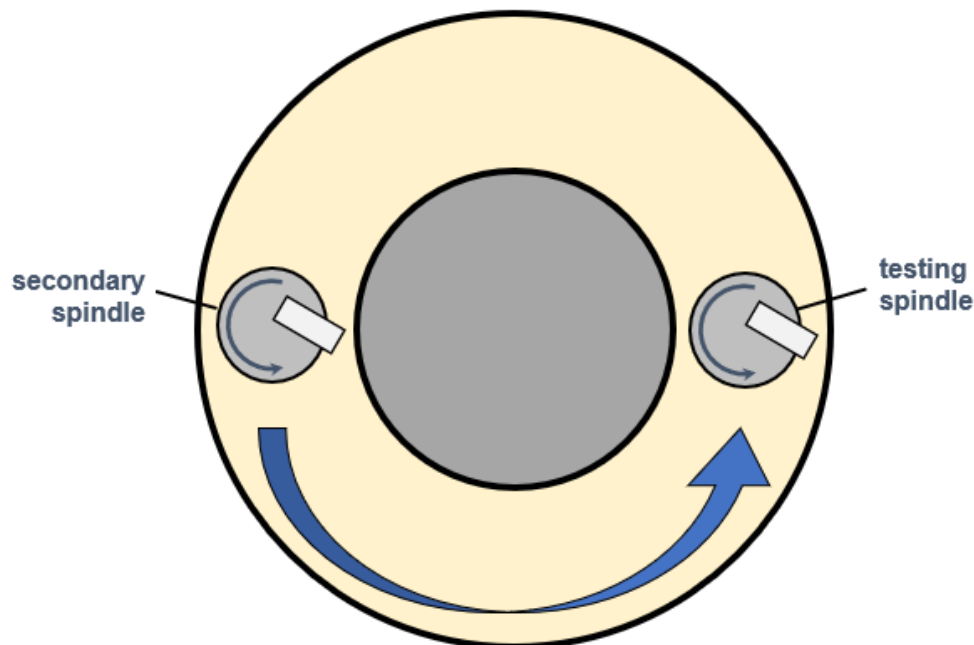
Figure 4.30: Twin Spindle Setup.

Figure 4.31 compares the results of using a single spindle and having a secondary spindle on the opposite side. It is clear that adding a secondary spindle significantly reduced the gradient of the honed edge. This verifies that the abrasive would sink if the rotary boundary does not rotate fast enough for the abrasive to mix well. However, the sinking effect can be utilized for a cutting tool that requires more honing at the bottom for such edges as ball-nose tools that refer to a zero velocity at the center.
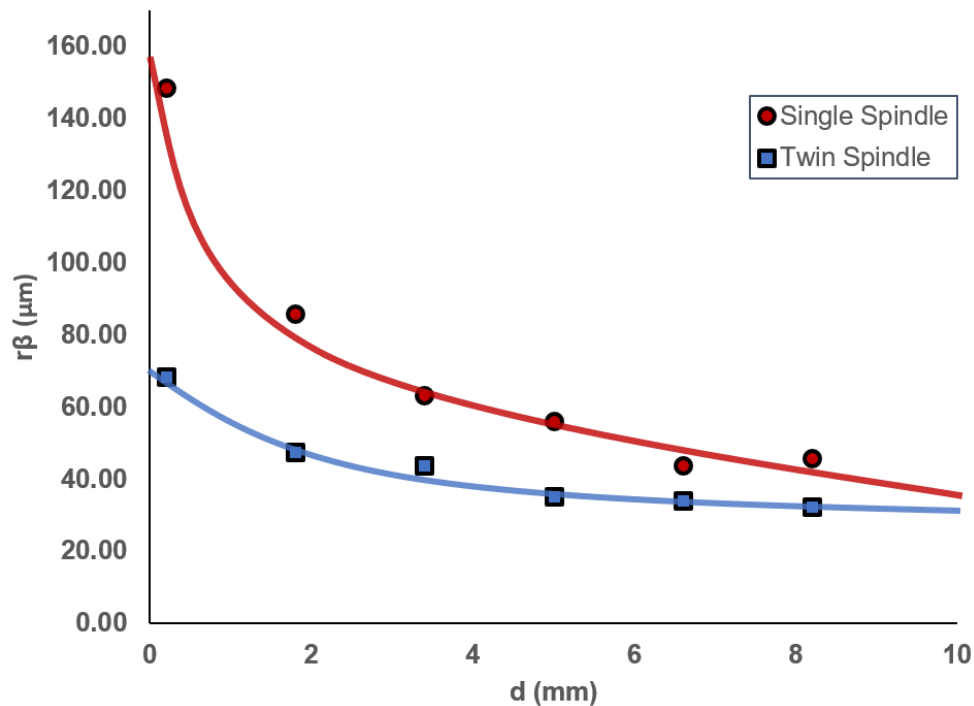
Figure 4.31: Single vs Twin Spindle Configuration with 2.5 m/min Linear Speed.

4.7   Effect of Abrasive Grit Size

During the novel edge honing process, the combined orbital and spindle motions develop a dynamically jammed domain in front of the tool in which the abrasives are held. The suspended abrasives remove materials from the tool edge as the rotating tool cuts

repeatedly through the dynamically jammed domain. The abrasive size and percentage play important roles in determining how well they are being suspended in the suspension as well as controlling the material removal rate through abrasion. Besides, the size and amount of abrasive would dramatically affect the rheological behaviour of the shear thickening fluids [51]. In the following section, different parameters in terms of the abrasive were experimented to study the effect on the cutting edge micro-geometry.

First, abrasive size experiments were conducted by varying the size of the Al_2O_3 abrasives to examine the effect on the cutting edge. Al_2O_3 abrasives of 3, 17, 30, 68 and 120 μm with 15% of the total weight of the cornstarch slurry were prepared for five individual experiments. The experimental parameters are listed in Table 4.7.

CS %	abrasive size (μm)	abrasive %	linear speed, direction (m/min)	spindle speed, direction (rpm)	gap (mm)	boundary config	tool holder	time (min)
50	variable	15	10, CCW	3000, CCW	2.0	twin	35°	10

Table 4.7: Parameters for Abrasive Size Experiments.

Figure 4.32 shows the results of the honed radius along the cutting edge. It is fascinating to find out that the data shows two different trends. With 3, 17 or 30 μm Al_2O_3, an uniform and similar size of the radius was honed along the cutting edge; the 68 or 120 μm both produced a gradient r_β with a more substantial honed performance close to the bottom while the 120 μm achieved slightly higher performance. The abrasives segregate in the cornstarch slurry if their size is larger than a threshold. This might be attributed to the Brazilian Nut effect in which two species of granular materials are segregated under shear and gravity [52]. In some cases, larger particles are forced upward as the smaller particles try to fill in the voids that are beneath the large particles nucleated by the agitation. The large particles may even sink or suspend evenly in the mixtures depending

on the segregation criteria. However, the criteria are complex and can be affected by the mixture contents, size, density, shape, roughness and boundary conditions. In our case, the 68 μm Al_2O_3 particles have higher density and larger particle size than the cornstarch particles (15.8 ± 4.7 μm in diameter) [31] in which they seemed to segregate downward to the bottom.
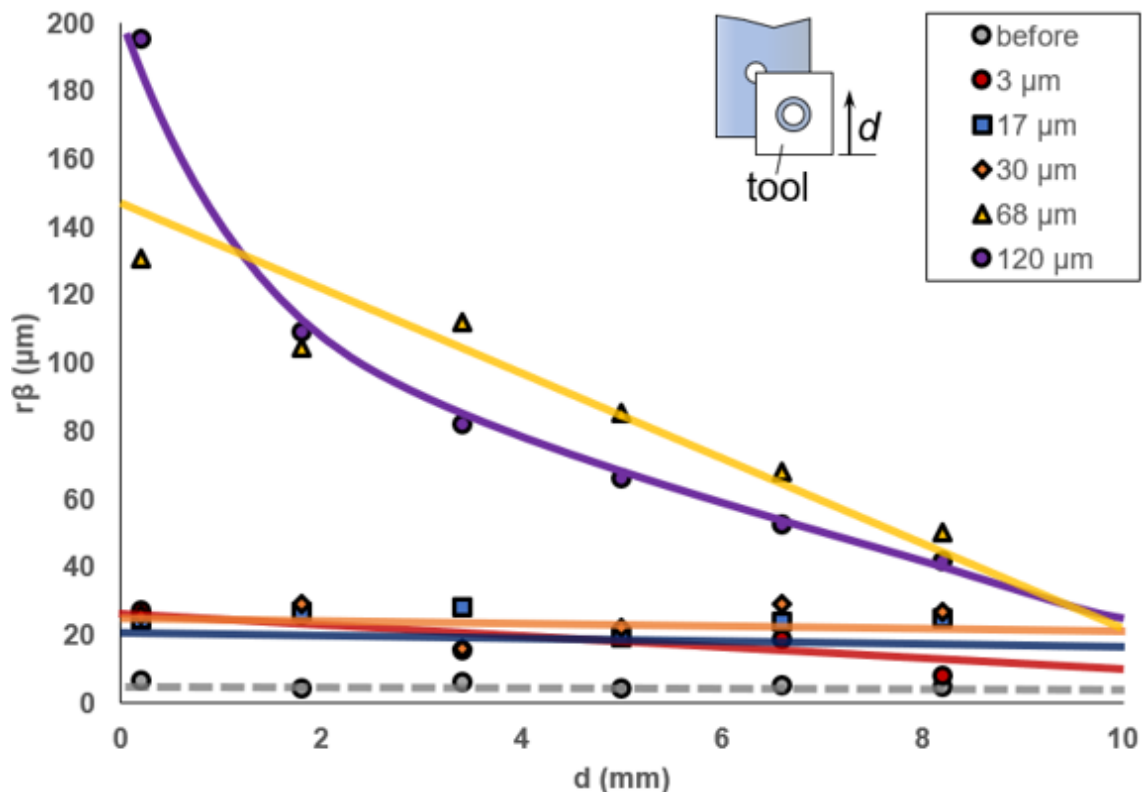
Figure 4.32: Effect of Different Abrasive Sizes on r_β.

On the other hand, the 17 μm Al_2O_3 has a similar particle size to the cornstarch particles and was able to mix evenly with the cornstarch slurry to produce a homogenous slurry. Such segregation was also captured when the slurry was being tumbled. Figure 4.33 shows two different batches of slurry that were being mixed for 30 minutes. The one with 17 μm became homogenous, while 68 μm showed stratification bands. The shear

action of the tumbler segregated the 68 µm Al_2O_3 and cornstarch particles into the stratification bands.

(a) homogenous   (b) stratification band
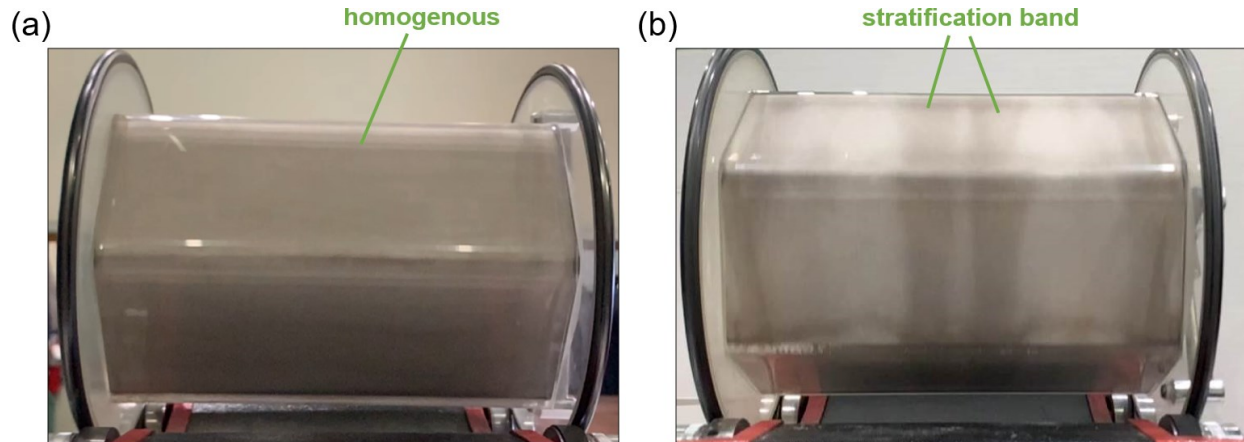
Figure 4.33: (a) 17 µm (b) 68 µm Al_2O_3 Mixing with Cornstarch Slurry in a Tumbler.

Abrasive percentage experiments were done by comparing the average r_β with different percentages of Al_2O_3 (0 to 20%). However, only abrasive sizes that can produce an uniform r_β along the cutting edge were used as the experiments were to compare the average r_β. Experimental parameters are listed in Table 4.8.

CS %	abrasive size (µm)	abrasive %	linear speed, direction (m/min)	spindle speed, direction (rpm)	gap (mm)	boundary config	tool holder	time (min)
50	variable	vary	10, CCW	3000, CCW	2.0	twin	35°	10

Table 4.8: Parameters for Abrasive Percentage Experiments.
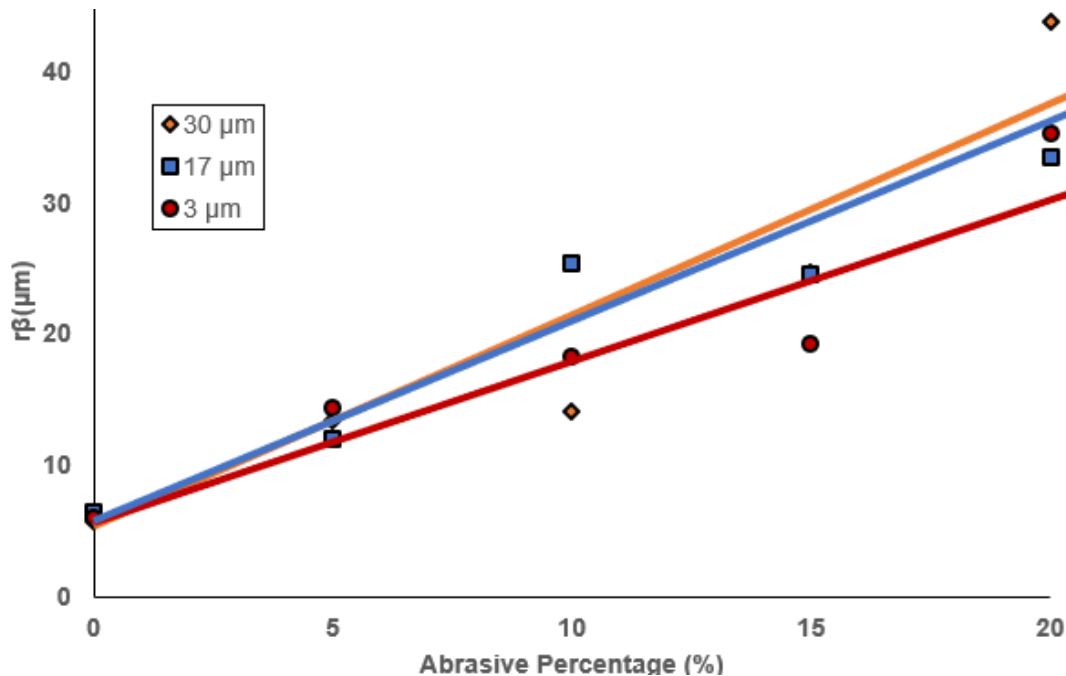
Figure 4.34: r_β vs Abrasive Percentage at Various Abrasive Sizes.

As shown in Figure 4.34, the average r_β is positively related to the amount of abrasive in the slurry. The maximum percentage of abrasives was capped at 20% because additional abrasives would increase the viscosity [51] and lead to slurry spillage. The average r_β honed by these three sizes of abrasive was similar, although the one with 3 μm seems to have slightly lower results. This is due to the inability of fine abrasive to remove materials as compared to the other two sizes. Figure 4.35 shows the cutting edge scanned by the white light optical system. The cutting edge that is honed by the slurry with 3 and 17 μm have a poor edge quality which proves the inability to remove material by the fine Al_2O_3. This agrees with findings from Span [46] that the finer abrasive was unable to remove deep scratches on the testing coupon using cornstarch-abrasive slurry.
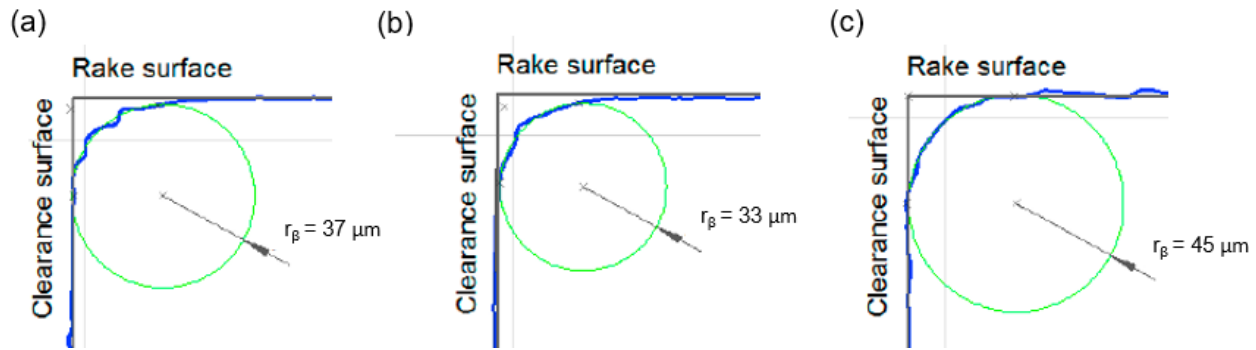
Figure 4.35: Cutting Edge Topography Honed by Cornstarch Slurry with Al_2O_3 of (a) 3 μm (b) 17 μm and (c) 30 μm.

Next, the segregating effect of the larger size abrasives was confirmed by repeating the above abrasive size experiments of 68 and 120 μm with the twin spindle setup [Figure 4.30]. This is to compare the change in r_β along the cutting edge with and without the twin spindle. As shown in Figure 4.36, both 68 and 120 μm show a decreasing trend of gradient after using a twin spindle setup. This proves that the twin spindle is able to agitate the larger size abrasives in the slurry to reduce sinking to the bottom. As a result, additional spindles can be used as a means to control the honed gradient radius of the cutting edge.
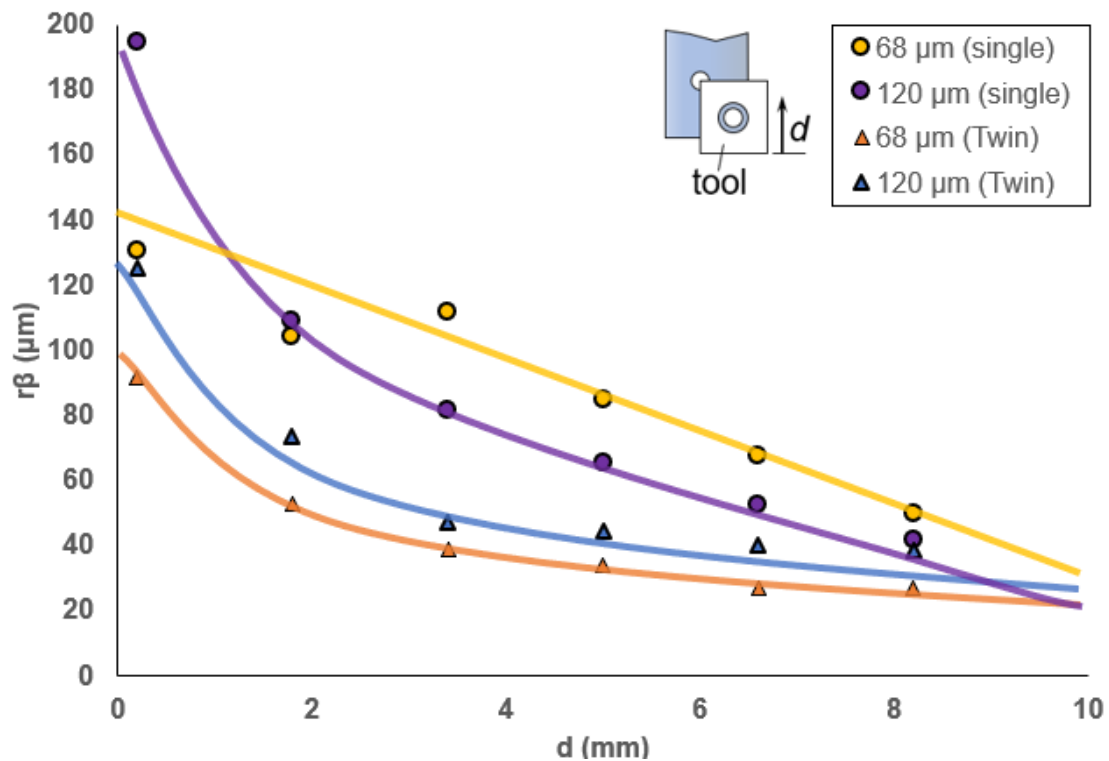
Figure 4.36: Single vs Twin Spindle Experiments for 68 and 120 µm Al_2O_3.

Since the 17 µm Al_2O_3 can be suspended well in the cornstarch fluid to create a homogenous slurry and the 68 µm Al_2O_3 can produce a relatively high performance, an additional experiment was performed by mixing these two sizes of abrasive in order to exploit their advantages. This time, 15% of 17 µm and 2.5% of 68 µm Al_2O_3 were added to the cornstarch suspension to perform the experiment. Other parameters remain the same as listed previously in Table 4.7.

As shown in Figure 4.37, the combination of 17 and 68 µm Al_2O_3 was able to double the performance than using just 17 µm of Al_2O_3. The segregating effect of the 68 µm Al_2O_3 was also eliminated and an uniform r_β was fabricated along the cutting edge. The addition of a ternary particle distribution promotes a better mixing as reported in [53]. A separate tumbling experiment was performed by mixing 50% CS, 15% 17 µm and 15%

124

68 µm Al_2O_3. As shown in Figure 4.38, suspension in the tumbler did not show any stratification bands as was in Figure 4.33 (b). This indicates that the addition of 17 µm Al_2O_3 was able to act as a dispersing agent in the slurry to suspend the larger size of abrasive. Thus, mixing both sizes of abrasive can take advantage of the homogeneity of the 17 µm Al_2O_3 and cornstarch slurry as well as the high material removal rate of the 68 µm Al_2O_3.
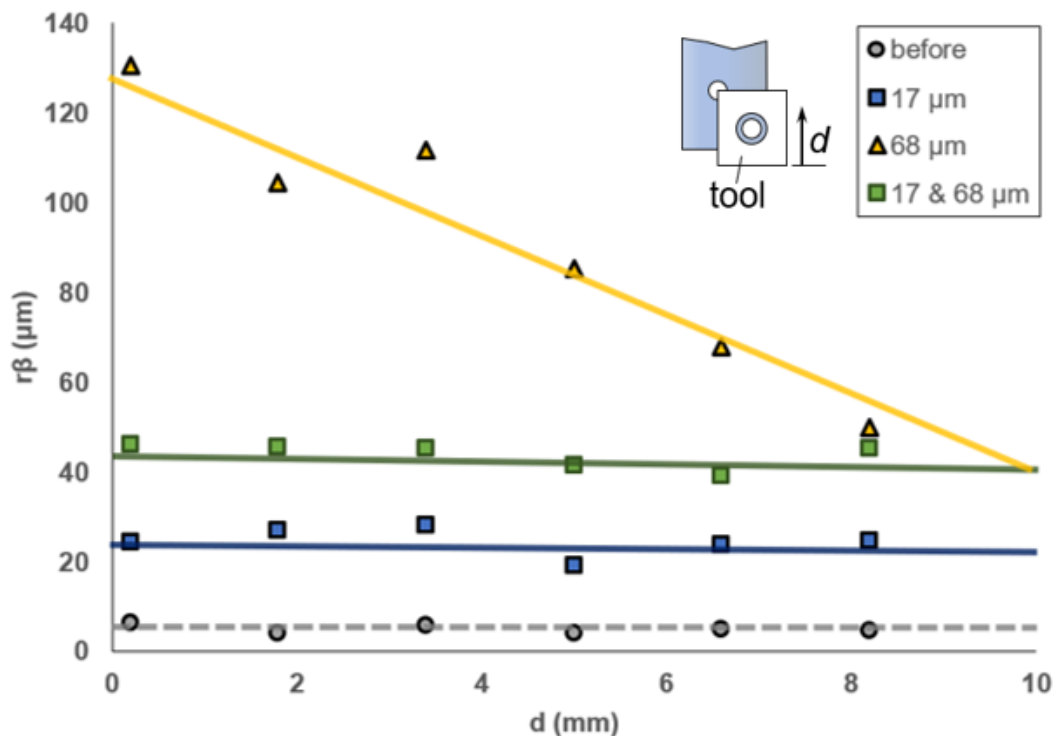
Figure 4.37: rβ vs Tool Height of Using Single and Mixed Sizes of Abrasive.
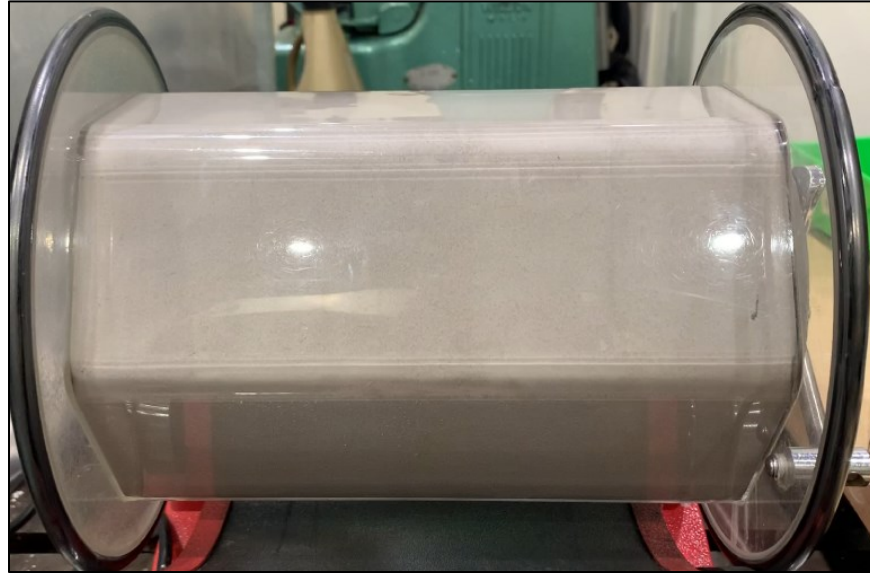
Figure 4.38: 17 and 68 µm Al_2O_3 Being Tumbled with Cornstarch Slurry.

Figure 4.39 summarizes the K values honed by different abrasive sizes. The variability of asymmetry diminished with the larger abrasive size. This is attributed to the ability of the larger abrasives to abrade the defects thus produce a higher edge quality. In addition, the K values converged to 1 with the increased abrasive sizes along with the mixed grit sizes. This suggests that the abrasive size may be used to control the edge asymmetry.
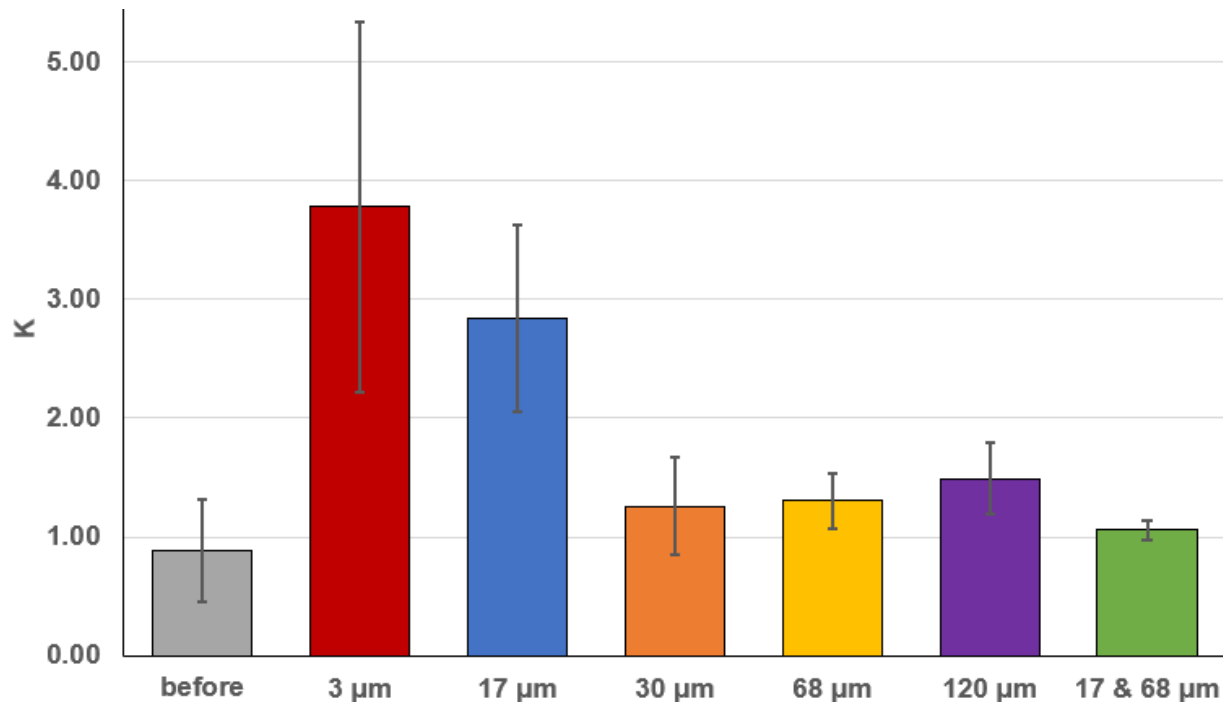
Figure 4.39: Edge Assymetry K Honed by Different Sizes of Abrasive.

Furthermore, the surface roughness along the cutting edge was analyzed. Figure 4.40 summarizes the cutting edge roughness before and after honing by using different sizes of abrasive in the cornstarch slurry. The data shows that the surface roughness increases with the finer size of abrasive. This is due to the inability of finer size abrasive to remove materials as discussed in abrasive percentage experiments; thus, it produced a lower quality of edge. On the other hand, mixing 17 and 68 µm Al_2O_3 dramatically reduced the variability of the surface roughness on the cutting edge comparing to just using 68 µm Al_2O_3 alone. This shows that suspending a larger size of the abrasive in the slurry can enhance the cutting edge honing quality.
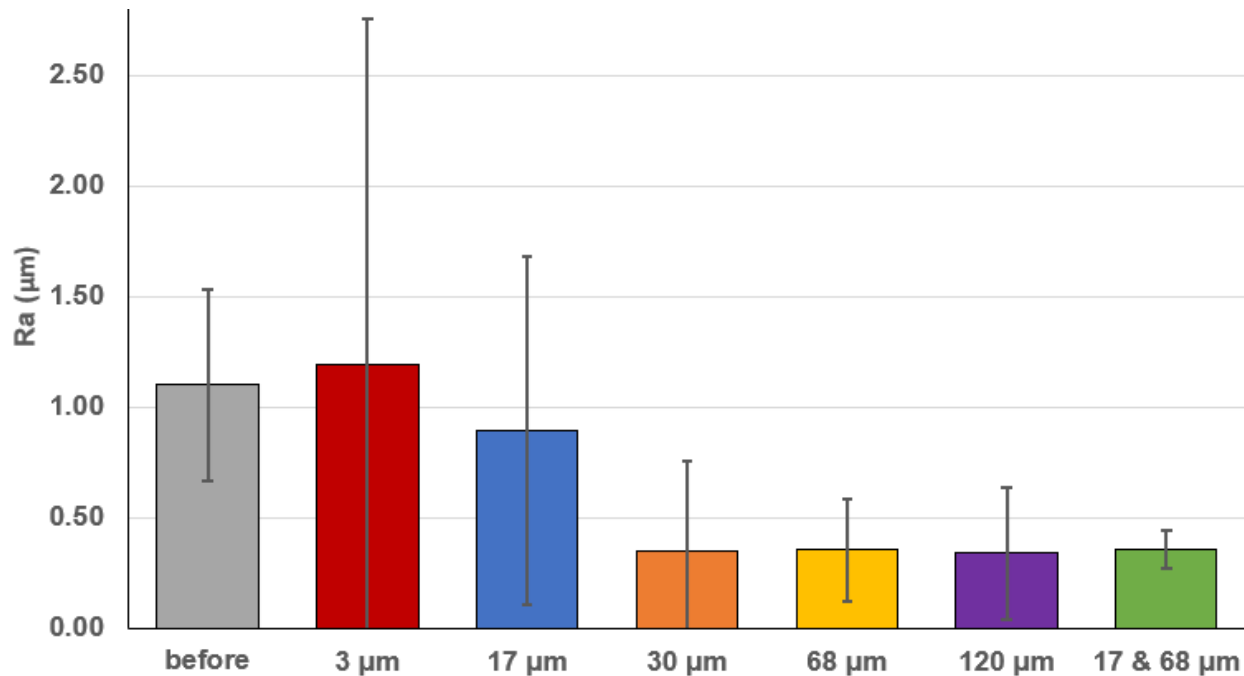
Figure 4.40: Surface Roughness Along the Cutting Edge Honed by Different Sizes of Abrasive.

Since the addition of only 2.5% of 68 μm seems to dramatically increase the edge honing efficiency from the mixed abrasive size experiments, further investigations were conducted to examine the effect of varying the percentage of 68 μm Al_2O_3 on a square carbide insert. The dimensions of the carbide insert are 12.7 mm x 4.7 mm and the experimental parameters are listed in Table 4.9: Noticed the honing time was decreased to 5 minutes to showcase the honing performance on a carbide tool.

CS %	abrasive %		linear speed, direction (m/min)	spindle speed, direction (rpm)	gap (mm)	boundary config	tool holder	time (min)
	17 μm	68 μm						
50	15	variable	10, CCW	3000, CCW	2.0	twin	35°	5

Table 4.9: Parameters for Carbide Experiments.

As shown in Figure 4.41, the increased amount of 68 µm directly correlates with the performance of the edge honing process and the honed r_β along d seems to be fairly uniform. This shows that as long as the larger size of abrasive able to suspend or mix well in the slurry, they can be used as one of the major parameters to control the edge honing performance. In addition to the r_β value, Figure 4.42 shows the insert edges before and after honing at different percentages of 68 µm Al_2O_3. The surface roughness of all edges was reduced from 0.58 µm to 0.16 µm. The amount of 68 µm Al_2O_3 only affects the edge radius but not the surface roughness. However, it is evident that the one honed by 30% 68 µm Al_2O_3 has the highest quality rake and flank faces.
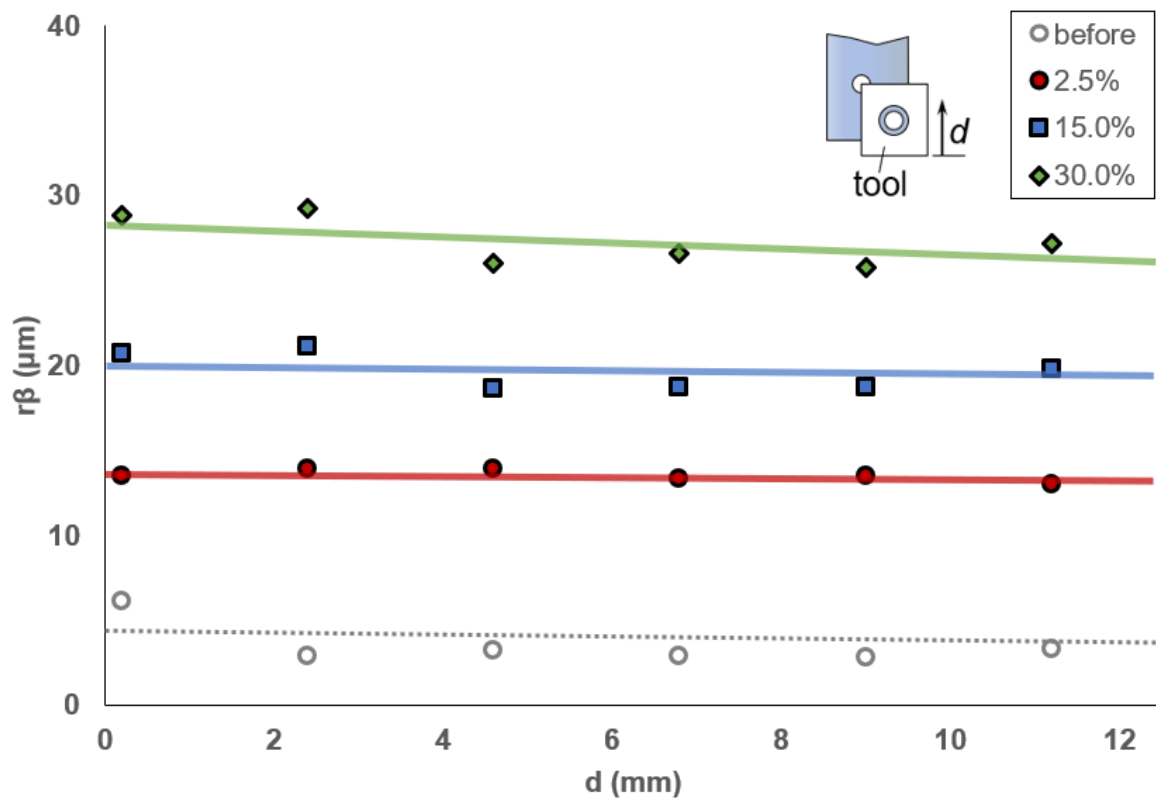
Figure 4.41: Edge Honing Results of Carbide Insert at Different Percentages of 68 µm Al_2O_3.
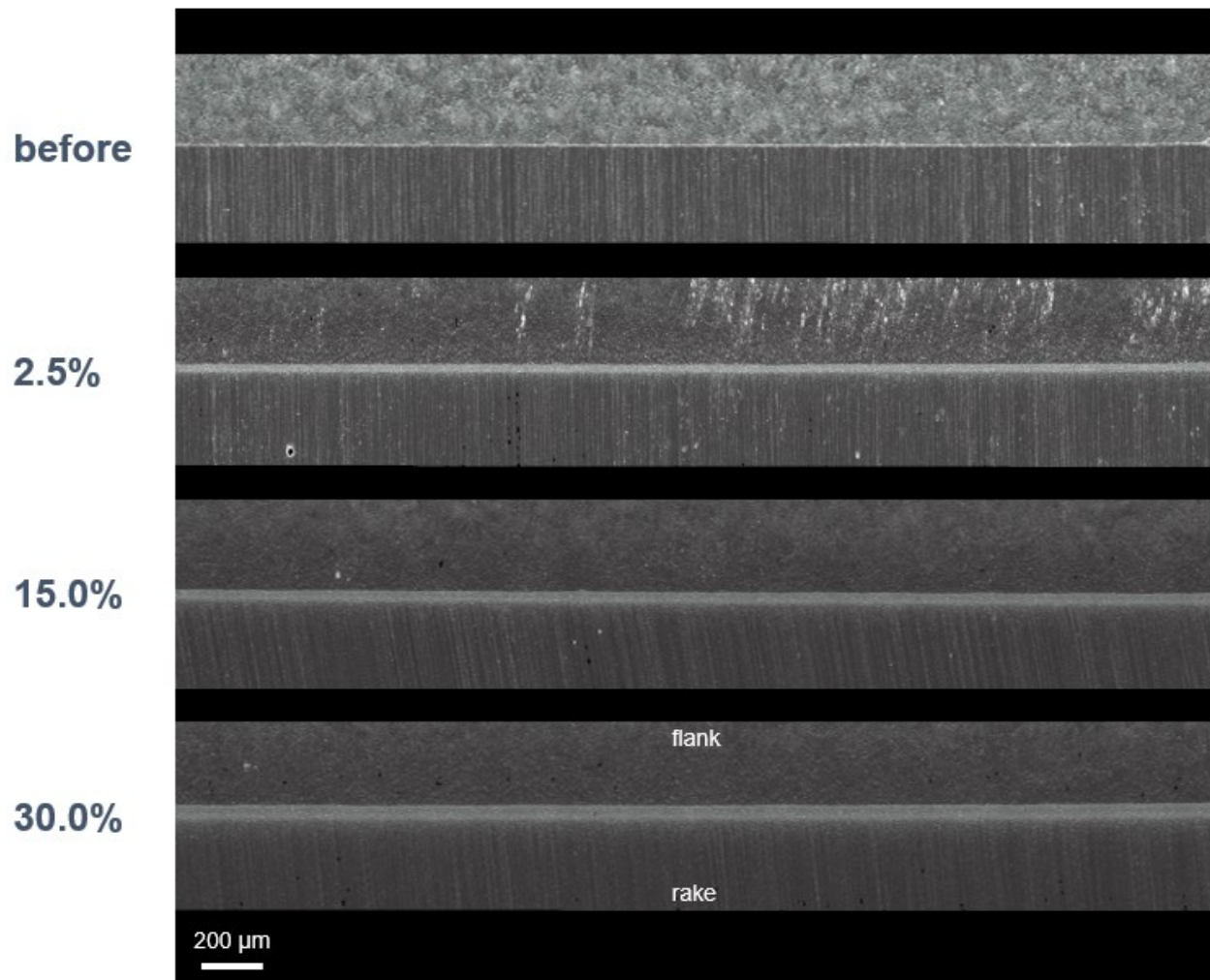
Figure 4.42. Honed Carbide Cutting Edge at Different Pecentages of 68 μm Al_2O_3.

4.8   Honing of Ball-nose Tools

From the HSS inserts honing experiments, it was concluded that r_β, K and gradient edge radius could be controlled by varying the kinematic motions and gap width. In this section, these parameters were tested to prove the feasibility of edge honing carbide ball-nose inserts. The carbide insert is almost 2.5 times as hard as the HSS insert (~ 2150 N/mm^2 vs 900 N/mm^2) [54] [55] and requires a gradient cutting edge radius along the cutting edge for optimal cutting performance. As shown in Figure 4.43 (a & b), the ball-nose tool

has an uncut-chip thickness t_2 greater than t_1 due to the tool geometry. In order for cutting to occur instead of ploughing, every point on the tool should have a r_β value less than t while maintaining a roundness for machining stability. For example, r_β at location 1 should be smaller than t_1 to prevent ploughing; r_β at location 2 should be larger than at 1 but less than t_2. As a result, a ball-nose cutting tool should have edges honed to a gradient r_β as illustrated in Figure 4.43 (c) for an optimal cutting process.
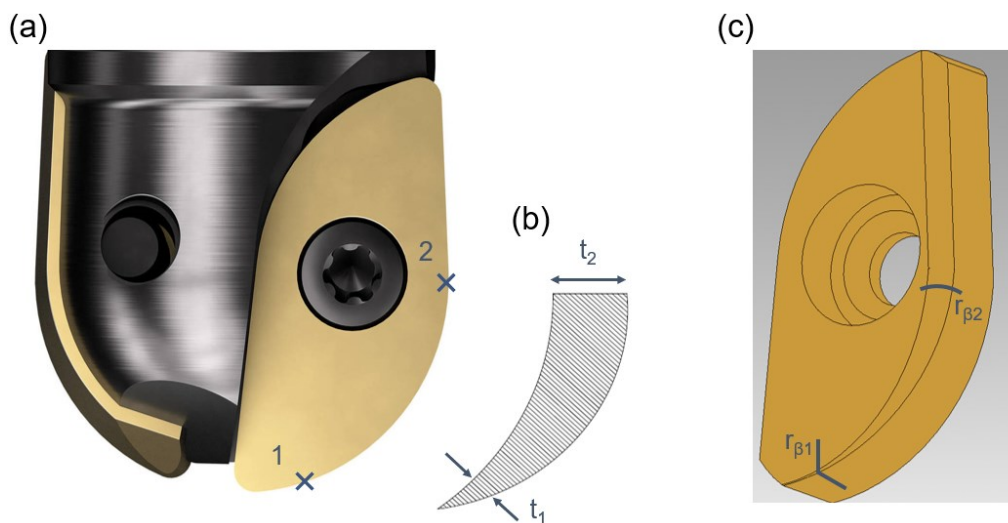
Figure 4.43: (a) Ball-nose Cutting Tool (b) Corresponding Chip Shape (c) Illustration of the Ideal Cutting Edge Radius.

Honed and ground ball-nose cutting inserts along with the tool holder (-10° axial rake, 0° radial rake) were supplied by Sandvik Coromant Company. The ball-nose cutting tool was of a diameter of 12 mm and the r_β values were measured. As shown in Figure 4.44, the honed insert had an average r_β of 40 μm which is relatively large comparing to the optimal r_β needed for machining as reported by [9]. The gradient radius of the honed insert could only be found near the center of the ball-nose insert. This might be the result of the drag finishing in which the edge is subjected to a rather uniform honing. Moreover,

the r_β value near the bottom edge was 30 μm which is relatively large and likely to locally promote ploughing during machining.
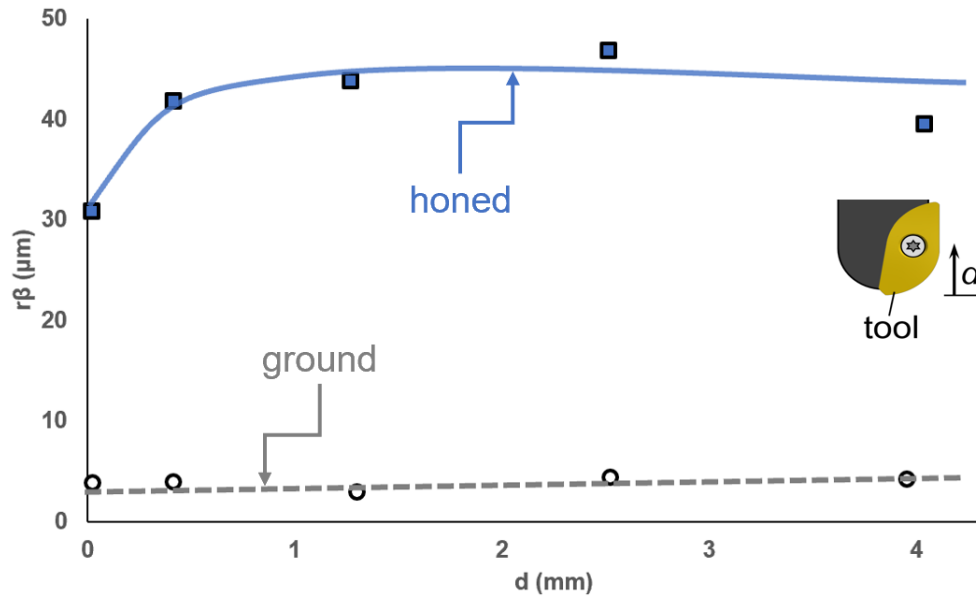
Figure 4.44: r_β for Ground and Honed Ball-nose Inserts as Received from Sandvik Coromant.

Based on the observation on the ball-nose inserts honed commercially, it is deemed necessary to investigate the potential of the novel edge honing process on such insert. Two sets of experiment were performed by varying the spindle speed and gap width. The baseline parameters are as listed in Table 4.10 below.

CS %	abrasive %		linear speed, direction (m/min)	spindle speed, direction (rpm)	gap (mm)	boundary config	time (min)
	17 μm	68 μm					
50	15	20	10, CW	variable, CW	1.3	twin	10

Table 4.10: Baseline Parameters for Ball-nose Experiments.

Figure 4.45 (a) shows the results of the honed ball-nose inserts by varying spindle speeds at 1500 and 3000 rpm. A gradient edge radius was produced along the tool height

d for both experiments. The higher spindle speed showed a greater gradient and performance along the cutting edge. On the other hand, Figure 4.43b shows the results of increasing the gap width from 1.3 to 4 mm. A greater gradient was found with the increased gap width but r_β was similar to the baseline one as moving along the tool height. Thus, given the above observation, the fabrication of the gradient radius is due to the increasing diameter along the curved edge. The corresponding increased local linear speed along the edge for a given rotational speed refer to higher kinetic energy of the abrasives that intensifies their indentation into the insert. As a result, the material removal volume increased alone the curved edge according to Archard's law [56].
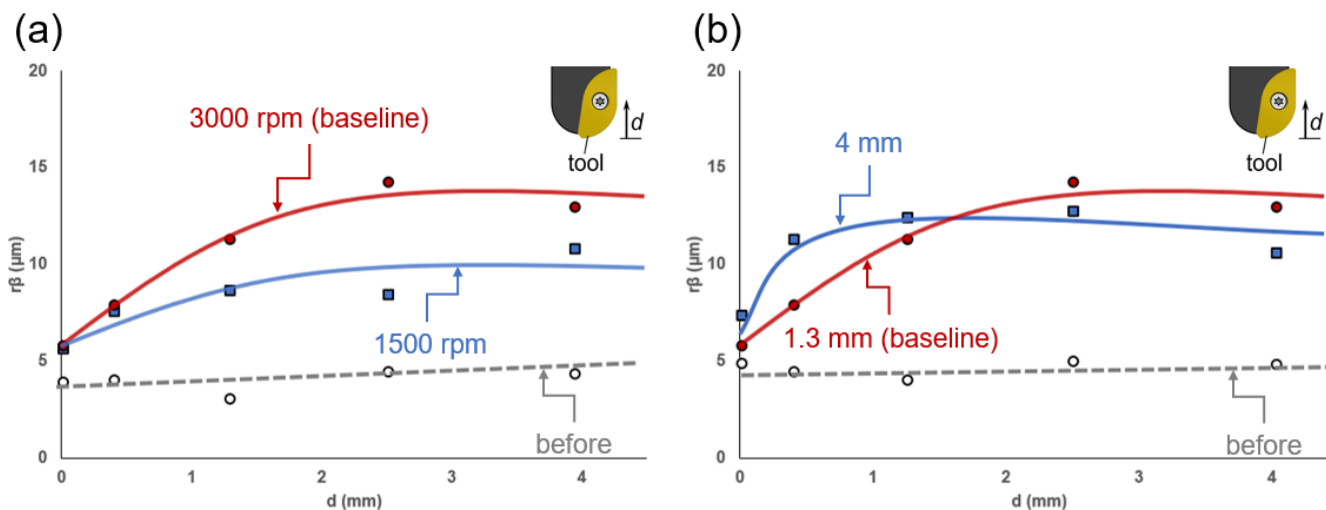
Figure 4.45: Cutting Edge Honing Results for Varying (a) Spindle Speed and (b) Gap Width.

4.9   Application to Commercial Tools

Five carbide cutting tools shown in Figure 4.46 were supplied by a local tooling company. This section explored the capability of the novel process in honing such commercial tools of a complex geometry.

1. Two-flute Drill 2. Three-flute End-mill 3. Three-flute End-mill 4. Tapered End-mill   5. Form Tool
(small)   (large)

Figure 4.46: Cutting Tools Supplied by Apex Tooling Company.

4.9.1   Two-flute Straight Drill

The two-flute drill was of a diameter of 9 mm and was first experimented to examine the edge honing performance as shown in Figure 4.47 (a). The parameters that were used are listed in Table 4.11 below:

CS %	abrasive %		linear speed, direction (m/min)	spindle speed, direction (rpm)	gap (mm)	boundary config	time (min)
	17 μm	68 μm					
50	15	15	10, CW	3000, CW	3.0	twin	5

Table 4.11: Parameters for Edge Honing Two-flute Straight Drill.

Figure 4.47 (b & c) show the cutting edge before and after honing. It is quite clear that the chipped edge was honed to a smooth finish. As shown in Figure 4.48 (a & b), r_β

134

increased from 6 µm to about 13 µm, except the drill point which was honed to about 28 µm. Figure 4.47 (c) also shows that the center point of the drill has been rounded off significantly. This may be attributed to the macro-geometry of the drill causing stagnation of the jammed domain at the center point of the drill which requires further investigation. In addition, the weaker edge honing performance at the bottom is due to the edges being exposed less to the incoming slurry flow.
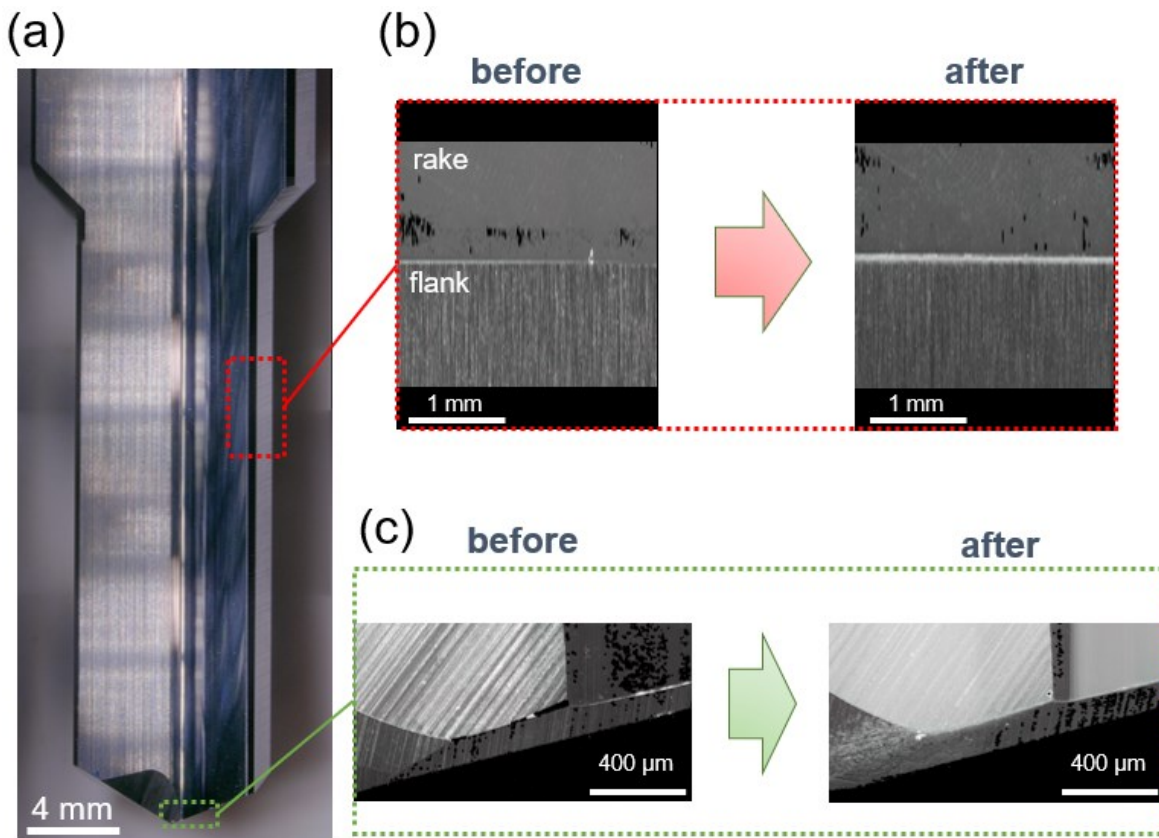
Figure 4.47: (a) Picture of Two-flute drill (b) Before and After Honing of the Peripheral Cutting Edge, (c) Before and After Honing of the Bottom Cutting Edge Near the Drill Point.
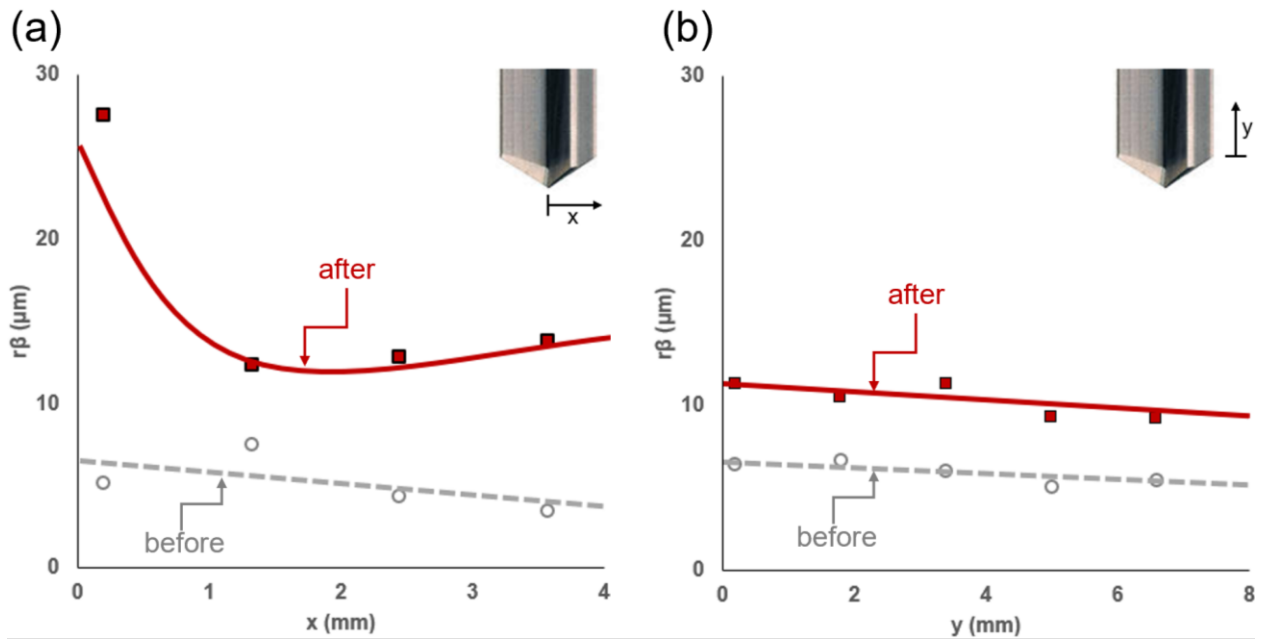
Figure 4.48: Cutting Edge Honing Results for Two-flute Drill on (a) Bottom Edge (b) Peripheral Edge.

4.9.2   Three-flute helical End-Mill (small)

The small three-flute helical end-mill was of a diameter of 11 mm [Figure 4.49 (a)] and was honed with the parameters listed in Table 4.12. The experimental parameters were adjusted to improve the edge honing efficiency compared to the previous test by increasing the cornstarch percentage and 68 µm Al_2O_3 percentage while decreasing the gap width.

CS %	abrasive %		linear speed, direction (m/min)	spindle speed, direction (rpm)	gap (mm)	boundary config	time (min)
	17 µm	68 µm					
51	15	30	10, CW	3000, CW	0.5	twin	5

Table 4.12: Parameters for Edge Honing Small Three-flute Helical End-mill.

As shown in Figure 4.49 (b), the cutting edge of the end-mill had a poor edge quality with multiple chippings. By performing honing with the cornstarch-abrasive media, the flaws on the cutting edge have been removed. As indicated in Figure 4.50, the peripheral r_β was honed from an average of 5 μm to 13 μm and the bottom r_β was honed from an average of 6 μm to 10 μm. The bottom edges refer to lower performance since the peripheral edges encounter more jamming by design. Also, the cutting edge near the center corresponds to a lower performance due to the zero linear local velocity at that point. The bottom edge result was the opposite of the drill due to the center point of the end-mill being somewhat isolated from the incoming slurry flow while the geometry of the drill allows the incoming slurry to reach the center point.
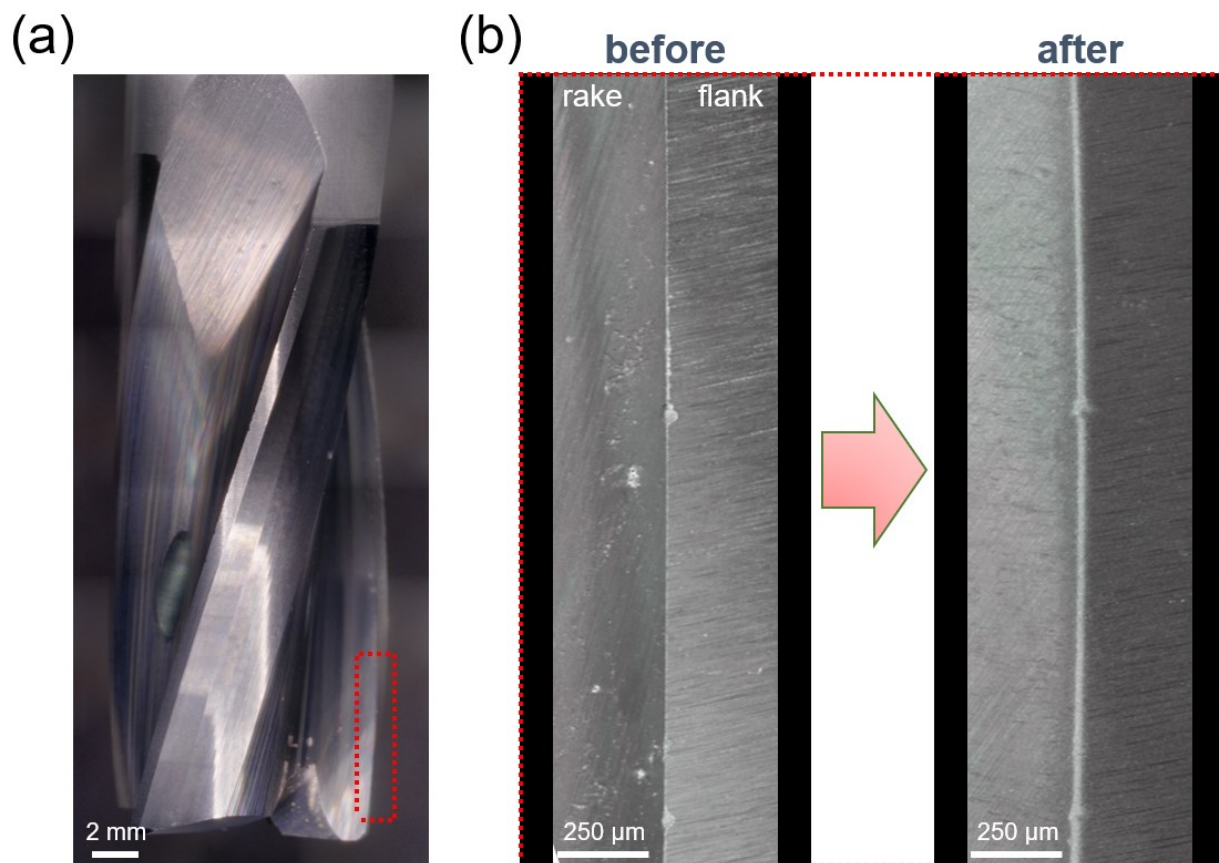
Figure 4.49: (a) Picture of Small Three-flute Helical End-mill (b) Before and After Honing of the Peripheral Cutting Edge.

(a)

(b)
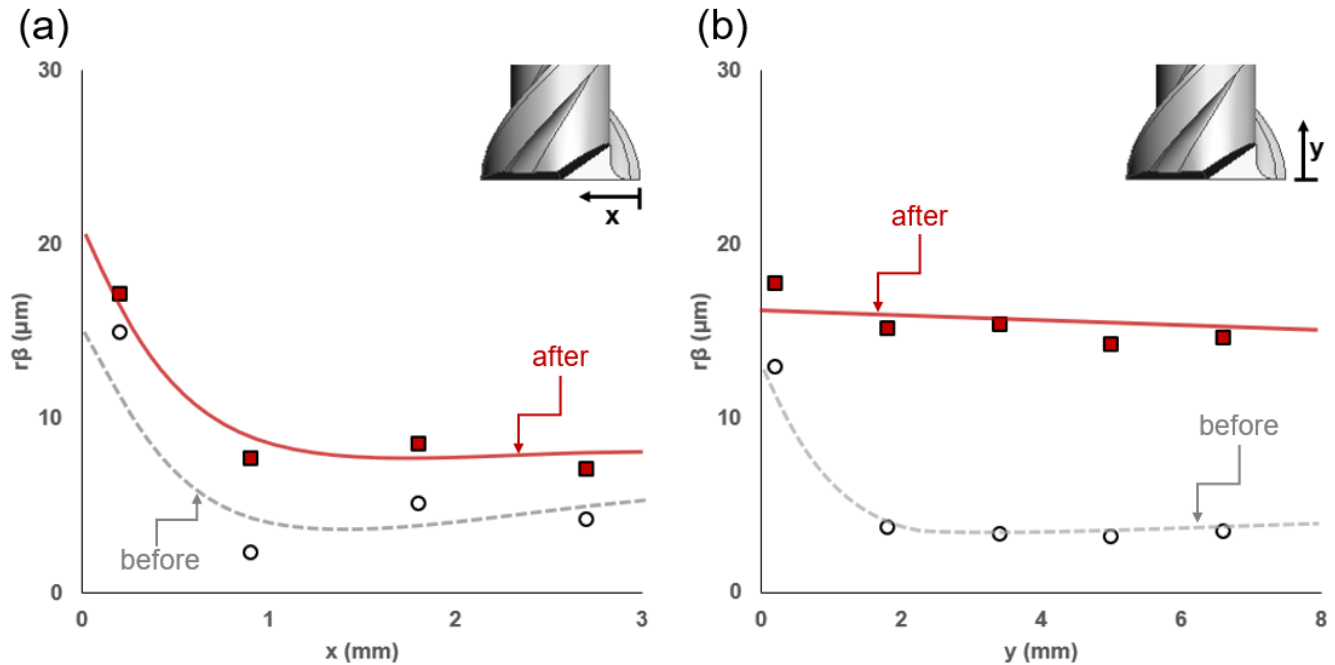
Figure 4.50: Cutting Edge Honing Results of Small Three-flute Helical End-Mill on (a) Bottom Edge (b) Peripheral Edge.

4.9.3   Three-flute Helical End-Mill (Large)

The large three-flute helical end-mill was of a diameter of 25.4 mm and was honed with the parameters listed in Table 4.13. The experimental parameters were similar to the one for the small three-flute helical end-mill but with decreased spindle speed to compensate for the larger tool diameter.

CS %	abrasive %		linear speed, direction (m/min)	spindle speed, direction (rpm)	gap (mm)	boundary config	time (min)
	17 µm	68 µm					
51	15	30	10, CW	2500, CW	0.5	twin	5

Table 4.13: Parameters for Edge Honing Large Three-flute Helical End-mill.

As shown in Figure 4.51, the end-mill was measured with $r_\beta \approx 12$ µm on the peripheral edges as received from the company. The uneven grind marks and chipping along the cutting edge were successfully smoothened out. However, the final average r_β obtained was about 14 µm which is similar to the small helical end mill. This indicates that there is a maximum limit of r_β for the edge honing process with the given input parameters. In order to push the edge honing process forward, more aggressive parameters such as higher cornstarch or Al_2O_3 percentage is needed. Figure 4.51 shows the r_β result of the bottom edge. The bottom edge received less honing performance as discussed previously. In addition, the resultant r_β has a similar trend prior to edge honing. This indicates that the initial cutting edge conditions affect the honing results.

$r_\beta = 12.4$ µm

before   after

$r_\beta = 14.3$ µm
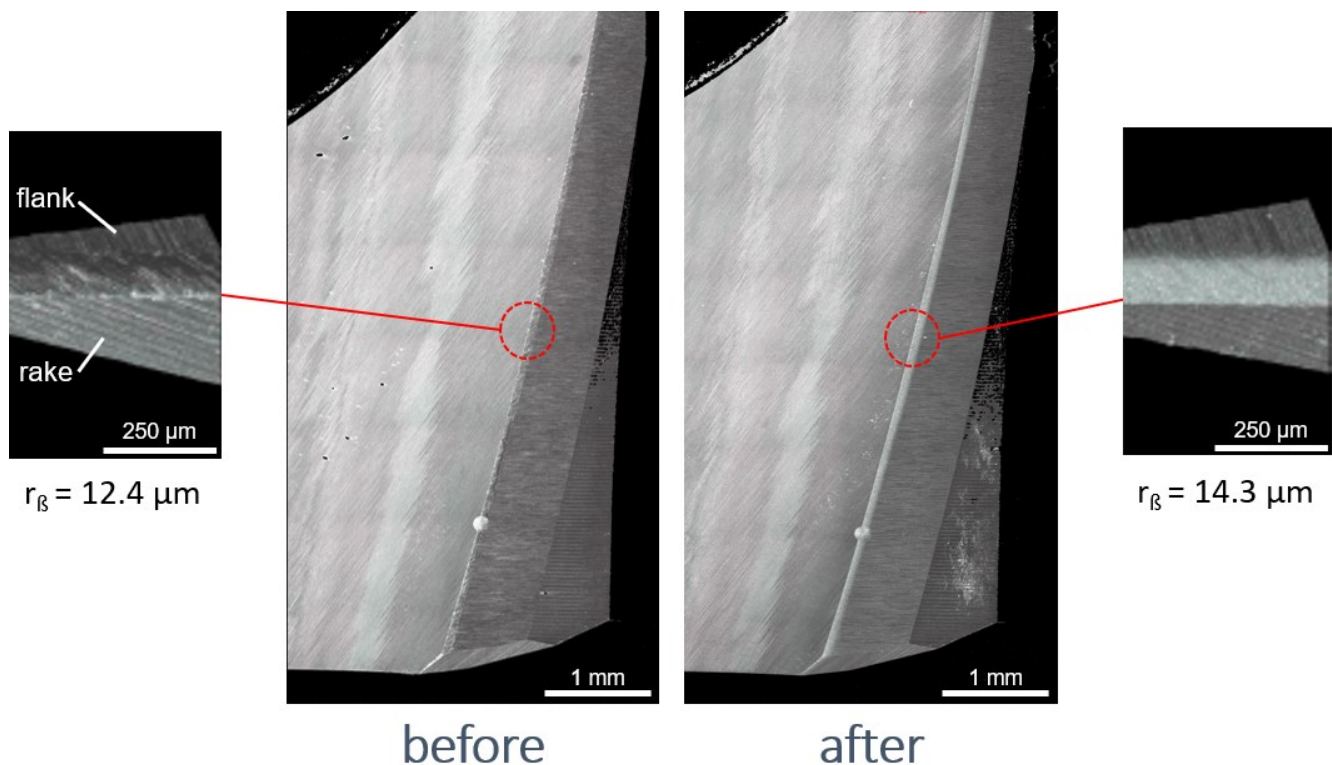
Figure 4.51: Before and After Honing of the Large Three-flute Helical End-mill.

(a)

(b)
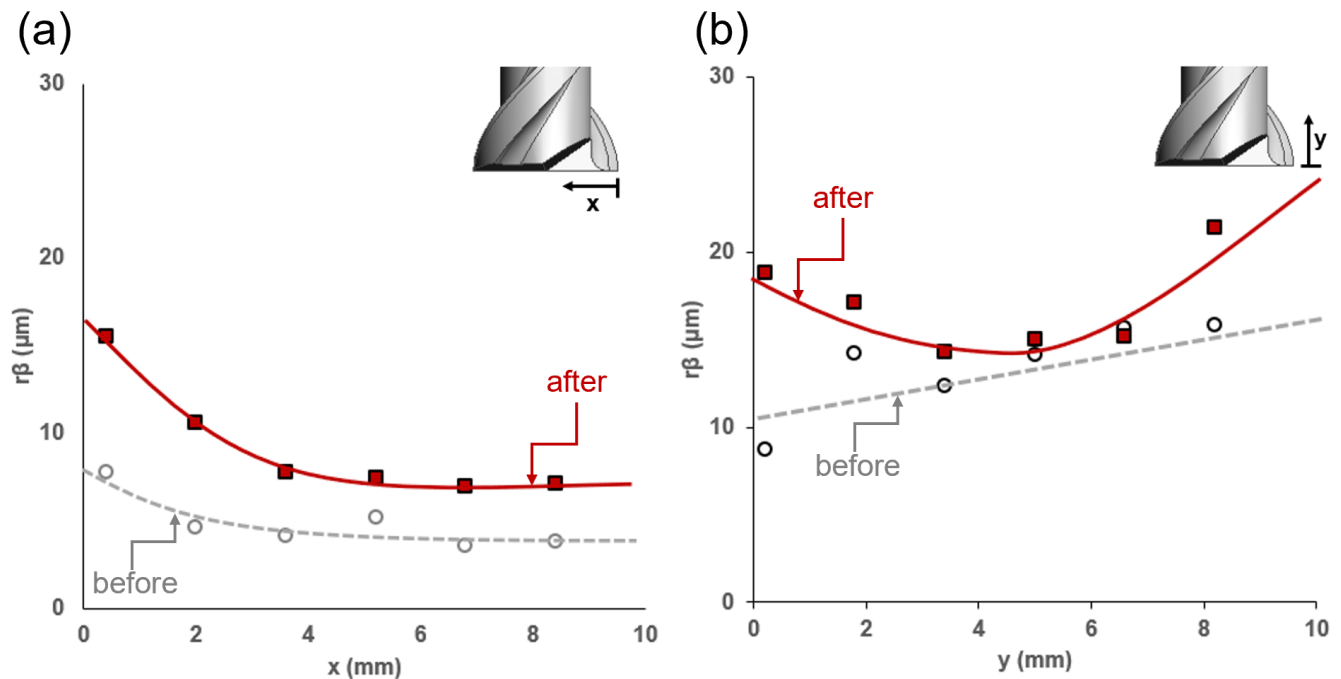
Figure 4.52: Cutting Edge Honing Results of Large Three-flute Helical End-Mill on (a) Bottom Edge (b) Peripheral Edge.

4.9.4   Tapered End-Mill

The tapered end-mill was of minimum and maximum diameters of 4.7 and 8 mm. Since the diameter is relatively small, a special tool adapter was designed to offset the end-mill to mimic orbital milling motions [Figure 4.53]. As a result, the relative velocity between the cutting edges and the slurry would increase. For simplicity of this experiment, the tool was fixed inside the tool adapter and only the edge facing outward radially would be considered in the honing process. The experiment parameters are listed in Table 4.14.

CS %	abrasive %		linear speed, direction (m/min)	spindle speed, direction (rpm)	gap (mm)	boundary config	time (min)
	17 µm	68 µm					
51	15	30	10, CW	2500, CW	0.5	twin	5

Table 4.14. Parameters for Edge Honing Tapered End-Mill.
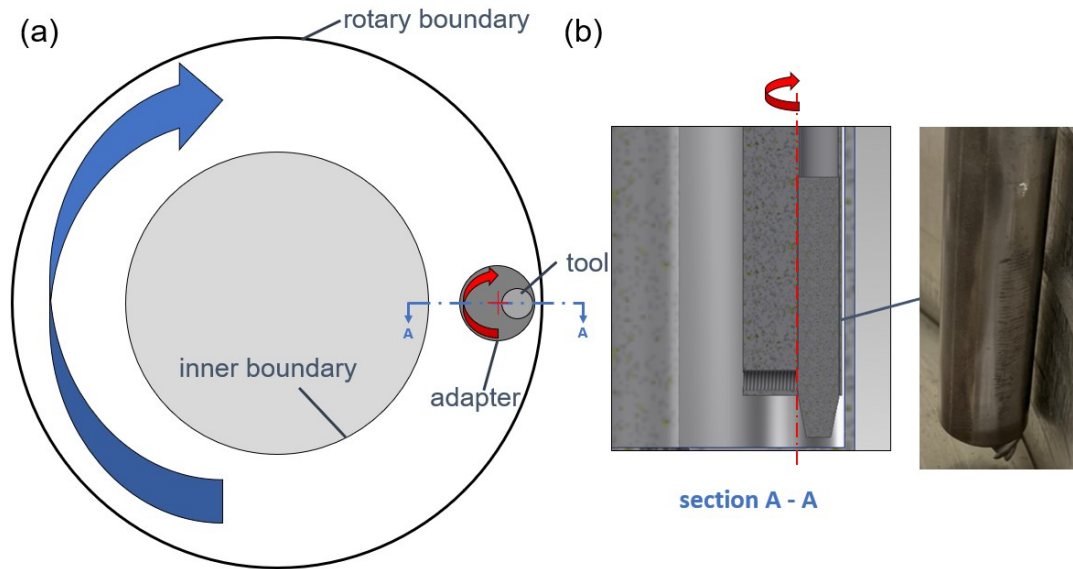
Figure 4.53: (a) Illustration of the Experiment Setup for the Tapered End-mill (b) Section View of the Offset Tapered End-mill.

Figure 4.54 shows the edge quality of the edge before and after honing. The chipping along the edge has been removed and the r_β on the peripheral edge was increased from an average of 9 to 26 μm Figure 4.55. Similar to the previous experiments, the bottom edge received less honing.
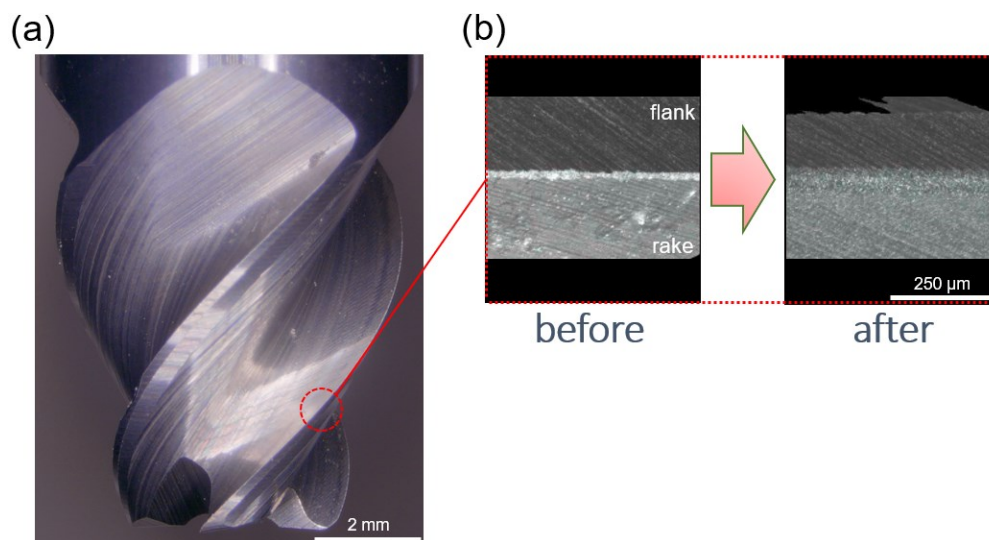
Figure 4.54: Before and After Honing of the Tapered End-mill.
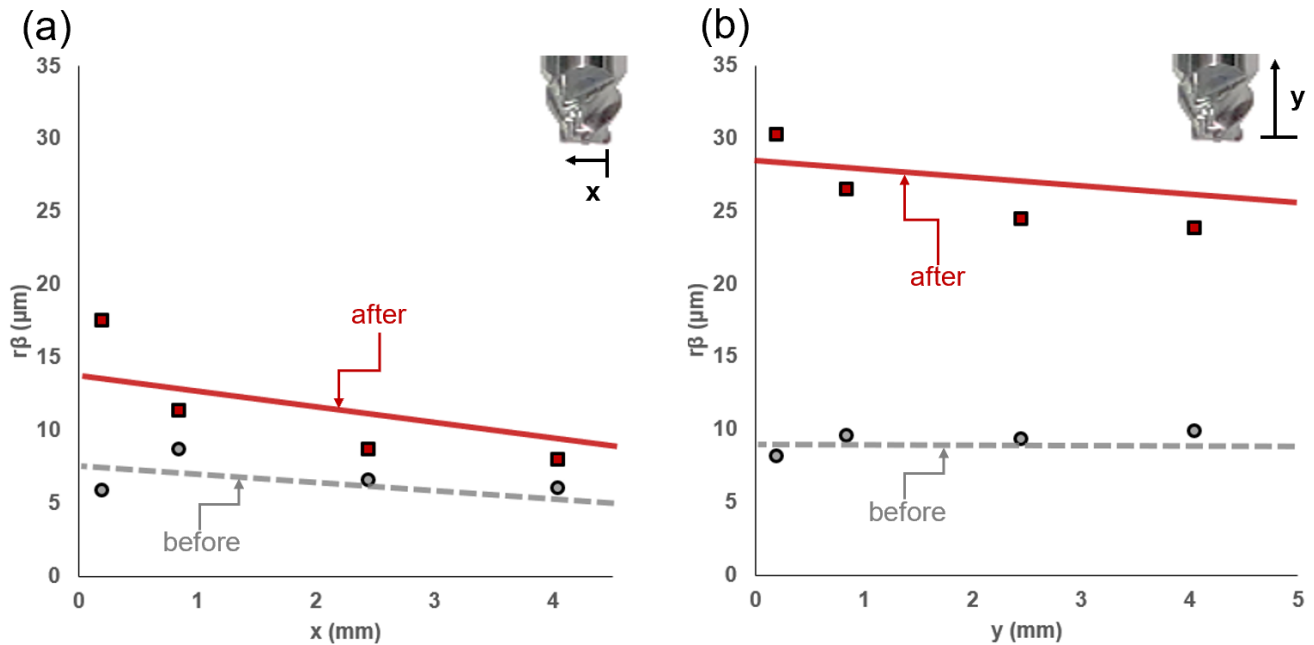
Figure 4.55: Cutting Edge Honing Results of Large Three-flute Helical End-Mill on (a) Bottom Edge (b) Peripheral Edge.

4.9.5 Form Tool

The form milling tool was of complex geometry with varying diameter along the tool height. which presents difficulty to current edge honing techniques to accommodate its shape and required microgeometry. The novel cutting edge honing media can conform to the shape of the form milling tool effortlessly which then turns into a jammed solid to uphold abrasion during process. In addition, the fluctuating diameter will result in variation of linear velocity along the curved edge which causes the abrasives to hone the edge at different rates depending on the resultant kinetic energy and sliding distance. Parameters for edge honing the form tool are listed in Table 4.15.

CS %	abrasive %		linear speed, direction (m/min)	spindle speed, direction (rpm)	gap (mm)	boundary config	time (min)
	17 µm	68 µm					
52	15	30	10, CW	3000, CW	0.5	twin	5

Table 4.15: Parameters for Edge Honing the Form Tool.

As shown in Figure 4.56, three points on the cutting edges along each fir tree feature were measured before and after honing. It is shown that the r_β has increased from an average of 9 µm to 17 µm. Variation along the edge profile could be found due to variations in linear speed. However, such variation of r_β is beneficial to accommodate the variation in un-cut chip thickness as discussed in the ball-nose experiments.
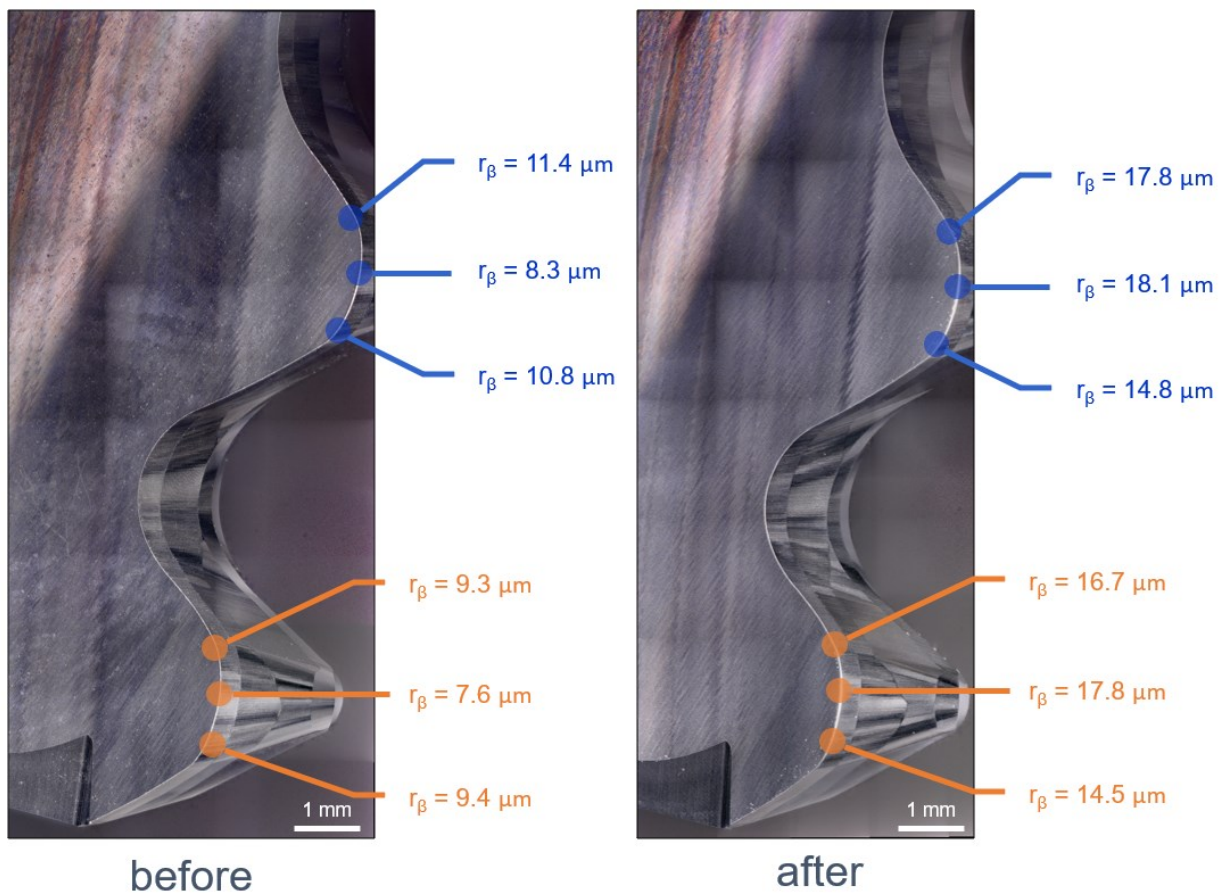
Figure 4.56: Before and After Honing of the Form Tool.

Chapter 5

Conclusions and Future Work

5.1   Conclusions

This research was motivated by the need for a cost-effective edge honing process. Non-Newtonian media, namely the cornstarch-abrasive slurry, showed a promising edge honing performance while adapting to different tool shapes as well as producing different cutting edge micro-geometries through its dynamic response to deformation. A number of investigations on edge honing were performed, the major findings are summarized below.

1.   The experimental apparatus was manufactured which primarily consists of a rotary boundary and a tool spindle to test the required kinematic motions of the novel edge honing process. It was determined that both orbital and spindle

motions are required to create a jammed domain in the presence of a rigid boundary.

2. Cutting edge honing and sharpening were manifest at the leading and trailing edges respectively. An explanation of slurry flow was offered by examining the surface roughness of insert faces. The findings were re-confirmed by edge honing and sharpening twist drills.

3. Edge honing performance cannot be assessed solely using r_β as the measurement can be skewed by asymmetric edges. Instead, the edge length to virtual tool was used as an indicator of the edge honing performance for asymmetric edges.

4. Cutting edge asymmetry K was controlled by adjusting the angle of attack θ which is similar to the setting angle in micro-blasting and 5-axis brush honing technique. It was found that when θ ≈ 35°, a symmetrical cutting edge could be produced with the baseline process parameters.

5. The presence of the inner boundary does not affect the honing performance as the dynamically jammed domain localized near the outer boundary. However, the inner boundary can reduce the volume of slurry required which can help reduce cost.

6. There is a fine line on how much cornstarch should be added to the slurry for the edge honing process. When the percentage is low, the honed edge appears to have a poor quality as there were not enough cornstarch particles in the fluid to sustain a force bearing network within the jammed domain that could uphold abrasion. An increase in cornstarch percentage reduced variability and produced

a much higher r_β. However, when the cornstarch percentage is higher than 51%, the workability of the slurry was affected.

7. It was shown that the spindle speed correlates with edge radius of the cutting edge. However, a high spindle speed would lead to the formation of a vortex around the tool body which plateaued the edge honing performance. An increment in cornstarch percentage from 50% to 51% helped to reduce the formation of the vortex which then improved the edge honing performance.

8. It was quite interesting to see that the lower orbital speed of the rotary boundary would lead to a production of gradient cutting edge radius. This is due to the abrasives having more time to sediment when they were orbiting away from the spindle. Such stratification of abrasives was verified by placing a mixer diametrically opposed to the honing spindle which reduced the gradient on the cutting edge radius.

9. Experiments were carried out to examine the influence of abrasive percentage and size on the novel edge honing process. The percentage of abrasives presented in the slurry positively correlated to the edge honing performance. On the other hand, larger (68 μm) abrasives tend to sediment to the bottom and produces a larger radius near the bottom of the tool edge while the smaller (17 μm + 30 μm) abrasives could generate an uniform cutting edge, but with limited honing ability. A combination of abrasive sizes (17 μm + 68 μm) was able to productively produce an uniform cutting edge.

10. The ball-nose carbide inserts were honed to a gradient radius due to the change in linear speed along the curved edge for a given rotational speed.

11. Industrial tools with various tool shapes were provided by a local company. The tools were honed using the knowledge gained from previous experiments. Additional techniques were used to compensate for some restrictions due to the tool design. For example, a small radius tool was offset from the center of the tool to increase the local velocity at the tool edge for more abrasion.

The above findings provided the proof of concept for edge honing various cutting tools using the dynamic shear jamming suspension. The method is cost-effective and environmentally friendly. Additional works may be accomplished in the future to further develop the novel finishing process.

5.2   Future Work

Although the major goals of developing the edge honing process tools were accomplished, some areas are suggested for further investigation to improve the novel edge honing process.

1. Since the edge honing technique requires a rotational velocity, the peripheral edges receive greater honing performance at the bottom edges. Two changes might aid the performance at the bottom edges. For example, since gap width dictates the intensity of the squeeze flow of the jammed domain, an extrusion at the bottom of the rotary boundary might help to compensate for the low performance at the center of the tool due to the decrease in the linear speed (Figure 5.1).
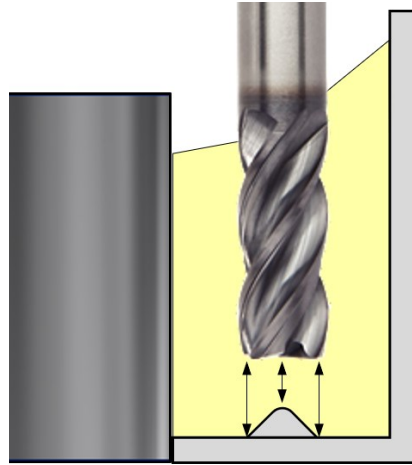
Figure 5.1: An Extrusion on the Bottom of the Rotary Boundary.

In addition, the spindle can be tilted as shown in Figure 5.2. This way, the bottom edge can be exposed to the incoming slurry which may result in a higher edge honing performance at the bottom edges.
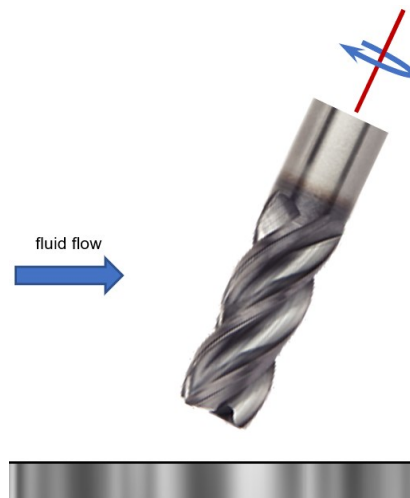
Figure 5.2: Tilting of the Tool Spindle.

2. As shown in Figure 5.3, the effect of the axial rake angle needs to be investigated further as it can affect the cutting edge asymmetry on the bottom edges.
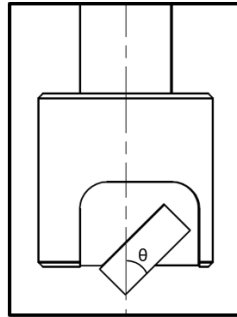
Figure 5.3: Axial Rake Angle.

3. The cutting edge asymmetry of the solid tool cannot be easily controlled as the radial rake angle is fixed. A possible solution is to adjust the slurry compositions as the cornstarch percentage affects the K value. Reduced performance due to low cornstarch percentage may be compensated by increasing the Al_2O_3 percentage.

4. Al_2O_3 abrasive was used to edge hone the cutting tools throughout this work. Different types of abrasive such as crystalline diamond and silicon carbide may be used to examine the effect on the edge honing performance and the surface roughness of the edges.

5. Edge honing can be achieved in a mass scale by placing multiple tools in the bath as shown in Figure 5.4. However, the minimum circumferential distance between each spindle has to be investigated since the slurry flow may be interrupted by each other.
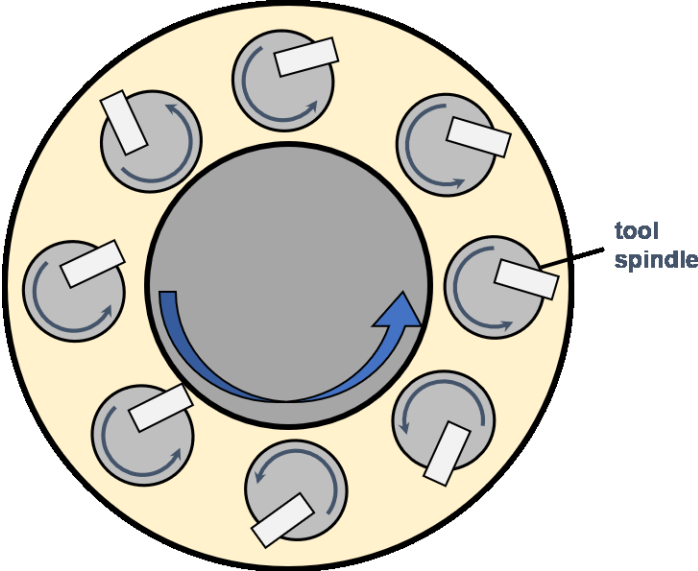
Figure 5.4: Edge Honing Multiple Cutting Tools.

Reference

[1]   A. S. David and S. A. John, *Metal Cutting Theory*, Third., vol. 66. CRC Press, 2012.

[2]   I. A. Time, *Resistance of Metals and Wood to Cutting (in Russian)*. St. Petersburg, Russia, 1870.

[3]   H. Treska, "Mmories Sur le Rabotage des Mtaux, Bulletin de la Scite dE-couragement pour," *IIndustrie Natl.*, vol. 15, pp. 585–685, 1873.

[4]   A. Mallock, "The action of cutting tools," *Proc. R. Soc. L.*, vol. 33, pp. 127–139, 1881.

[5]   M. E. Merchant, "Mechanics of the metal cutting process. I. Orthogonal cutting and a type 2 chip," *J. Appl. Phys.*, vol. 16, no. 5, pp. 267–275, 1945.

[6]   P. Albrecht, "New developments in the theory of the metal-cutting process: Part I. the ploughing process in metal cutting," *J. Manuf. Sci. Eng. Trans. ASME*, vol. 82, no. 4, pp. 348–356, 1960.

[7]   Chien K, "Influence of Tool Sharpness on the Mechanics of Metal Cutting," Massachusetts Instiute of Techn., Cambridge, 1953.

[8]   M. Masuko, "Fundamental Research on Metal Cutting Process. II. Plasticity," 1953.

[9]   B. Denkena and D. Biermann, "Cutting edge geometries," *CIRP Ann. - Manuf. Technol.*, vol. 63, no. 2, pp. 631–653, 2014.

[10]   TBM Precision Engineering Ltd, "Indexable Insert Tooling." [Online]. Available: http://www.tbmprecision.com/products/indexable-insert-tooling/.

[11]   I. Distribution, "Solid Round Tool." [Online]. Available: https://abm-website-assets.s3.amazonaws.com/inddist.com/s3fs-public/styles/hero/public/featured_image/2017/11/Cutting.gif?itok=lx3YeHva.

[12]   S. R. Waitukaitis and H. M. Jaeger, "Impact-activated solidification of dense suspensions via dynamic jamming fronts," *Nature*, vol. 487, no. 7406, pp. 205–209, 2012.

[13]   Nao, "Walking on Ooblecks – add it to your bucket list," 2015. [Online]. Available: http://sciencewows.ie/blog/walking-on-ooblecks-add-it-to-your-bucket-list/.

[14]   Extrude Hone, "ABRASIVE FLOW MACHINING (AFM)." [Online]. Available:

https://extrudehone.com/products/abrasive-flow-machining-afm.

[15] Moratex Institute of Security Technology, "Liquid body armour proves to be bullet proof." [Online]. Available: https://www.youtube.com/watch?v=L5Ts9lYZIDk.

[16] C. Rodríguez, *Cutting edge preparation of precision cutting tools by applying micro-abrasive jet machining and brushing*. 2009.

[17] R. W. Overholser, R. J. Stango, and R. A. Fournelle, "Morphology of metal surface generated by nylon/abrasive filament brush," *Int. J. Mach. Tools Manuf.*, vol. 43, no. 2, pp. 193–202, 2003.

[18] B. Denkena, J. Köhler, B. Breidenstein, A. M. Abrão, and C. E. H. Ventura, "Influence of the cutting edge preparation method on characteristics and performance of PVD coated carbide inserts in hard turning," *Surf. Coatings Technol.*, vol. 254, pp. 447–454, 2014.

[19] E. Bassett, J. Köhler, and B. Denkena, "On the honed cutting edge and its side effects during orthogonal turning operations of AISI1045 with coated WC-Co inserts," *CIRP J. Manuf. Sci. Technol.*, vol. 5, no. 2, pp. 108–126, 2012.

[20] E. Krebs, M. Wolf, D. Biermann, W. Tillmann, and D. Stangier, "High-quality cutting edge preparation of micromilling tools using wet abrasive jet machining process," *Prod. Eng.*, vol. 12, no. 1, pp. 45–51, 2018.

[21] K. D. Bouzakis *et al.*, "The effect of micro-blasting procedures on the cutting performance of coated tools," *FME Trans.*, vol. 37, no. 2, pp. 71–82, 2009.

[22] E. Uhlmann, A. Eulitz, and A. Dethlefs, "Discrete element modelling of drag finishing," *Procedia CIRP*, vol. 31, pp. 369–374, 2015.

[23] OTEC Präzisionsfinish GmbH, "OTEC Präzisionsfinish GmbH_ Drag finishing machines." [Online]. Available: https://www.otec.de/en/products/mass-finishing/drag-finishing-machines/.

[24] J. C. Aurich, M. Zimmermann, and L. Leitz, "The preparation of cutting edges using a marking laser," *Prod. Eng.*, vol. 5, no. 1, pp. 17–24, 2011.

[25] N. Z. Yussefian and P. Koshy, "Application of foil electrodes for electro-erosion edge honing of complex-shaped carbide inserts," *J. Mater. Process. Technol.*, vol. 213, no. 3, pp. 434–443, 2013.

[26] J. C. Aurich, C. Effgen, and B. Kirsch, "Cutting edge preparation with elastic bonded superabrasive grinding wheels," *CIRP Ann. - Manuf. Technol.*, vol. 65, no. 1, pp. 329–332, 2016.

[27] Y. Fu, H. Gao, Q. Yan, and X. Wang, "A new predictive method of the finished surface profile in abrasive flow machining process," *Precis. Eng.*, vol. 60, no. April, pp. 497–505, 2019.

[28] J. Rech, Y. C. Yen, M. J. Schaff, H. Hamdi, T. Altan, and K. D. Bouzakis, "Influence of cutting edge radius on the wear resistance of PM-HSS milling

inserts," *Wear*, vol. 259, no. 7–12, pp. 1168–1176, 2005.

[29] B. Karpuschewski, O. Byelyayev, and V. S. Maiboroda, "Magneto-abrasive machining for the mechanical preparation of high-speed steel twist drills," *CIRP Ann. - Manuf. Technol.*, vol. 58, no. 1, pp. 295–298, 2009.

[30] I. G. Schmid *et al.*, "United States Patent (45) Date of Patent :," vol. 2, no. 12, pp. 5–12, 2006.

[31] N. C. Crawford, L. B. Popp, K. E. Johns, L. M. Caire, B. N. Peterson, and M. W. Liberatore, "Shear thickening of corn starch suspensions: Does concentration matter?," *J. Colloid Interface Sci.*, vol. 396, pp. 83–89, 2013.

[32] S. Gürgen and M. A. Sofuoğlu, "Experimental investigation on vibration characteristics of shear thickening fluid filled CFRP tubes," *Compos. Struct.*, vol. 226, no. May, 2019.

[33] J. Orwig, "This substance lets you 'walk on water' — here's how it works - Business Insider," 2018. [Online]. Available: https://www.businessinsider.com/non-newtonian-fluid-filled-pool-substance-walk-on-water-how-it-works-2017-12. [Accessed: 08-Oct-2019].

[34] P. J. PRITCHARD, *Introduction to Fluid Mechanics 8th Edition*. .

[35] F. A. M. When, S. Putty, and U. Rheology, "What is rheology anyway ? Page 1 of 4 What is rheology anyway ? What is rheology anyway ?," *J. Rheol. (N. Y. N. Y).*, pp. 12–15.

[36] Anton Paar, "Modular Compact Rheometer." [Online]. Available: https://www.anton-paar.com/?eID=documentsDownload&document=57983&L=0.

[37] N. J. Wagner and J. F. Brady, "The popular interest in cornstarch and water mixtures," no. October, pp. 27–32, 2009.

[38] B. H. Lyu, Q. K. He, S. H. Chen, Q. Shao, Y. Chen, and Z. Y. Geng, "Experimental study on shear thickening polishing of cemented carbide insert with complex shape," *Int. J. Adv. Manuf. Technol.*, vol. 103, no. 1–4, pp. 585–595, 2019.

[39] B. Liu, M. Shelley, and J. Zhang, "Focused force transmission through an aqueous suspension of granules," *Phys. Rev. Lett.*, vol. 105, no. 18, pp. 1–4, 2010.

[40] S. Von Kann, J. H. Snoeijer, and D. Van Der Meer, "Velocity oscillations and stop-go cycles: The trajectory of an object settling in a cornstarch suspension," *Phys. Rev. E - Stat. Nonlinear, Soft Matter Phys.*, vol. 87, no. 4, pp. 1–14, 2013.

[41] S. R. Waitukaitis, *Impact-Activated Solidification of Cornstarch and Water Suspensions*. 2015.

[42] E. Han, I. R. Peters, and H. M. Jaeger, "High-speed ultrasound imaging in dense suspensions reveals impact-activated solidification due to dynamic shear

jamming," *Nat. Commun.*, vol. 7, pp. 1–8, 2016.

[43]   D. Bi, J. Zhang, B. Chakraborty, and R. P. Behringer, "Jamming by shear," *Nature*, vol. 480, no. 7377, pp. 355–358, 2011.

[44]   E. Han, L. Zhao, N. Van Ha, S. T. Hsieh, D. B. Szyld, and H. M. Jaeger, "Dynamic jamming of dense suspensions under tilted impact," *Phys. Rev. Fluids*, vol. 4, no. 6, pp. 1–8, 2019.

[45]   S. Majumdar, I. R. Peters, E. Han, and H. M. Jaeger, "Dynamic shear jamming in dense granular suspensions under extension," *Phys. Rev. E*, vol. 95, no. 1, pp. 1–10, 2017.

[46]   J. Span, P. Koshy, F. Klocke, S. Müller, and R. Coelho, "Dynamic jamming in dense suspensions: Surface finishing and edge honing applications," *CIRP Ann. - Manuf. Technol.*, vol. 66, no. 1, pp. 321–324, 2017.

[47]   Bruker Alicona, "Infinite Focus_ Dimensional metrology & surface roughness _ Alicona." [Online]. Available: https://www.alicona.com/products/infinitefocus/.

[48]   I. R. Peters and H. M. Jaeger, "Quasi-2D dynamic jamming in cornstarch suspensions: Visualization and force measurements," *Soft Matter*, vol. 10, no. 34, pp. 6564–6570, 2014.

[49]   J. H. Span, "Free Abrasive Finishing with Dynamic Shear Jamming Fluid FREE ABRASIVE FINISHING WITH DYNAMIC," McMaster University, 2016.

[50]   F. Preston, "The Theory and Design of Plate Glass Polishing Machines," *J. Glas. Technol.*, vol. 11, p. 214, 1927.

[51]   S. Gürgen, W. Li, and M. C. Kuşhan, "The rheology of shear thickening fluids with various ceramic particle additives," *Mater. Des.*, vol. 104, pp. 312–319, 2016.

[52]   S. V. Franklin and M. D. Shattuck, *Handbook of Granular Materials*, vol. 53, no. 9. 2019.

[53]   M. J. Metzger, B. Remy, and B. J. Glasser, "All the Brazil nuts are not on top: Vibration induced granular size segregation of binary, ternary and multi-sized mixtures," *Powder Technol.*, vol. 205, no. 1–3, pp. 42–51, 2011.

[54]   L. Nippon Tungsten Co., "Is cemented carbide hard?," 2012. [Online]. Available: https://www.nittan.co.jp/en/products/carbide_007_023.html. [Accessed: 23-Dec-2019].

[55]   I. C. Tools, "HIGH SPEED STEEL TOOL DATA." [Online]. Available: https://www.icscuttingtools.com/Tooldata.htm. [Accessed: 23-Dec-2019].

[56]   V. Popov, "Generalized archard law of wear based on rabinowicz criterion of wear particle formation," *Facta Univ. Ser. Mech. Eng.*, vol. 17, no. 1, pp. 39–45, 2019.